Computational Studies of Ziegler-Natta Catalysis

and

Concurrent Resonance Computations

Thesis by

Erik Paul Bierwagen

In Partial Fulfillment of the Requirements

for the Degree of

Doctor of Philosophy

California Institute of Technology
Pasadena, California

1995
(Submitted May 26, 1995)

To Laura, for everything

Acknowledgments

There are so many people who have affected me during my stay at Caltech that it is impossible to acknowledge every one of them.

I wish to first, and most importantly, thank my advisor Bill Goddard for guiding me during the ups and downs of research. It is not always easy to keep up with someone with so many different interests in chemistry, but it sure does make the work exciting. I also want to thank him for teaching me what it means to be a good theoretician.

I also wish to thank John Bercaw for teaching me much about Ziegler-Natta catalysis, and for allowing me a brief tenure in his group. I tried hard to be a synthetic chemist, John, but I guess at heart I am a theoretician!

Many thanks go out to the members of the Goddard and Bercaw groups for their support, knowledge and camaraderie during my stay. In particular, Jason Perry, Rick Muller, Jamil Tahir-Kheli, and Kevin Plaxco (the 007 gang), Terry Coley, Jean-Marc Langlois, Alan Mathiowetz, K-T Lim, Charles Musgrave, Jim Gerdy, and Ken Brameld from the Goddard Group have been ideal colleagues: generous, helpful, and lots of fun! I am also indebted to Terry Coley for all of his patience while we worked together on the resonance program. Bryan Coughlin, Donnie Cotter, Sharad Hajela, Tim Herzog, and Andy Keily from the Bercaw group helped keep me grounded in experimental results, in addition to teaching me much about organometallic chemistry. And I cannot forget the great assistance of Siddharth Dasgupta, especially as I was learning to use force fields (as he claims, they will, like love, conquer all).

Debbie Chester and Darryl Willick have provided much assistance guiding me through the inner workings of Caltech and our computer systems, respectively, and for that I am very grateful. I also appreciate the assistance Dian Buchness has given within the chemistry department.

Many other friends have provided support along the way, in particular Len and Shelley Mueller, Sara Meyer, Erin and Lawrence Jones, and Dr. Karen Fagin. They have made my stay at Caltech much more enjoyable than it would have otherwise been.

I am also indebted to the ARCS Foundation for financial support. Through their generosity, financial concerns were not uppermost in our minds and we were able to concentrate on our studies.

And last, but by certainly no means least, I wish to thank all (and I mean ALL) of my family for the support they have given. I know that without the support and confidence of my parents I would never have been able to achieve what I have. In addition, I am very lucky to have gained another mother and father who have generously taken me as their son.

Finally, I wish to thank my wife Laura, for all the support and love she has given. It has not always been easy surviving as two students, one in medicine and one in chemistry, but we have certainly made the best of it. And now, we've finally made it: we are the doctors Bierwagen, and damned proud of it!

Abstract

This thesis discusses work on two different subjects. First, results from computational studies of Ziegler-Natta catalysts are presented. Quantum mechanical calculations of model Ziegler-Natta catalysts X_2MR are described, where X is either Cl or the cyclopentadienyl (Cp) ligand, M is a group three transition metal or group four transition metal cation, and R is a hydrogen or alkyl group. It is found that complexes based on group four cations have pyramidal structures (the R group is not in the X_2M plane), whereas group three neutral complexes have planar structures. This difference in structure is considered in the context of syndiodirecting polymerization, leading to the conclusion that the group three metals are expected to show little, if any, syndiodirecting capabilities, while the group four cations, including thorium, are expected to show large syndiodirecting capabilities, in accord with experiments. Results from molecular mechanics simulations of zirconocene-based catalysts follow. These calculations are used to assess the steric demands of different ligand environments during propylene polymerization, to determine the relative importance of site and chain end control on the enantioface selectivity, both of which are found to be operative.

The second part of the thesis describes the development of concurrent algorithms for the computation of resonance matrix elements. The algorithms are described for two different models of concurrent computing: parallel and distributed. A general program design and architecture that facilitate the program development are described. The scaling of both algorithms with the number of processors is found to be nearly ideal.

Table of Contents

PART 1: COMPUTATIONAL STUDIES OF ZIEGLER NATTA CATALYSIS 1

CHAPTER I: INTRODUCTION TO ZIEGLER-NATTA CATALYSIS 2

Abstract *3*

Heterogeneous Catalyst Systems *4*

Homogeneous Catalyst Systems *7*

Active Sites 8

Effect of Co-Catalyst 9

Multicomponent vs. Single Component Catalysts 10

Mechanisms *10*

Polypropylene Polymerization: Regiochemistry of the Insertion *13*

Polypropylene: Stereopolymerization *13*

Basic Mechanisms of Stereopolymerization 13

Isotactic Polypropylene 17

Syndiotactic Polypropylene 18

Atactic Polypropylene 21

Hemi-isotactic Polypropylene 21

Block Isotactic Polypropylene 22

References *23*

CHAPTERII: QUANTUM MECHANICS INVESTIGATIONS OF GROUP THREE AND GROUP FOUR ZIEGLER-NATTA CATALYSTS 28

Abstract *29*

Introduction *30*

Computational Models *32*

Studies of Dichlorometal Hydride Models *33*

Cl_2ScH, Cl_2TiH^+ 33

Implications 34

Understanding the Geometries 35

MH and MCl Complexes 37

ClMH Complexes 39

Cl_2Sc and Cl_2Ti^+ Complexes 42
Cl_2MH Complexes 44
Studies of Cl_2MH Species for M=Y, Zr^+, La, Hf^+ 47
MH and MCl Complexes 48
MHCl Complexes 51
Analysis of Cl_2MH, M=Y, Zr^+, La, Hf^+ 52
Investigating Thorium for use in Syndiodirecting Catalysts 53
Studies of Dichlorometal Methyl Complexes *56*
Studies of Metallocene Species *57*
Conclusions *64*
Appendix: Calculational Details *71*
Methods 71
Basis Sets and Effective Core Potentials 74
Geometries 79
References *82*

CHAPTER III: MOLECULAR MECHANICS INVESTIGATIONS OF SYNDIOSPECIFIC ZIRCONOCENE-BASED ZIEGLER-NATTA CATALYSTS 86
Abstract *87*
Introduction *88*
Stereochemical Notation *90*
Previous Molecular Mechanics Calculations *91*
Developing Force Fields *93*
M-Cp Interaction 98
M-Olefin Binding 99
General Considerations 99
Results and Discussion *100*
Isopropyl(cyclopentadienyl-1-fluorenyl)zirconium system 100
Cp_2Zr and Cp^*_2Zr 103
Isopropyl(3-methyl-1-cyclopentadienyl-1-fluorenyl)zirconium system 105
CpCp*Zr 108

Appendix: Force Field Description *111*
Bond Terms 112
Angle Terms 112
Torsion Terms 113
van der Waals Terms 113
Electrostatic Terms 114
References *116*

CHAPTER IV: CONCLUSIONS OF THE COMPUTATIONAL STUDIES 119
Abstract *120*
Introduction *121*
Summary of Results *122*
Rules for Design of Effective Syndiodirecting Catalysts *123*
Proposed Catalysts *123*
References *125*

PART 2: CONCURRENT RESONANCE CALCULATIONS 126

CHAPTER V: INTRODUCTION AND DESCRIPTION OF PROGRAM 127
Abstract *128*
Introduction *129*
Background Theory *133*
Resonance Method *135*
Program Design for Resonance Program *138*
C++ Programming Language 138
The Tcl Interpreter 139
Tcl Enabled Objects 140
Program Architecture for Resonance Program *142*
References *145*

CHAPTER VI: THE PARALLEL AND DISTRIBUTED ALGORITHMS 146
Abstract *147*
Parallel Computing: Introduction *148*
Algorithm *151*
Goals 151
Background Notation 152

Parallel Algorithm: Description *152*
Pipeline Algorithm 153
Truncated Wavefront 156
Load Balancing 160
Distributed Computing: Introduction *164*
Algorithm *165*
Program Design *167*
References *170*

CHAPTER VII: RESULTS AND CONCLUSIONS 171
Abstract *172*
Timing Results *173*
Parallel Calculation 173
Distributed Calculation 176
Chemical Results *177*
Computational Details 177
$C_{10}H_6$ 177
Cyclopentadienyl Anion 179
References *181*

Part 1:

Computational Studies of

Ziegler-Natta Catalysis

Chapter I

Introduction to Ziegler-Natta Catalysis

Abstract

This chapter presents an overview of Ziegler-Natta catalysis, both heterogeneous and homogeneous, to provide context for the computational studies and results described in Chapters II, III, and IV.

Heterogeneous Catalyst Systems[1]

Ziegler and coworkers[2] originally discovered in their work with aluminum organometallic complexes that small amounts of added transition metals would efficiently catalyze ethylene polymerization. Further investigation proved that the most efficient catalyst systems consisted of titanium compounds and the aluminum alkyls. Natta and coworkers[3] developed the solid titanium chloride catalysts and extended these catalysts to propylene polymerization. Their studies revealed that the resulting polypropylene can be separated into less and less soluble fractions, culminating in solids that are completely insoluble in boiling heptane. This remaining solid has a very high melting point (about 170° C), indicating a high crystallinity. X-ray diffraction studies reveal that the position of these methyl pendant groups on the polymer backbone have a remarkably high regularity, one not seen previously. Indeed, Natta and coworkers had to define new terms to describe such a regular pattern (or tacticity) in polymers: isotactic if the pendant groups were on the same side of the chain,[4] syndiotactic if they were on alternating sides of the chain,[5] and atactic if there were no regularity to the groups (see Figure 1).

The original stereopolymers produced with these heterogeneous catalysts were isotactic, but recent developments have led to heterogeneous catalysts, based on both $TiCl_3$ and VCl_4, that can produce syndiotactic products* as well.[6] Further improvements to the original catalysts generated higher yields, greater stereoregularity of the resulting polymer, and longer lasting catalysts. Most catalyst systems involve the main catalyst ($TiCl_3$ (α, β, γ, or δ) or $TiCl_4$), a co-catalyst (generally $AlCl_xR_{3-x}$), catalyst modifiers (often a Lewis base), solvent, and monomer. The most efficient modern heterogeneous catalysts are so-

---

*Natta and coworkers also discovered homogeneous catalysts that could polymerize syndiotactic polypropylene: Natta, G.; Pasqon, I.; and Zambelli, A. *J. Am. Chem. Soc.*, **1962**, *84*, 1488. Natta, G.; Zambelli, A.; Lanzi, G.; Pasquon, I.; Mognaschi, E. R.; Segre, A. L.; Centola, P. *Makromol. Chem.*, **1965**, *81*, 161.

called supported catalysts, in which small $TiCl_4$ particles are well dispersed within a support, often $MgCl_2$.

Figure 1. Polypropylene of Different Tacticities (a) Isotactic (b) Syndiotactic (c) Atactic

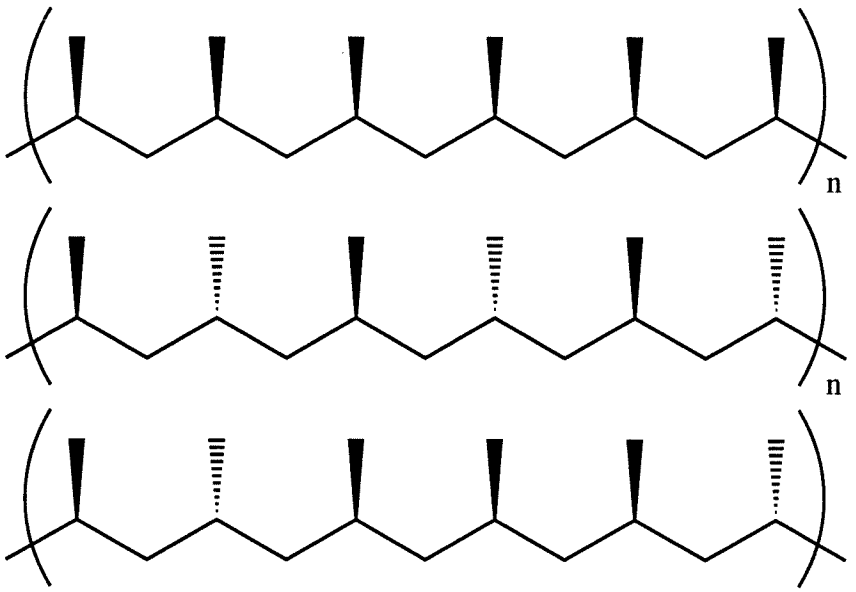

Since its discovery, Ziegler-Natta polymerization of olefins has evolved into a major industrial process, producing tens of billions of pounds of polyethylene and polypropylene per year. Ziegler-Natta catalysts produce over 60% of the total polyolefins produced, a market which is expected to grow by about 5% in the upcoming years (well exceeding the 3% growth expected for other plastics).[7] For their work on the catalysts bearing their name, Ziegler and Natta were awarded the Nobel Prize in Chemistry in 1963.

It is thought that the co-catalyst performs at least three, and perhaps five, roles in the polymerization.[8] First, the aluminum agent alkylates the titanium surface, presumably forming the active sites. This function has been directly observed by the exchange of chlorine for ethyl groups in the interaction between $TiCl_3$ and $AlEt_3$.[9] Second, the aluminum has been shown to dehalogenate the titanium to form a possibly cationic site, while acting as a counterion. Third, the co-catalyst is most likely associated with catalyst centers, and may play either a direct or indirect role in the polymerization reaction. Fourth, the co-catalyst may serve as a chain transfer agent. Fifth, oxygen and water are known to

poison the catalysts, and the co-catalyst is thought to function as an oxygen scavenger during polymerization reactions. In addition, there are still many subtle details involved in the catalyst–co-catalyst interaction that need to be understood: for example, at high enough concentrations, or at long enough times, the co-catalyst can act as a catalyst poison.

In addition to the uncertainty surrounding the co-catalyst, it is still not known exactly what the active site (or sites) on the titanium surface looks like (either structurally or electronically). There are four known forms of $TiCl_3$ solid (α, β, γ, and δ), and the most active catalysts are prepared by milling a given amount of $TiCl_3$ (forming the δ-$TiCl_3$), thus forming particles with large surface to volume ratios and surfaces with a variety of different titanium sites. It is generally accepted that the active sites are defects, with a titanium exposed on the surface missing its full complement of surrounding chlorines.[13] However, exactly what electronic and structural environment comprises an active site is still unknown.

It is thought that more than one active site exists. Certain additives, (*i.e.*, Lewis bases such as ethyl benzoate), can increase the isotacticity of the resulting polymer[†] while concurrently decreasing the activity of the catalyst. Presumably the Lewis base poisons the atactic sites, thus leading to a lower overall activity (due to fewer polymerization sites) but higher tacticity; it may also increase the activity of the isospecific sites,[10] although this fact is still open for debate. Exactly which sites the additive poisons, and what they look like, are still unknown.

There have been a number of sites proposed that would polymerize propylene isotactically.[11] Two of the more popular are shown in Figure 2, the tetracoordinate and the tricoordinate sites. Plausible mechanisms have been proposed for both sites.

[†]But, according to Busico, V., *et al.* in reference 6c, ethyl benzoate can also increase the *syndiotacticity* of the resulting polymer.

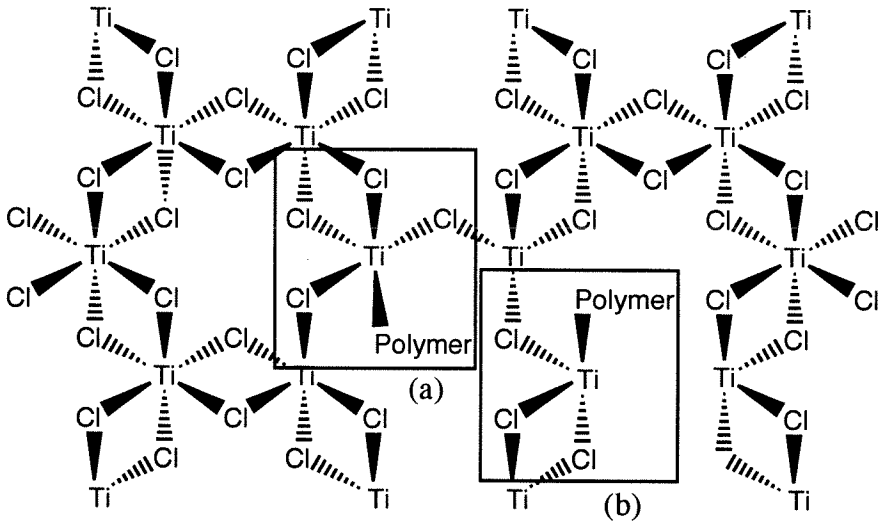

Figure 2: Representative Active Sites on α -$TiCl_3$ Surface with a Growing Polymer Chain (a) Tetracoordinate Site (b) Tricoordinate Site

Many elegant studies have been performed on heterogeneous catalysts, linking polymerization characteristics to certain structural or mechanistic features of the catalyst. These include statistical analyses of the polymer microstructure to determine the stereochemical control[12] and kinetic studies of the polymerization reaction.[13] However, most studies have been indirect, in that a catalyst is synthesized, a polymerization reaction is run, and then the resulting polymer characteristics (chain length, polydispersity, microstructure, etc.) are analyzed; the catalyst surface itself, which contains the active sites, has proven particularly difficult to study.[14] In addition, most studies are complicated by the fact that the variables controlling the polymerization reactions are often difficult to isolate, and are changed simultaneously between different polymerization runs, leading to many difficulties interpreting the experimental results. No matter how carefully the preparations are controlled, in general there will be a variance in catalyst features.

Homogeneous Catalyst Systems

Not long after the original discoveries of the heterogeneous polymerization catalysts, Breslow and Newburg[15] and Natta and coworkers[16] discovered that titanocene

catalysts would polymerize ethylene in the presence of alkylaluminum chlorides. These original homogeneous catalysts have low activities and do not polymerize propylene and thus are not useful commercially.[1d] They were, however, regarded as good models for the heterogeneous systems. As was stated earlier, studies of the heterogeneous systems have been hampered by a lack of knowledge of the active site or sites; these original homogeneous systems provided evidence for the structure of an active site.

Homogeneous catalyst technology took a great leap forward by the discovery of Sinn and Kaminsky[1d,17] that using methyl-alumoxanes (MAO) as a co-catalyst rather than aluminum alkyls resulted in catalyst systems having activities (about 10^6 g polyethylene/(g Zr • h)) much closer to heterogeneous systems. MAO's are curious in that they are synthesized by reacting aluminum alkyls with water, previously thought to be a catalyst poison;[‡] they are ill defined structurally, consisting of the basic structural unit -Al(O)(CH_3)- in linear and ring polymer chains of unknown length. The original discovery of the MAO co-catalysts was impressive. However, technical considerations (high flammability of MAO's, high cost of $AlMe_3$, and large amounts of MAO necessary (10^4-fold excess))[7] and mechanistic considerations (assuming that the active site is the metallocene, the large excess of MAO required hampers detailed studies of the active site) have stimulated the search for suitable replacements.

Active Sites

It has generally been accepted, based on experimental evidence from the metallocene catalyst systems, that the active site for polymerization is the transition metal in the metallocene. Dyachkovshi and coworkers,[18] based on kinetic measurements, proposed that the insertion takes place on a metallocenium alkyl species, and Eisch and coworkers

---

[‡]Although, Breslow and Newburg (ref 15a and 14b) reported that titanocene/aluminum alkyl ethylene polymerization was greatly improved if the ethylene contained traces of oxygen; they speculated that the oxygen was important to forming a Ti(IV) complex.

studied the insertion of phenyl-trimethylsilyl-acetylene into $Cp_2TiCl_2/AlCl_2Me$, producing the Cp_2Ti(1-phenyl-2-methyl-2-trimethylsilyl) ethenyl cation.[19] This evidence suggested that the catalytically active species in solution is the 14 electron, bis(cyclopentadienyl)metal alkyl cation, $[Cp_2M–R]^+$, where M is a group four metal. However, until recently, the nature of the active species has never been proven conclusively.

Recent advances in understanding the structure of the active catalyst have been facilitated by the discovery of relatively well-defined Ziegler-Natta α-olefin polymerization systems: (1) simpler two-component systems based on group 4 metallocene dialkyls with a stoichiometric (or nearly stoichiometric) amount of activator such as $[C_6H_5(CH_3)_2NH^+]$ $[B(C_6F_5)_4^-]$,[20] $[(C_6H_5)_3C^+]$ $[B(C_6F_5)_4^-]$,[21] and $B(C_6F_5)_3$,[22,23] and (2) single component catalysts such as Lewis base-adducts of cationic group 4 metallocene alkyls.[24] In addition, NMR studies by Sishta, Mathorn, and Marks[25] provide further evidence for the metallocenium alkyl species as the active catalyst.

Effect of Co-catalyst

Given the evidence above that the active site is the cationic metallocenium alkyl, the most obvious purposes of the co-catalyst are to alkylate the metallocene (if necessary) and form the metallocenium cation. However, especially with the aluminum alkyl co-catalysts, there is still some speculation that the aluminum is intimately involved in the polymerization reaction. Recent experiments by Stille and coworkers[26] have demonstrated that, while there is strong catalyst–co-catalyst interaction in the systems $Cp_2TiClR \bullet EtAlCl_2$ and $Cp_2TiClR \bullet MgX_2$, it is the Ti center that is responsible for polymerization and not the aluminum or magnesium.

Bochmann and coworkers have been performing studies of the effect of different counterions on the catalyst activity, stereospecificity, and molecular weight of the resulting polymers.[27] It appears that with the non-coordinating counterions, the stereospecificity degraded dramatically with increasing temperature, as opposed to using MAO as a

counterion, in which the stereochemistry did not depend as strongly on the polymerization temperature.[27a] They also studied the differences in competition between solvent, counterion, and monomer for the open coordination site.[27c] The differences in solvent are small and there appears to be a slight difference between ions: $B(C_6F_5)_4^-$ coordinates less than $B(C_6H_3(CF_3)_2)_4^-$,.

Multicomponent vs. Single Component Catalysts

While the discovery of the homogeneous catalysts was a great step forward towards a well defined active site amenable to study, the group four based catalysts still suffer from the fact that a co-catalyst is necessary. There has been much work recently in developing single component, well defined catalysts. Successful catalysts are based on isoelectronic group three and actinide metallocene complexes, and can polymerize ethylene and in some cases propylene.[28] Development of these catalysts has given further credence to the idea that the active species for the group four metals is the 14 electron metallocenium alkyl cation. In addition, these catalysts have allowed detailed studies of the basic polymerization reactions, initiation, propagation, and termination.

One reason these catalyst systems have been used so successfully for studying the polymerization reactions is that they are not nearly as efficient as the group 4 cationic systems. While the activities of the homogeneous group four cationic systems (typically on the order of 10^6 g polymer/(g catalyst • h)) can rival heterogeneous catalyst activities, the group three catalysts have much more modest activities, typically of the order 10^3 g polymer/(g catalyst • h).[29]

Mechanisms

The most widely accepted mechanism for the polymerization was put forth by Cossee and Arlman.[30] They postulated that the polymerization is simply a complexation of the olefin to a metal center followed by an insertion into the metal carbon bond, resulting in

a new metal carbon bond and an extension of the polymer chain. They predicted the nuclear positions shown based on the principle of least nuclear motion (Figure 3).

Note that this mechanism does not include the co-catalyst. Mechanisms have been proposed that include the co-catalyst explicitly[31] or two olefins simultaneously (the reactions are second order in monomer).[32] Results from the metallocene catalysts, however, prove that the aluminum alkyl co-catalyst is not directly involved in the polymerization and that the polymerization is first order in monomer.[20-25,28a, 33]

Figure 3. Cossee-Arlman Mechanism for Ziegler-Natta Polymerization

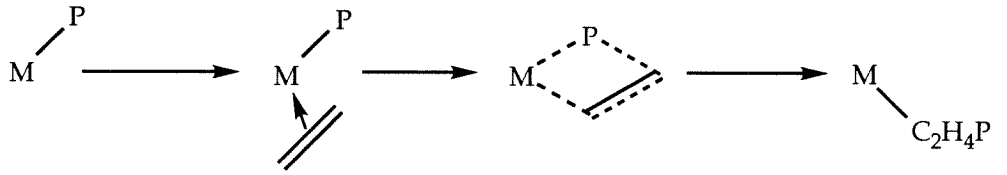

It is known that the barrier for this reaction must be exceptionally low, given the observed rates of polymerization (it is determined to be about 6-12 kcal/mol).[34] In the transition state, the sp^3 carbon must be pentacoordinate; evidence suggests that such a bonding situation would lead to higher barriers (20 kcal/mol or higher).[35] Because of this discrepancy, modifications to the Cossee-Arlman mechanism have been proposed. In these catalysts the metal is quite Lewis acidic, and these modifications allow the metal to be "solvated" in some manner. Green and Rooney[36] suggested that the α-carbon transfers a hydride to the metal, forming a metal-carbon double bond. In this case, the polymerization mechanism would be metathesis-like. Although evidence suggests that this mechanism may be operative for catalysts involving metals later in the transition series,[37] formally this mechanism is impossible for d^0 metals, as they would be unable to form the required M-H bond.

A modification of the strict hydride-transfer model was suggested by Green and coworkers.[38] In this case, the metal and the carbon "share" the hydrogen in a three-center,

two-electron bond, known as an α-agostic bond (Figure 4), in the transition state; such a bond would lower the insertion barrier. As Grubbs and coworkers have suggested, one way to experimentally probe for this α-agostic assistance is via the presence or absence of kinetic isotope effects.[39] They performed an internal cyclization-competition experiment in which the α-carbon was chiral, containing a hydrogen, a deuterium, and another carbon; if there were an α-agostic assisted mechanism, there would be a preference for the hydrogen in the agostic position. Their experiment using titanium catalysts revealed no such preference, leading them to conclude that the α-agostic assisted mechanism was not operative. However, more recent experiments using scandium[40] and zirconium[41] reveal kinetic isotope effects of about 1.2-1.3,[§] suggesting that α-agostic assistance is occurring. It is unlikely, though possible, that completely different mechanisms are operative in the two cases; the presence or absence of a kinetic isotope effect may be due to a difference in degree, rather than kind.

Figure 4. α-agostic Assisted Ziegler-Natta Insertion Mechanism

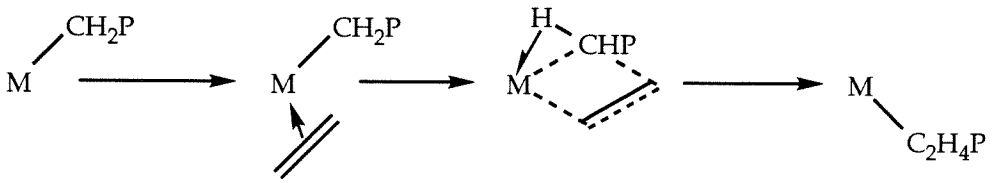

[§]Note that the data for the zirconium systems is contradictory. In certain cases, the α-agostic mechanism appears operative (ref. 41), while in other cases (cyclization experiments similar to the Grubbs experiments (ref. 39)) there appears no α-agostic assistance (Brintzinger, unpublished results)

Polypropylene Polymerization: Regiochemistry of the Insertion

In propylene polymerization, there are two possible regiochemistries with which the propylene can insert: the 1,2 insertion, in which the monomer inserts to give a secondary metal-carbon bond, and the 2,1 insertion, in which the monomer inserts to give a tertiary metal-carbon bond. Repeated 1,2 or 2,1 insertions are called head-to-tail insertions, as the resulting polymer has alternating chiral, non-chiral carbon centers. In general, the homogeneous systems are less regiospecific that the heterogeneous catalysts,[42] although substitution of *ansa* metallocenes at the carbons α to the linking group can improve the regioregularity of the insertions.[43] Busico, *et al.*,[42] have shown that regioirregular insertions decrease the rate of propagation considerably, and estimate that up to 90% of the active sites in a catalyst system are in a dormant state cause by a 2,1 insertion.

Polypropylene: Stereopolymerization

Ewen discovered that the titanocene/MAO catalysts could polymerize polypropylene to give mildly isotactic polypropylene at low temperatures.[44] However, as homogeneous, metallocene based catalysts were developed, it was discovered that suitable substitution of the cyclopentadienyl rings can produce catalysts that produced stereoregular polymers at higher temperatures. Brintzinger and coworkers[45] developed a chiral catalyst system for polymerizing isotactic polypropylene, and Ewen and coworkers[46] developed catalysts for producing syndiotactic polypropylene.

Basic Mechanisms of Stereopolymerization

In order to polymerize propylene in a stereospecific manner, the catalyst must be able to discriminate between the prochiral faces (the *re* and *si* faces) of propylene in a regular manner. If the catalyst chooses the same olefin face on each insertion, then isotactic polypropylene is produced; each chiral carbon on the polymer backbone has a meso

relationship to the adjacent chiral centers (represented by *m*; see Figure 5). If the catalyst regularly chooses between the two prochiral faces, then syndiotactic polypropylene is produced. The chiral carbon centers have a racemic relationship to adjacent chiral centers (represented by *r*).

Figure 5. Stereopolymer Representations (a) Isotactic (b) Syndiotactic

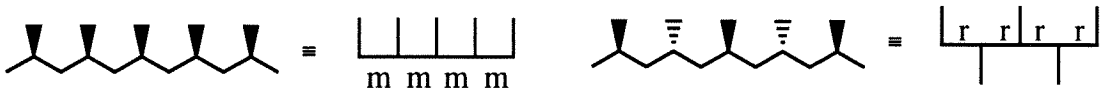

(a) (b)

There are two classical mechanisms for the discrimination between the two faces during olefin polymerization: enantiomorphic site control[47] and chain end control.[48] The site control mechanism states that the rigid, chiral ligand environment around the metal dictates exactly the enantioface selectivity of the olefin complexation and insertion. If an error occurs in the polymerization, the catalyst environment will force the subsequent insertions to be performed with the proper stereochemistry *relative to the catalyst*. Thus, an analysis of the dyads would indicate that two consecutive errors occurred (Figure 6).

The chain end control mechanism states that the chain adopts a particular conformation, based on the stereochemistry of the β-carbon, which in turn controls the enantioface selectivity of the olefin complexation and insertion. If an error occurs in the polymerization, the chirality of the β-carbon will be changed relative to the previous insertions, and the single "mistake" will be propagated (Figure 6). Generally, the two mechanisms are distinguished from each other based on dyad, triad, tetrad, or pentad analyses by looking for single or double mistakes.

More recent evidence and thinking has suggested that the actual control may be more subtle than is accounted for in the simpler theories.[49] If the two mechanisms can be thought of as the extremes of control, one in which the chain plays no role, and one in which the site plays no role, the actual control involves contributions from both

mechanisms, to a greater or lesser extent. Kawamura-Kuribayashi and co-workers[49a] report that computational models suggest the enantiomorphic site control occurs via the chain: the ligand environment around the metal confers a certain conformation to the chain, which in turn controls the enantioselectivity of the next insertion.

Figure 6. Polymer Chains With Misinsertion (a) Site Control (b) Chain Control

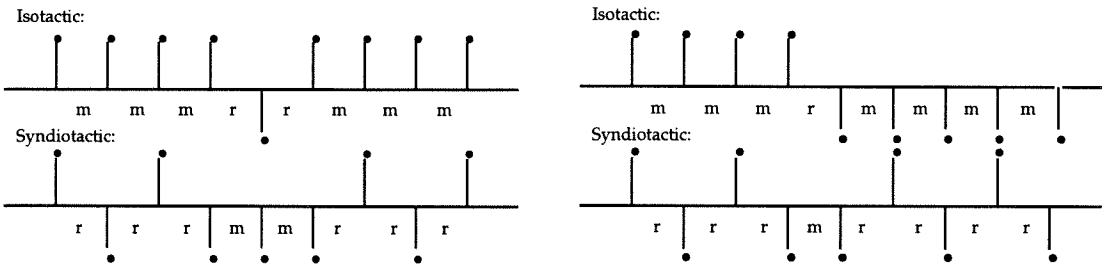

As Erker and coworkers point out, it is also possible that the two modes of control are working concurrently, giving a double stereo-differentiation.[50] Using unlinked metallocenes with a single, large substituent on each ring, they are able to produce isotactic polypropylene that could be classified as having both site control and chain control errors. By systematically varying the substituents, they are able to modify the extent of the two control mechanisms.[50b]

In regard to the stereospecificity of the metallocene complexes, a useful guide to thinking about and generalizing their stereodirecting mechanism was developed by Pino, Cioni, and Wei.[51] If one looks at the catalyst "head on," one can conceptually divide the complex into four quadrants (Figure 7). In general, isotactic catalysts have quadrants I and III filled with large, sterically demanding substituents and quadrants II and IV empty (or, II and IV filled and I and III empty). Syndiotactic catalysts have quadrants II and III filled, and I and IV empty. The ramifications of this guide will be discussed in the next section.

In all of the mechanisms, it is assumed that the stereochemistry of the β-carbon is preserved throughout the polymerization, and that any stereoerrors are due exclusively to

mis-insertions. Recent evidence suggests that epimerization of the α-carbon (Figure 8) can account for a significant number of the observed errors, especially at lower olefin concentrations.[52] Statistically, this epimerization cannot improve the stereochemistry of the resulting polymer. In fact, stereoselective polymerizations of d_1-propenes provide evidence that this epimerization is the dominant cause of stereoerrors.[41b] Thus, while the stereochemical error data can be used as a qualitative guide to the effectiveness of a catalyst, care should be taken when drawing quantitative conclusions from this data.

Figure 7. Division of Catalyst Wedge into Quadrants

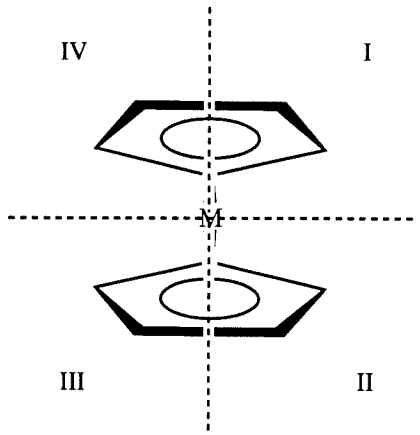

Figure 8. Epimerization Reaction Causing Stereoerrors

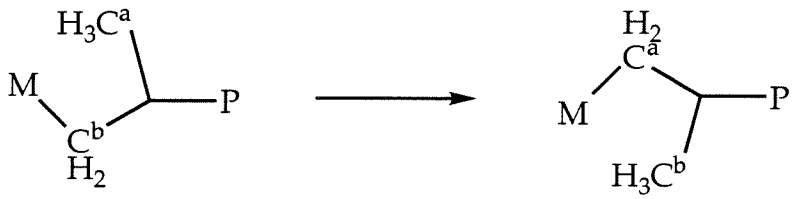

It has been frequently noted in the literature that increasing the stereoselectivity of a catalyst, by modifying the ligand environment, also improves its activity.[45,42,53] There are two causes for this: a greater rate of initiation or greater rate of polymerization; as kinetic studies are difficult with these catalysts, it is not straightforward to determine which one (or both) is causing the greater activities. However, assuming that the stereoselective catalysts

have a greater polymerization rate, one plausible explanation for this greater rate is that bulkier ligands, such as alkylated Cp rings or indenyl or fluorenyl groups, are more electron donating, thus increasing the electron density at the metal; it is proposed that increasing the electron density at the metal weakens the metal-ligand bonds.[54] It appears that increasing the metal electron density increases the rate of ethylene polymerization, although it is difficult to separate electronic and steric effects.[55]

Isotactic Polypropylene

Isotactic polypropylene, by virtue of its high stereoregularity, is a highly crystalline polymer with many desirable properties. It has a high melting point (183° C), high tensile strength, and excellent chemical and solvent resistance.[56] By virtue of its ease of synthesis (via heterogeneous catalysts), it is the most important stereopolymer of polypropylene commercially.

The first homogeneous isodirecting catalysts (chiral, *ansa*-metallocenes) were synthesized by Brintzinger[45] and Ewen.[57] A typical isodirecting, homogeneous catalyst precursor ([*rac*–ethylene bis(indenyl)]metal dichloride) is shown in Figure 9. As described above, the general requirements for the catalyst to be isodirecting are that it must have quadrants I and III filled and quadrants II and IV empty. Often the ligand system is such that the two ancillary ligands are the same. In this case, there are two sets of diastereomers, the racemic and the meso. Of these two, it is the racemic (*R* isomer shown in Figure 9) that is isospecific, the meso isomers producing atactic polymers. It is well accepted that this catalyst site controls the stereochemistry of the resulting polymer.

In order to produce isotactic poly-α-olefins, each insertion must use the same stereoface. For the active species, the two different lateral sites to which the monomer can bind are equivalent stereochemically. Given that the two lateral sites are stereochemically equivalent, the monomer should insert in the same manner from each side. As long as this equivalent insertion occurs, the resulting polymer will be isotactic. Conceivably, there are

two different ways in which the monomer can bind and insert: with the pendant group directed towards or away from the sterically demanding ligand. An initial guess might suggest that it would insert via the least sterically crowded path. However, it has been suggested that the polymer chain occupies the least sterically demanding locations, forcing the monomer to insert via a more sterically crowded path.[58]

Figure 9. Isodirecting Catalyst

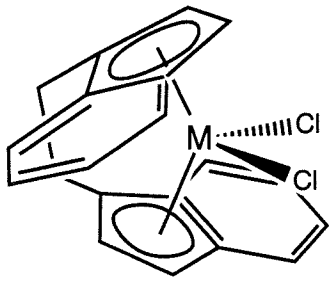

Experimental evidence by Waymouth and Pino, in examining the stereoselectivity of hydrogenation and polymerization, shows that different stereofaces are preferred for the two different reactions.[59] A straightforward interpretation of their results considers what groups are occupying the open sites in the ligand environment. In the hydrogenation reaction, the steric bulk of the hydrogen is small, allowing the monomer to insert via the least crowded path. In the polymerization reaction, the chain adopts a conformation such that it occupies the least sterically demanding location. As the chain is now occupying the site which the monomer pendant group occupied in the hydrogenation reaction, the monomer is forced to present the opposite stereoface to reduce contacts with the chain.

Syndiotactic Polypropylene

Like isotactic polypropylene, syndiotactic polypropylene is highly crystalline due to its stereoregularity but has a lower melting point. The melting point for pure, crystalline syndiotactic polypropylene is estimated to be about 30-40° C below that of isotactic polypropylene,[60] which is consistent with an experimental melting point of 140° for

syndiotactic polypropylene.[58a] Unlike isotactic polypropylene, highly crystalline syndiotactic polypropylene is readily soluble in ether and many hydrocarbon solvents at temperatures below 40° C.[60] While isotactic is superior to syndiotactic polypropylene in many properties, syndiotactic is less susceptible to autoxidation than isotactic polypropylene.[60]

The homogeneous syndiodirecting catalysts were first discovered by Ewen and coworkers[46,61] for the polymerization of polypropylene, and extended to other monomers.[62] In contrast to isotactic polymer, the production of syndiotactic polymer requires that a regular alternation between the two stereofaces occurs during the polymerization. A typical catalyst precursor (isopropyl[cyclopentadienyl-1-fluorenyl]metal dichloride) (^{i}Pr(Cp Flu)MCl_2) is shown in Figure 10; the requirements for syndiotactic polymerization appear to be that the ligand environment fills quadrants II and III, leaving quadrants I and IV empty (see above). It is interesting to note that, unlike the isodirecting catalysts, the syndiodirecting catalysts are not chiral, and thus would not be expected to exhibit enantiomorphic site stereocontrol. However, given that the active species is the species is the metallocenium alkyl cation, the catalyst will be chiral *if the alkyl group occupies a lateral site in the complex* (leaving the other lateral site unoccupied for monomer complexation). These two lateral positions of the catalyst are stereochemically different, so that inserting from either side will result in a different stereochemistry of the polymer.

Figure 10. Syndiodirecting Catalyst

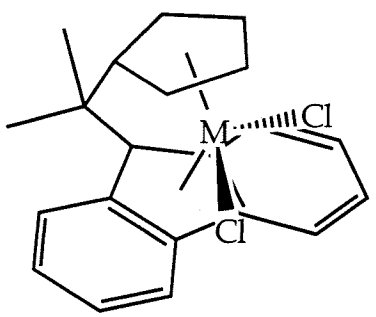

It is still not well accepted what features control the stereoselectivity of the syndiospecific catalysts. An attractive mechanism put forward by Ewen and coworkers[58a] is shown in Figure 11. The basic feature of this mechanism is that the polymer regularly alternates from one side to the other relative to the catalyst, this alternation forcing the monomer to insert from alternating sides. Assuming, as was done for the isotactic case, that the monomer inserts in the same manner relative to the sterically crowded/empty quadrants, the alternation of sides will regularly choose between the two different stereofaces of the monomer, resulting in syndiotactic poly-α-olefins.

Figure 11. Ewen Mechanism for Syndiotactic Polymerization

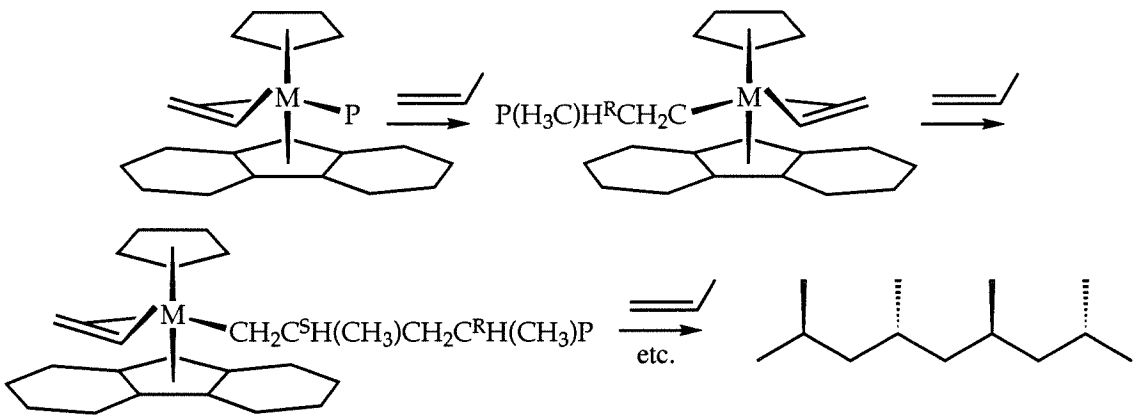

Ewen *et al.*[57a] argued that this mechanism, a site controlled mechanism, is consistent with the experimental evidence: the majority of the errors in the polymer were of the simultaneous-double type (see above), indicative of classical site control. However, there are two main problems with this mechanism: the alternation implicit in the Cossee-Arlman mechanism is assumed to be operative; no evidence for such a motion has existed. Also, if the alternation is truly what is governing the stereochemistry of the insertion, then a mistake (assumed to be an insertion without a polymer motion) would tend to give single errors, rather than double errors. Ewen *et al.* argued that the most probable errors were due not to lack of polymer motion, but to an enantioface selectivity error, leading to the double errors associated with site control. The evidence suggests that single and double

errors occur with similar frequencies.[58,63] Although the Ewen mechanism has problems, no other mechanism has been proposed to account for the syndiodirecting capabilities of the catalysts.

Atactic polypropylene

In the presence of no stereo-directing forces, α-olefins polymerize with a random stereochemistry; the resulting polymer is called atactic. The resulting polymer is amorphous and soft, with little strength. Even though it is the easiest polymer to produce, it has few uses.[56]

Hemi-isotactic polypropylene

A curious polymer that has been synthesized by Ewen, *et al.*,[58] is known as hemi-isotactic, which is shown with its catalyst in Figure 12. In this case, the polymer has an alternating random and stereoregular insertion. Note the similarity between the syndiodirecting catalyst precursor and this catalyst precursor. The only difference is the β-methyl substitution on the cyclopentadienyl ring. The existence of this catalyst gives further credence to Ewen's migratory syndiotactic polymerization mechanism, as it is quite difficult to explain this stereopolymerization by any chain control mechanism. Because three of the four quadrants are filled, the most likely chain conformation would position the chain so that it occupies the least sterically crowded quadrant. In this case, only atactic polymer would be expected. According to Ewen's mechanism, the polymer would still migrate, regardless of the resulting steric environment. When the polymer is residing on the crowded side, a stereoregular insertion would be anticipated; when the polymer is residing on the emptier side, an insertion of indeterminate stereochemistry would be expected. The regular insertions, being on the same side, would have the same isotactic stereochemistry.

Figure 12. Hemiisotactic (a) Catalyst (b) Polymer

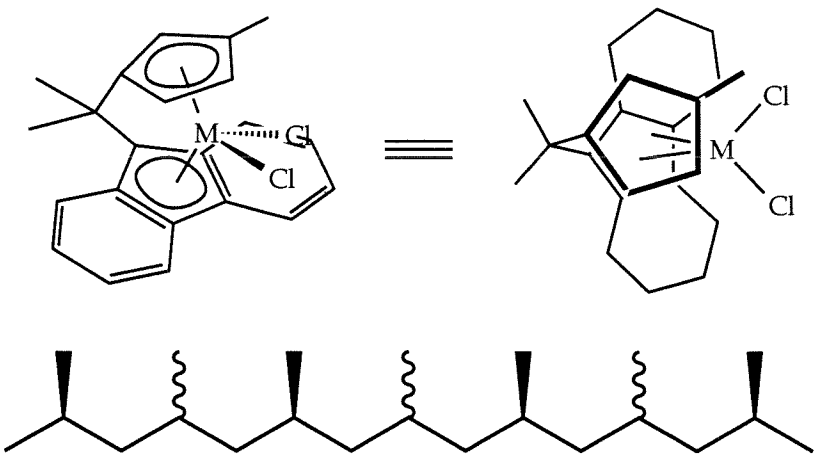

(a)

(b)

Block Isotactic-Atactic

Recently, Waymouth and Coates have described the synthesis of a polymer that has alternating blocks of isotactic and atactic polypropylene.[64] This polymer combines the thermoplastic properties of isotactic polypropylene with the elastomeric properites of atactic polypropylene, giving a rubbery product. The catalyst system that produces these block polymers is similar to the *ansa*-isodirecting catalysts: it consists of a bis(indenyl)zirconiumdichloride (Figure 13) precursor with a MAO co-catalyst. However, in this case the indenyl ligands are unlinked, allowing rotation around the Zr-indenyl bond so that the catalyst can isomerize between the meso and racemic isomers. In addition, the indenyls are substituted at the 2 position to retard the rate of rotation, allowing the catalyst to produce the polymer with the observed properties.

Figure 13. Catalyst with Oscillating Stereocontrol (a) Isodirecting Conformation (b) Non-stereodirecting Conformation

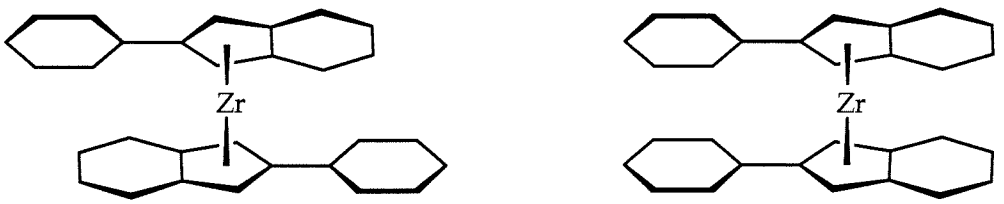

(a) (b)

References

1. For a more thorough review of heterogeneous systems, see for example (a) Kissin, Y. *Isospecific Polymerization of Olefins*, Springer-Verlag: New York, 1985. (b) Minsker, K. S.; Karpasas, M. M.; Zakov, G. E. *Rev. Macromol. Chem. Phys.*, **1987**, *C27*, 1. (c) Gavens, P. D.; Bottrill, M.; Kelland, J. W.; McMeeking, J. *Comprehensive Organometallic Chemistry, vol 3*. (d) Sinn, H.; Kaminsky, W. *Adv. Organomet. Chem.*, **1980**, *18*, 99.
2. Ziegler, K.; Holzkamp, E.; Breil, H.; Martin, H. *Angew. Chem.*, **1955**, *67*, 541.
3. Natta, G. *Makcromol. Chem.*, **1955**, *16*, 213.
4. Natta, G. *J. Polym. Sci.*, **1955**, *16*, 143.
5. Natta, G. *Chim. Ind.*, **1955**, *37*, 888.
6. See for example (a) Zambelli, A.; Natta, G.; Pasquon, I. *J. Poly. Sci., Part C.*, **1963**, *4*, 411. (b) Zambelli, A.; Locatelli, P.; Provasoli, A.; Ferro, D. R. *Macromolecules*, **1980**, *13*, 267. (c) Busico, V.; Corradini, P.; DeMartino, L. *Makromol. Chem., Rapid Comm.*, **1990**, *11*, 49.
7. Zucchini, U.; Dall'Occo, T.; Resconi, L. *Ind. J. Tech.*, **1993**, *31*, 247.
8. Ref.1a, pp 112-153, and references therein.
9. Ref. 1a, pp 109-118.
10. (a) Cheng, H. N. *Makromol Chem., Theory Simul.*, **1993**, *2*, 901. (b) Sacchi, M. C.; Tritto, T.; Locatelli, P. *Prog. Polym. Sci.*, **1991**, *16*, 331. and references therein.
11. (a) Ref. 1a, pp. 372-428 and references therein. (b) Corradini, P.; Barone, V.; Fusco, R.; Guerra, G. *Gazz. Chim. Ital.*, **1983**, *113*, 601.
12. See for example Busico, V.; Corradini, P.; DeBaisio, R. *Makromol. Chem.*, **1992**, *193*, 897.
13. Ref. 1a, pp 1-93.
14. Ref 1a, pp 118-122.
15. (a) Breslow, D. S.; Newburg, N. R. *J. Am. Chem. Soc.*, **1957**, *79*, 5072. (b) Breslow, D. S.; Newburg, N. R. *J. Am. Chem. Soc.*, **1959**, *81*, 81.

16. (a) Natta, G.; Pino, P.; Mantica, E.; Danusso, F.; Mazzanti, G.; Peraldo, M *Chim. Ind. (Milan)*, **1956**, *38*, 124. (b) Natta, G.; Pino, P.; Mazzanti, G.; Giannini, U.; Mantica, E.; Peraldo, M. *Chim. Ind. (Milan)*, **1957**, *39*, 19. (c) Natta, G.; Pino, P.; Mazzanti, G.; Giannini, U. *J. Am. Chem. Soc.*, **1957**, *8*, 612.

17. (a) Sinn, H.; Kaminsky, W.; Vollmer, H. J.; Woldt, R. *Angew. Chem., Int. Ed. Engl.*, **1980**, *19*, 390. (b) Sinn, H.; Kaminsky, W. *Adv. Organomet. Chem.*, **1980**, *18*, 137. (c) Hervig, J.; Kaminsky, W. *Polym. Bull*, **1983**, *9*, 464. (d) Kaminsky, W.; Lüker, H. *Makromol. Chem., Rapid. Commun.*, **1984**, *5*, 225. (e) Kaminsky, W. *Naturwissenshaften*, **1984**, *71*, 93.

18. Dyachkovski, F. S.; Shilova, A. K.; Shilov, A. E. *J. Polym. Sci.*, **1967**, *16*, 2333.

19. Eisch, J. J.; Piotrowski, A. M.; Brownstein, S. K.; Gabe, E. J.; Lee, F. L. *J. Am. Chem. Soc.*, **1985**, *107*, 7219.

20. (a) Hlatky, G. G.; Turner, H. W.; Eckman, R. R. *J. Am. Chem. Soc.*, **1989**, *111*, 2728. (b) Turner, H. W. European Patent Application 2277004, 1988.

21. (a) Ewen, J. A.; Elder, M. J. European Patent Application 426,638, 1991. (b) Chien, J. C. W.; Tsai, W. M.; Rausch, M. D. *J. Am. Chem. Soc.*, **1991**, *113*, 8570.

22. Ewen, J.; Elder, M. J. European Patent Application 427,697, 1991.

23. Xinmin, Y.; Stern, C.; Marks, T. *J. Am. Chem. Soc.*, **1991**, *113*, 3623.

24. (a) Jordan, R. F.; Bradley, P.; Baenziger, N. C.; LaPointe, R. E. *J. Am. Chem. Soc.*, **1990**, *112*, 1289. (b) Jordan, R. F.; LaPointe, R. E.; Bradley, P. K.; Baenziger, N. *Organometallics*, **1989**, *8*, 2892. (c) Eshuis, J. J. W.; Tan, Y. Y.; Meetsma, A.; Teuben, J. H.; Renkema, J.; Evens, G. G. *Organometallics*, **1992**, *11*, 362. (d) Jordan, R. *J. Chem. Ed.*, **1988**, *65*, 285.

25. Sishta, C.; Hathorn, R. M.; Marks, T. J. *J. Am. Chem. Soc.*, **1992**, *114*, 1112.

26. (a) Barta, N. S.; Kirk, B. A.; Stille, J. R. *J. Organomet. Chem.*, **1995**, *487*, 47. (b) Barta, N. S.; Kirk, B. S.; Stille, J. R. *J. Am. Chem. Soc.*, **1994**, *116*, 8912. (c) Young, J. R.; Stille, J. R. *J. Am. Chem. Soc.*, **1992**, *114*, 4936.

27. (a) Bochmann, M.; Lancaster, S. J. *Makromol. Chem., Rapid Commun.*, **1993**, *14*, 807. (b) Bochmann, M. *Angew. Chem., Int. Ed. Engl.*, **1992**, *31*, 1181. (c) Bochmann, M.; Lancaster, S. J. *J. Organomet. Chem.* , **1992**, *434*, C1.

28. (a) Watson, P. L. *J. Am. Chem. Soc.*, **1982**, *103*, 337. (b) Burger, B. J.; Thompson, M. E.; Cotter, W. D.; Bercaw, J. E. *J. Am. Chem. Soc.*, **1990**, *112*, 1566. (c) Jeske, G.; Lauke, J.; Mauermann, J.; Sweptson, P. N.; Schumann, H.; Marks, T. J. *J. Am. Chem. Soc.*, **1985**, *107*, 8091. (d) Coughlin, E. B.; Bercaw, J. E. *J. Am. Chem. Soc.*, **1992**, *114*, 7606.

29. Coughlin, E. B., Ph. D. Thesis, California Institute of Technology, 1994, p. 87.

30. (a) Cossee, P. *Tetrahedron Lett.*, **1960**, *17*, 12. (b) Cossee, P. *J. Catal.*, **1964**, *3*, 80. (c) Arlman, E.; Cossee, P. *J. Catal*, **1964**, *3*, 99. (d) Arlman, E. J. *J. Catal.*, **1966**, *5*, 178.

31. See for example: Novaro, O.; Blaisten-Barojas, E.; Clementi, E.; Giundi, G.; Ruiz-Vizeaya, M. E. *J. Chem. Phys.*, **1978**, *68*, 2337.

32. See for example Ystenes, M. *J. Catal.*, **1991**, *129*, 383.

33. Chien, J. C. *J. Am. Chem. Soc.*, **1959**, *81*, 86.

34. (a) Natta, G.; Pasqon, I. *Adv. Catal.*, **1959**, *11*, 1. (b) Chien, J. C. W. *J. Am. Chem. Soc.*, **1959**, *81*, 86.

35. See for example (a) Low, J. J.; Goddard, W. A., III *J. Am. Chem. Soc.*, **1984**, *106*, 6928. (b) Low, J. J.; Goddard, W. A., III *J. Am. Chem. Soc.*, **1984**, *106*, 8321. (c) Low, J. J.; Goddard, W. A., III *Organometallics*, **1986**, *5*, 609.

36. Green, M. L. H.; Rooney, J. J. *Chem Comm.*, **1978**, 604.

37. Turner, H. H.; Schrock, R. R. *J. Am. Chem. Soc.*, **1982**, *104*, 2331.

38. (a) Brookhart, M.; Green, M. L. H. *J. Organomet. Chem.*, **1983**, *250*, 395. (b) Laverty, D. T.; Roney, J. J. *J. Chem. Soc., Faraday Trans.*, **1983**, *79*, 869. (c) Brookhart, M.; Green, M. L. H.; Wong, L. *Prog. Inorg. Chem.*, **1988**, *36*, 1.

39. Clawson, L.; Soto, J.; Buchwald, S. L.; Steigerwald, M. L.; Grubbs, R. H. *J. Am. Chem. Soc.*, **1985**, *107*, 3377.

40. Piers, W. E.; Bercaw, J. E. *J. Am. Chem. Soc.*, **1990**, *112*, 9406.

41. (a) Krauledat, H.; Brintzinger, H. H. *Angew. Chem., Int. Ed. Engl.*, **1990**, *29*, 1412. (b) Leclerc, M. K.; Brintzinger, H. H. *J. Am. Chem. Soc.*, **1995**, *117*, 1651.

42. Busico, V.; Cipullo, R.; Chadwick, J.; Madder, J.; Sudmeyer, O. *Macromolecules*, **1994**, *27*, 7538.

43. Röll, W.; Brintzinger, H. H.; Rieger, B.; Zolk, R. *Angew. Chem., Int. Ed. Engl.*, **1990**, *29*, 279.

44. Ewen, J. A. *J. Am. Chem. Soc.*, **1984**, *106*, 6355.

45. Kaminsky, W.; Kulper, K.; Brintzinger, H. H.; Wild, F. R. W. P. *Angew. Chem., Int. Ed. Engl.*, **1985**, *24*, 507.

46. Ewen, J. A.; Jones, R. L.; Razavi, A.; Ferrara, J. D. *J. Am. Chem. Soc.*, **1988**, *110*, 6255.

47. (a) Sheldon, R. A.; Fueno, T.; Tsunstsugu, T.; Kurukawa, J. *J. Polym. Sci., Part B.*, **1965**, *3*, 23. (b) Doi, Y.; Asakuru, T. *Makromol. Chem.*, **1975**, *176*, 507.

48. Bovey, F. A.; Tiers, G. V. D. *J. Polym. Sci.*, **1960**, *44*, 173.

49. (a) Kawamura-Kuribayashi, H.; Koga, N.; Morokuma, K. *J. Am. Chem. Soc.*, **1992**, *116*, 8687. (b) Guerra, G.; Cavallo, L.; Moscardi, G.; Vacatello, M.; Corradini, P. *J. Am. Chem. Soc.*, **1994**, *116*, 2988.

50. (a) Erker, G.; Nolte, R.; Tsay, Y.-H.; Krüger, C. *Angew. Chem., Int. Ed. Engl.*, **1989**, *28*, 628. (b) Erker, G.; Nolte, R.; Aul, R.; Wilker, S.; Krüger, C.; Noe, R. *J. Am. Chem. Soc.*, **1991**, *113*, 7594. (c) Erker, G.; Fritze, C. *Angew. Chem., Int. Ed. Engl.*, **1992**, *31*, 199. (d) Erker, G. *Pure Appl. Chem.*, **1992**, *64*, 393. (e) Erker, G.; Psiorz, C.; Krüger, C.; Nolte, M. *Chem. Ber.*, **1994**, *127*, 1551.

51. Pino, P.; Cioni, P.; Wei, J. *J. Am. Chem. Soc.*, **1987**, *109*, 6189.

52. (a) Busico, V. *Abstr. Int. Symp. Stereosel. Polym.*, **1994**, 73. (b) Busico, V.; Cipullo, R. *J. Am. Chem. Soc.*, **1994**, *116*, 9329. (c) Balbontin, G.; Fait, A.; Piemontesi, F.; Resconi, L.; Rychlicki, H. *Abstr. Int. Symp. Stereosel. Polym.*, **1994**, 205.

53. Bochmann, M.; Lancaster, S. *Organometallics*, **1993**, *12*, 633.

54. (a) Henrici-Olivé, G.; Olivé, S. *Angew. Chem., Int. Ed. Engl.*, **1971**, *10*, 105. (b) Alelyunas, Y. W.; Jordan, R. F.; Echols, S. F.; Borkowsky, S. L.; Bradley, P. K. *Organometallics*, **1991**, *10*, 1406.

55. (a) Möhring, P. C.; Coville, N. J. *J. Mol. Catal.*, **1992**, *77*, 41. (b) Möhring, P. C.; Coville, N. J. *J. Organomet. Chem.*, **1994**, *479*, 1.

56. Odian, G. *Principles of Polymerization, 2nd Ed.*, John Wiley & Sons: New York, 1991, p. 580

57. (a) Ewen, J. *J. Am. Chem. Soc.*, **1984**, *106*, 6355. (b) Ewen, J.; Haspeslagh, L.; Atwood, J.; Zhang, H. *J. Am. Chem. Soc.*, **1987**, *109*, 6544.

58. (a) Ewen, J.; Elder, M.; Jones, R.; Haspeslagh, L.; Atwood, J.; Bott, S.; Robinson, K. *Makromol. Chem., Macromol. Symp.*, **1991**, *48-49*, 253. (b) Cavallo, L.; Guerra, G.; Vacatello, M.; Corradini, P. *Macromolecules*, **1991**, *24*, 1784.

59. Waymouth, R.; Pino, P. *J. Am. Chem. Soc.*, **1990**, *112*, 4911.

60. Youngman, E. A.; Boor, J., Jr. *Macromolecular Reviews*, Volume 2, Peterlin, A.; Goodman, M.; Okamura, S.; Zimm, B. H.; Mark, H. F., Eds., Wiley Interscience: New York, 1967, pp 33-69.

61. (a) Haftka, W.; Konnecke, K.; *J. Macromol Sci. Phys.*, **1991**, *B30*, 319. (b) Balbontin, G.; Dainelli, D.; Galimberti, M.; Paganetto, G. *Makromol Chem.*, **1992**, *193*, 693.

62. (a) Asanuma, T.; Nishimori, Y.; Ito, M.; Uchikawa, N.; Shiomura, T. *Polym. Bull.*, **1991**, *28*, 567. (b) DeRosa, C.; Venditto, V.; Guerra, G.; Pirozzi, B.; Corradini, P. *Macromolecules*, **1991**, *24*, 5645.

63. (a) Ewen, J. A.; Elder, M. J. *Makromol Chem., Macromol. Symp.*, **1993**, *66*, 179. (b) Razavi, A.; Ferrera, J. D. *J. Organomet. Chem.*, **1992**, *435*, 299.

64. Coates, G. W.; Waymouth, R. M. *Science*, **1995**, *267*, 217.

Chapter II

Quantum Mechanics Investigations

Of Group Three and Group Four

Ziegler-Natta Catalysts

Abstract

This chapter discusses the qualitative differences found in the ground state geometries of model homogeneous Ziegler-Natta catalysts based on group three and group four transition metals. It is found that for species with a general formula of X_2MR, where X is an electronegative ligand (either Cl or the cyclopentadienyl anion) and R is either a hydrogen or an alkyl, that complexes containing group three metals are planar, whereas complexes containing group four metals are non-planar. The significance of this result is discussed within the context of syndiospecific α-olefin polymerization. It is concluded that the group three catalysts will not be syndiodirecting, whereas the group four catalysts will be syndiodirecting. It is also concluded that thorium has the correct electronic structure for syndiodirecting catalysis.

Introduction

Due to its industrial importance, Ziegler-Natta catalysis has attracted intense study, both experimental and computational. The majority of previous *ab initio* computational work[1] has focused on the reaction pathway from metallocenium ion and monomer to the inserted product. As stated in Chapter I, it is accepted that the mechanism for this insertion (the Cossee-Arlman mechanism) involves coordination of the monomer to the metal, a four center transition state, and final insertion into the metal carbon bond. Whether it is energetically possible to have a low barrier for a reaction such as this, involving a pentacoordinate, sp^3 carbon in the transition state still appears to be an unsettled question. Much of the computational work has established that this pathway can be reconciled with the low barriers, but experimental work pointing to α-agostic assistance in the transition state[2] still remains an unsettled question computationally. Most computational studies arrive at the same conclusion: that barriers of about 10-12 kcal/mol are possible, thus apparently justifying the Cossee-Arlman mechanism.

It is important to note that the results of the computational studies tend to vary, particularly depending on the models used. The majority of earlier calculations[1b-e] employed a common approximation for much computational organometallic chemistry: the replacement of the computationally demanding cyclopentadienyl (Cp) rings with electronically similar chlorine atoms. Thus, much work has been done on $Cl_2TiCH_3^+ + C_2H_4 \rightarrow Cl_2TiC_3H_7^+$. In these cases, it appears that the transition state is late, with a barrier of about 10-15 kcal/mol. More recent calculations[1g] using the more sterically realistic Cp rings suggest that the insertion occurs without a barrier, although this result has been discounted as a calculational artifact.[1h]

The Cosee-Arlman mechanism has influenced much of the computational work. One major assumption of the Cossee-Arlman mechanism is that, if one considers the

reaction to occur in a plane, the polymer resides off center relative to the other ligands (Figure 1), allowing the monomer an empty coordination location to which it can complex; following olefin insertion, the polymer chain migrates, and the monomer consequently complexes from the other side.

Figure 1. Cossee-Arlman Mechanism

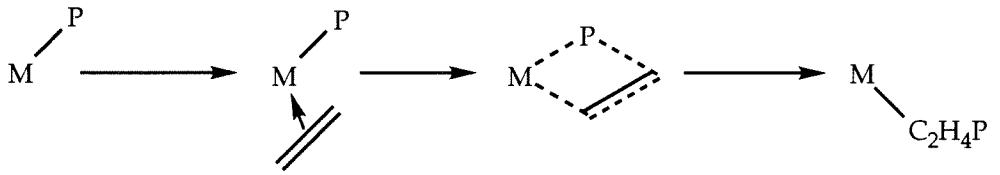

As discussed in Chapter I, this assumed migratory insertion has been used by Ewen, *et al.*,[3] as the basis for their syndiospecific polymerization reaction for metallocenium catalysts. However, the validity of the assumption has never been well established and there are many reasons to challenge it: sterically, the most favorable position for the polymer would be in the center of the metallocene wedge, which is where the alkyl group resides in structures of group three complexes.[4] The most common analogues to the monomeric metallocenium complexes that have been crystallographically characterized are the group 3 metallocenes, although there are examples of metallocenium complexes crystallized with their counterions.[5] In the case of the group three neutral metallocene complexes, the alkyl group resides in center of the plane as opposed to off to the sides as presumed by the Cossee-Arlman mechanism. In the case of metallocenium-anion structures, the alkyl group is sitting off to the side, although it is most likely sitting off to the side to accommodate the bulky counterion.

While simple steric arguments would predict that the polymer's residing off to the side would be thermodynamically unfavorable, the rate of monomer/solvent/counterion complexation may be faster than the rate of intramolecular reorganization. If this were the case, the Cossee-Arlman mechanisms would be justified on kinetic, rather than thermodynamic grounds. However, as the most favored position for the polymer is in the

center of the wedge, there is no barrier to rearrangement to the center (in fact, there is a energetic preference for this rearrangement). Thus, the reorganization is most likely as fast or faster than the monomer/solvent/counterion complexation, which means that the Cosee-Arlman mechanism must be justified on thermodynamic grounds.

Essentially, this geometric assumption of the Cossee-Arlman mechanism has never been proven, and its validity is questionable. Previous computational results[1a-e,h] indicate a possible resolution: it has been found that for model cationic catalysts, X_2MR^+ (X = Cl, Cp; M = Ti, Zr; R = H, CH_3), that the ground state geometry of this complex does not have all four atoms (Cl or Cp centroids, M, and H or C) in the same plane; instead, it is non-planar. This chapter will be devoted to understanding the geometries of the ground state complexes, for both the group three neutral and the group four cationic catalysts: understanding the geometries, the geometries' origins, and their ramifications.

Computational Models

As discussed in Chapter I, it is well accepted that the active species in solution for the homogeneous catalysts is a 14 electron metallocene species with the growing polymer chain. It is these monomeric, monometallic species that are modeled in the present study. However, these species are too large for rigorous electronic structure analyses, and simplifying approximations must be made.

The specific details of the calculations are discussed in the appendix to this chapter, although the approximations used are briefly discussed below. Simple model complexes are used to gain a full understanding of the geometries, to understand the origins and trends of the observed geometries, and through the knowledge gained to make predictions. In the case of these metallocene catalysts, these simple complexes are those that model the electronics of the complexes and ignore steric considerations. Once the electronic effects are understood, calculations that include the steric effects are performed to understand how these steric effects modify the understanding. The reasons for this are two-fold: (1) the

smaller the complexes, the more rigorous the electronic structure analysis and (2) if a separation of the two effects can be made, then their relative effects can be quantitatively discussed.

One important approximation that has been used in computational studies of related complexes is the modeling of the electronic effects of the cyclopentadienyl rings with chlorine atoms. The validity of this was first established by Brusich and Goddard,[6] through their comparison of the electronegativies and state splittings of the Cp rings and chlorines. Especially in early metal complexes, where the majority of the charge transfer is from the metal to the rings, with little backbonding to the metal, this should be a valid model.

Studies of Dichlorometal Hydride Models

Experimentally, metallocene catalysts involving the metals Sc, Y, Ti, Zr, Hf are known to polymerize olefins.[7] Formally, all of these catalysts are isoelectronic, 14 electron species with d^0 metals, so they would be expected to share similar geometric characteristics. Metallocenium catalysts have been synthesized using group four metals that are both isodirecting[8] and syndiodirecting.[9] While isodirecting catalysts have been synthesized using group three metals,[10] to date there are no examples of syndiodirecting catalysts involving group three metals. This difference will be used as a starting point to understand the origins of the syndiospecificity of the group four cationic catalysts.

Cl_2ScH, Cl_2TiH^+

The study will start with Sc and Ti^+, as in many senses these are the easiest metals to study: they have the smallest relativistic effects and have been well characterized experimentally. As stated above, these two metals are isoelectronic and their complexes are be expected to exhibit similar characteristics. However, they exhibit quite different ground state geometries (Table 1). Cl_2ScH has a planar geometry (and requires a 1.53 kcal/mol

energy increase to move the H out of the plane by 50°), whereas Cl_2TiH^+ has a nonplanar geometry with the hydrogen 84° out of the plane (with a planar structure 12.8 kcal/mol higher in energy).

Table 1. Ground State Geometries of Cl_2MH, M=Sc, Ti, and Ti^+

Species	R(M-H)	R(M-Cl)	θ(Cl-M-Cl)	ω(plane-H)	θ(Cl-M-H)
Cl_2ScH	1.74	2.36	139.1	0.0	110.4
Cl_2TiH^+	1.69	2.18	120.5	84.4	92.6
Cl_2TiH	1.68	2.32	147.8	0.0	106.1

Distances in Å, angles in degrees

Similar geometries have been found for other X_2MR^+ (X = Cl, Cp; M = Ti, Zr, Hf; R = H, CH_3) complexes.[1,11] However, little discussion has been devoted to such geometries. By electrostatic and steric arguments it is counterintuitive: all of the formally negatively charged ligands are crowded near each other. Lauher and Hoffmann,[12] based on their Extended Hückel study of Cp_2TiH^+, conclude that a non-planar geometry is expected for this species and all formally d^0 metal complexes. In their calculation, the LUMO for the Cp_2M^+ fragment is perpendicular to the plane defined by the Cp centroids and the metal. This LUMO is the orbital to which the R group would bond, thus giving the observed non-planar geometry. However, according to this analysis, bis(cyclopentadienyl)scandium complexes would also be expected to exhibit a non-planar geometry, in contrast to crystal structure data[4] and the results presented here. The implications of these geometries will be explored first, followed by an analysis of the causes of these geometries.

Implications

As previously discussed, the migratory insertion assumed in the Cossee-Arlman mechanism has been used by Ewen, *et al.*,[3] as the basis for their syndiospecific polymerization mechanism. Such geometries as found for Cl_2TiH^+ provide an electronic justification for this mechanism, as shall be described. With regards to their mechanism, a planar geometry, which is a loss of metal chirality, would represent a loss of

stereochemical information, for in their mechanism it is the chirality of the metal that dictates the stereochemistry of the insertion. Thus, according to their mechanism syndiospecific polymerization would *not* be expected for complexes that exhibit planar geometries, implying that scandium complexes, by nature of their electronics, could not be syndiodirecting.

Understanding the Geometries

The geometries listed in Table 1 can be understood in terms of the ground electronic structure of the metal.[13] Scandium has a $(4s)^2(3d)^1$ occupation, leading to a ^2D state, while Ti^+ has a $(4s)^1(3d)^2$ occupation, leading to a ^4F state. To minimize electronic repulsion between the two d electrons of Ti^+, one occupied d orbital lies in a plane (either the d_{xy} or $d_{x^2-y^2}$), while the other occupied d orbital is perpendicular to this plane (d_{z^2}). It is generally found[14] that electronegative ligands bond to other, less electronegative elements via the most easily ionized electrons of that element. In the case of transition metals, the most easily ionized electrons are the s. Thus, bonding two Cl's or Cp's to Sc uses the two metal electrons in 4s-like orbitals (as $4s+4p_z$ and $4s-4p_z$ hybrids), leaving a single electron in a d orbital for bonding to an H or alkyl. However, for titanium there is only one s electron and the Cl's or Cp's must bond via sd hybrids; again, the H or alkyl bonds to the remaining d electron. In this case, the M-X bonds use d_{xy}-s hybrids, while the M-R bond uses d_{z^2}. This bonding scheme is consistent with the calculations and leads naturally to the observed geometries for both Sc and Ti^+.

An analysis of the data presented in Table 1 shows that this interpretation is consistent with that data. For scandium, there is no directionality imposed upon the chlorines by their bonding to s electrons as the s orbitals are spherically symmetric. Again, the d electron to which the hydrogen is bound has little directionality imposed upon it; the orbital is a d_σ-type orbital, as the strongest covalent bonds are formed by using such orbitals, and has no orthogonality constraints. Because this covalent bonding scheme is so

flexible, electrostatics will dominate the geometry.† Formally, the three ligands are negatively charged; by Mulliken populations each chlorine carries a –0.37 charge and the hydrogen a –0.19 charge. Based on these charges, one would anticipate a planar geometry with angles of about 120°. A planar geometry is found, although the Cl-Sc-Cl angle is enlarged to 140° due to Cl-Cl repulsions Because little directionality is imposed by the covalent bonding, geometric deformations should require little energy. The energy increase required to move the H out of the plane by 50° is only 1.53 kcal/mol.

For the Ti^+ complex, the chlorines are bonding to s-d_{xy} hybrids. In such a bonding scheme, 90° Cl-Ti-Cl bond angles would be expected. The actual Cl-Ti-Cl angle is 120.5°. As in the Sc case, the Cl-Cl repulsions will enlarge this bond from 90°. It is significant that this angle is smaller than the Cl-Sc-Cl angle, which is dominated by electrostatic repulsions. The hydrogen position comes naturally from the Ti^+ d_{xy}–d_{z^2} occupation, as shown above. The energy for a planar structure is significant (12.8 kcal/mol), especially when compared to the Sc complex, indicating that there is a significant directionality imposed by the orbitals on the geometry.

These studies of isoelectronic Sc and Ti^+ complexes demonstrate that the electronic ground state of the metal or cation dictates the observed geometries. Metals often have low lying excited states that are important for directing structure and reactivity, as they are energetically accessible from the ground state (within 10-20 kcal/mol or 0.5-1.0 eV). Thus, it is important to determine the accessibility of the excited states of Sc and Ti^+. Table 2 shows the ground state and lowest lying important excited state for Sc, Ti^+, and Ti. From these data it can be seen that the excited states are inaccessible and thus the group state will determine the geometry.

---

†There will be some repulsive interactions between the d_σ orbital and the two sp hybrids used for bonding; even though the d_σ will be polarized towards the bonding region in the Sc-H bond, there will still be some orbital extent 180° from the Sc-H bond which would be repulsive with the two sp hybrids. However, this repulsive interaction is minor.

Table 2. Atomic State Splittings for Sc and Ti

Metal	Ground State	Excited State	Excitation Energy (eV)	
			Theory[a]	Experiment[b]
Sc	$^2D(s^2d^1)$	$^4F(s^1d^2)$	1.09	1.43
Ti^+	$^4F(s^1d^2)$	$^2D(s^2d^1)$	–4.26	–3.08
Ti	$^3F(s^2d^2)$	$^5F(s^1d^3)$	0.98	0.81

[a]Quartet state calculated at HF level, doublet state at GVB(1/2) PP level, correlating the s electrons
[b]Experimental data from ref. 15.

From Table 2, it is seen that Ti has an s^2 ground state. According to the arguments presented above, it is expected that Cl_2TiH would have a planar geometry, as it does (Table 1). Although the electronics of this complex are modified by the radical (open shell) electron, the geometry is still consistent with the above arguments.

One way to fully understand the bonding in a molecule, as it affects structure and reactivity, is to conceptually break the molecule into fragments. The fragments are studied to understand their orbital character and then the molecule is reassembled based on this bonding. Such a fragment analysis has been successfully employed in both Extended Hückel[16] and valence bonding[14,17] schemes. A complete analysis is presented, examining the diatomic and triatomic species in order to understand the bonding in the full complex. It is important to emphasize that such fragment analyses are meant to guide the reasoning, to understand the conditions for optimal bonds in the absence of other effects. It is not always obvious how competing effects will be compromised: the real test is the GVB wavefunction for the complete molecule.

MH and MCl Complexes

The metal hydride and chloride bonds are correlated in GVB(1/2) perfect-pairing (PP) wave-functions and are analyzed for the metal contribution to the bond, the character of the singly occupied orbitals, and the total metal valence occupations; this data is listed in Table 3. It is immediately obvious from this data how strongly the ground states of the

metal dictate the diatomic states. For scandium, the states that require a d^2 valence occupation, the $^3\Phi$ and $^3\Sigma$ states (based on the Sc valence occupations), are much higher in energy than those that can have a d^1 occupation, the $^3\Delta$ and $^3\Pi$, for both the hydride and the chloride complexes. For both the $^3\Pi$ and $^3\Delta$ states, Sc forms s-p_z hybrids, one which is used to bond to the ligand. Electron-repulsion considerations dictate which d orbital is occupied: for the ground state d_{xy} is occupied, leading to the $^3\Delta$ state. It can also be determined from this data that the optimal Sc hybridization for a M-L bond is about 40% s, 30% p, and 30% d. This hybridization has more sp character than has been previously found for optimal M-L covalent bonds, which is about 40% (sp) and 60% d.[18] A larger d contribution, though, would require mixing in more of the d^2 excited state.

In contrast to Sc, Ti^+ complexes are much more d^2 like and the singly occupied orbitals are almost pure d. Two states are important in the diatomics, $^3\Delta$ and $^3\Phi$ states. The $^3\Delta$ state is favored by the Ti^+ ground state with its $d_{x^2-y^2}$–d_{z^2} occupation. However, there is considerable repulsion in the $^3\Delta$ state between the M-L bond and the d_{z^2} orbital. In the Φ state this repulsion is minimized. In the hydride complex, the $^3\Phi$ state is the ground state, in agreement with previous studies.[19] However, the importance of the Ti^+ ground state can be seen in the low lying Δ excited state. In the chloride complex, the Δ is the ground state, with the Φ being only 0.27 kcal/mol higher in energy. The optimal bonding between Ti and ligands requires a 50% s, 20% p and 30% d hybridization.

Table 3. States for ScH, ScCl, TiH^+, and $TiCl^+$

				Character of Metal Bonding Orbital			Single Occupied Orbital			Metal Valence Occupations		
		ΔE										
Molecule	State	kcal/mol	Charge	%s	%p	%d	%s	%p	%d	s	p	d
ScH	$^3\Delta$	0.00	+0.22	40	30	30	68	27	5	0.99	0.50	1.29
	$^3\Pi$	6.77	+0.22	43	31	26	66	30	4	0.99	0.54	1.25
	$^3\Phi$	36.07	+0.23	63	22	15	0	0	100	0.48	0.23	2.06
	$^3\Sigma$	48.38	+0.24	61	21	18	0	0	100	0.46	0.15	2.14
ScCl	$^3\Delta$	0.00	+0.47	37	28	35	80	17	3	0.90	0.33	1.29
	$^3\Pi$	7.82	+0.49	39	30	31	81	18	1	0.91	0.36	1.24
	$^3\Phi$	36.75	+0.54	48	27	24	0	0	100	0.11	0.25	2.09
	$^3\Sigma$	47.21	+0.54	47	25	28	0	0	100	0.11	0.15	2.20
TiH^+	$^3\Phi$	0.00	+0.96	47	15	37	0	0	100	0.50	0.15	2.39
	$^3\Delta$	4.24	+1.00	65	15	20	9	0	91	0.76	0.15	2.09
	$^3\Sigma$	13.10	+0.95	38	15	47	0	0	100	0.41	0.14	2.51
	$^3\Pi$	28.03	+0.99	66	14	20	11	0	89	0.80	0.14	2.07
$TiCl^+$	$^3\Delta$	0.00	+1.22	53	22	25	5	1	94	0.29	0.22	2.28
	$^3\Phi$	0.27	+1.22	42	20	38	0	0	100	0.20	0.20	2.38
	$^3\Sigma$	12.54	+1.19	36	20	44	0	0	100	0.18	0.18	2.45
	$^3\Pi$	28.35	+1.23	56	21	23	6	1	93	0.33	0.28	2.22

Note: One of the singly occupied orbitals is a d orbital; thus, the character listed above for the singly occupied orbital is for the second orbital. Occupations and metal bonding character is based on Mulliken population analyses.

ClMH Complexes

Given the knowledge of the bonding for the MH and MCl complexes, one can predict how the subsequent ligands would bind and the resulting geometries. It is seen that for both ScH and ScCl that the two singly occupied orbitals on Sc are of s and d character respectively. It is also seen that the optimal bonds between Sc and H or Cl are of predominantly sp character. Thus, the second ligand would be expected to bond to the s electron, leading to a linear geometry. For Ti^+, the singly occupied orbitals are of d character. As with Sc, the ligands form the strongest bonds to orbitals of predominantly sp character. Thus, in order to form two strong bonds, the metal must either form sd hybrids, leading to 90° bond angles, or bond using the s^2 excited state, which would lead to 180° bonds like Sc.

At the GVB(1/2) level (correlating the M-H bond), the Cl-Sc-H angle is 180°, while the Cl-Ti-H angle is 100°. At this 180° bond angle, each ligand of ClScH bonds to the metal via metal sp hybrids (as usual for s^2 states) (Figure 2), leaving a singly occupied d orbital in the plane bisecting the Cl-Sc-H angle. Such a d occupation minimizes electron electron repulsions. At the GVB(2/4)-PP level of correlation (correlating both bonds), the Sc-H bond pair has 1.24 of the two electrons transferred to the H and has a scandium hybridization of 19% d and 81% sp; the Sc-Cl bond has 1.79 of the two electrons transferred to Cl, with 37% d and 63% sp on Sc. The unpaired orbital is d_{xy} (taking the molecular axis as z). The valence population on the Sc is 1.38 d and 0.89 sp.

In contrast, the Ti-H bond of $ClTiH^+$ involves a transfer of only 0.85 electrons to H and the Ti^+ hybridization is 79% d and 21% sp for a GVB(2/4) wave-function. The Ti-Cl bond involves 1.50 electrons transferred to Cl and has sd (55% sp and 45% d) metal hybrid character, with a valence Ti^+ population of 2.35 d and 0.62 sp. The singly occupied orbital has d_π-character relative to the Ti-Cl bond, and the Ti d contribution to the Ti-H and Ti-Cl bond is of d_σ character. $ClTiH^+$ is bent in order to maintain orthogonality between the metal d_σ orbitals used in the Ti-H and Ti-Cl bonds (Figure 3). Thus, the s^1d^2 state imparts an electronic influence on the geometry of the $ClTiH^+$ species due to the large metal d component of the metal ligand bonds

Figure 2. GVB Orbital for (a) ScH Bond and (b) ScCl Bond in ClScH

(a)

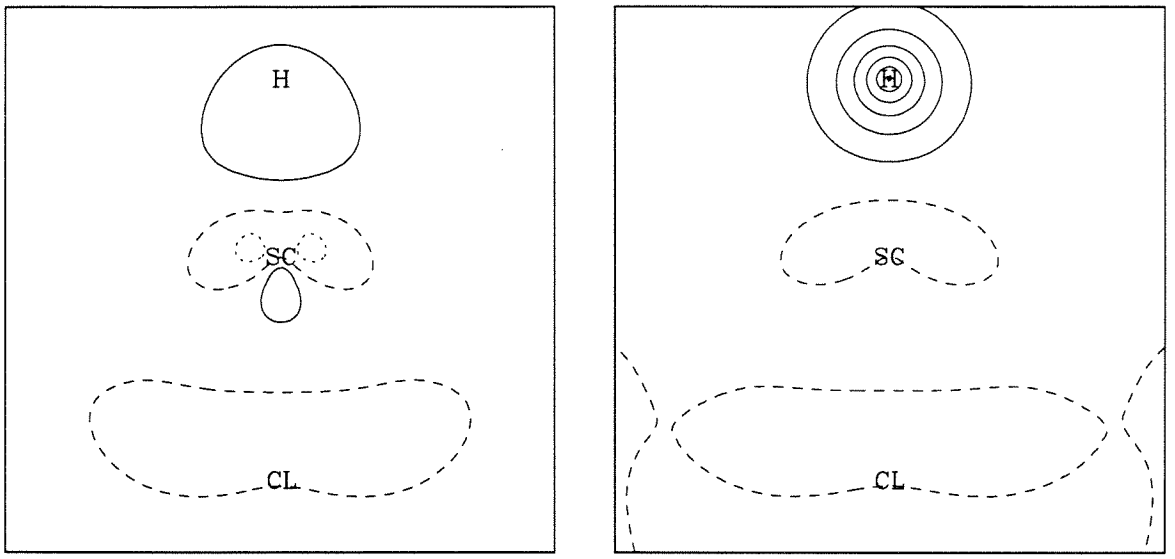

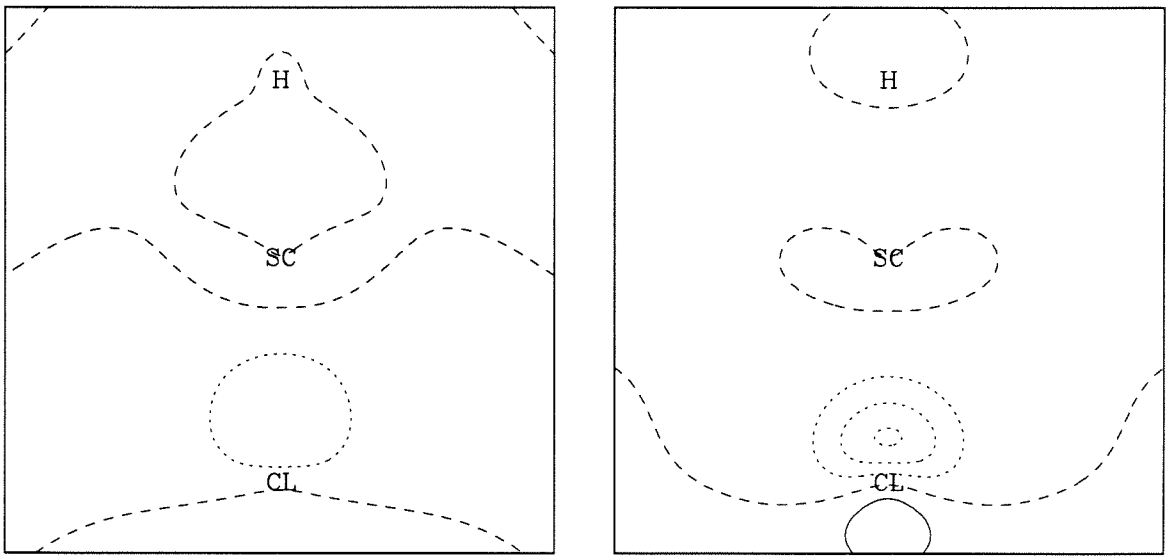

(b)

Figure 3. GVB Orbitals for (a) TiH Bond and (b) TiCl Bond in $ClTiH^+$

(a)

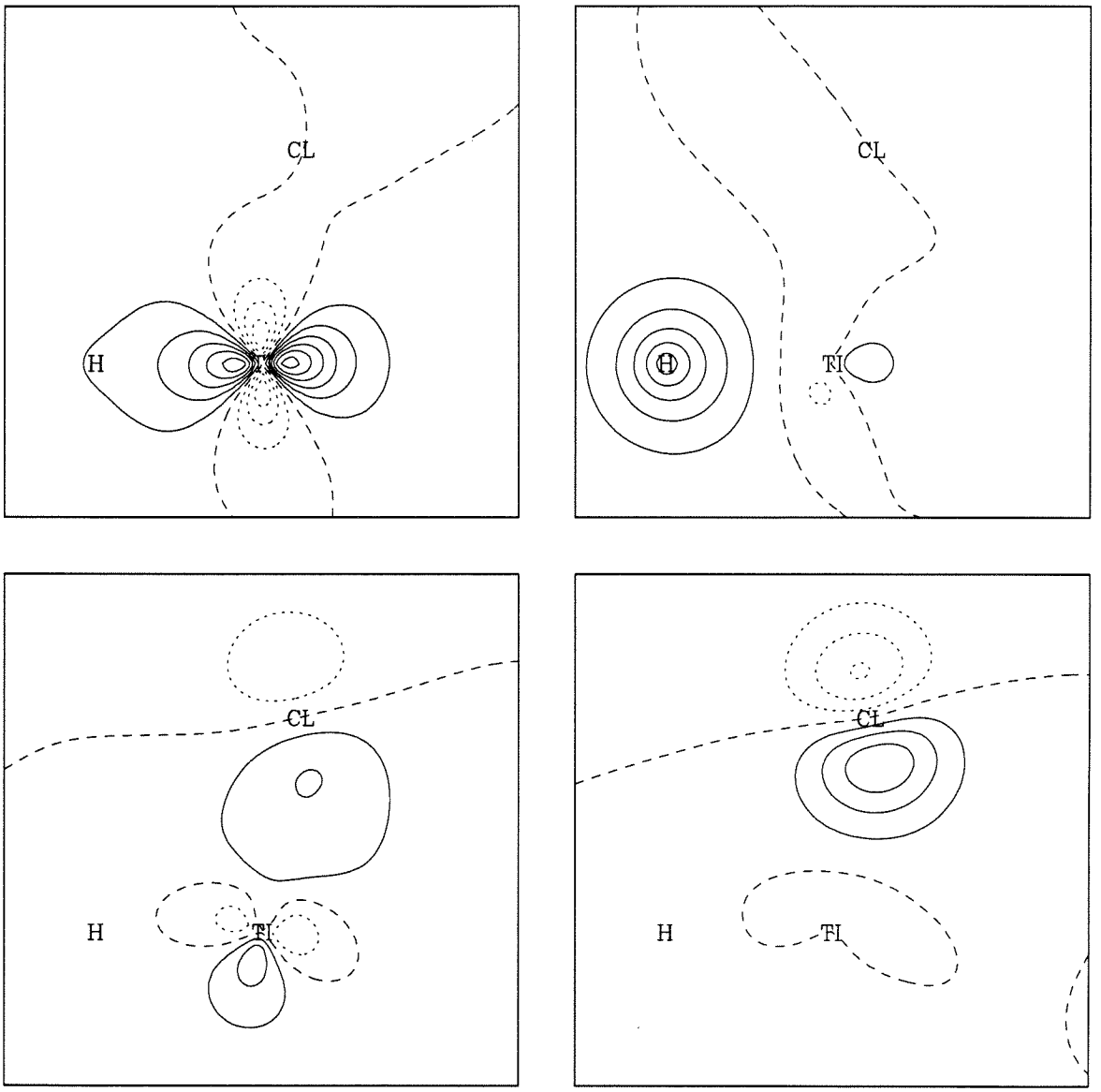

(b)

Cl_2Sc and Cl_2Ti^+ Complexes

Since Cl is more electronegative than the metal, there is some charge transfer from M to Cl. As stated earlier, this charge transfer is primarily out of the M s orbital, since this orbital is more easily ionized. Thus, the chlorines preferentially bond to the metal via metal s orbitals (or, polarized sp hybrids) rather than d orbitals. By polarizing the 4s pair with 4p

orbitals, scandium can form two bonds that are of predominantly metal-s character, leaving a singly occupied d orbital that prefers to be in the plane bisecting the Cl-Sc-Cl angle (Figure 4). The two Cl-Sc bonds have a 180° angle between them due to hybridization and minimization of the electrostatic repulsion between the chlorines. Indeed, the Cl-Sc-Cl angle of $ScCl_2$• is 180°. However, the energy to bond at an angle of 126° is only 5.69 kcal/mol higher.

The titanium case is much different. Ti^+ has only one valence s electron, so that the two Ti-Cl bonds must incorporate some d character. If the s and d orbitals had the same radial character, then mixing the 4s and $3d_{xy}$ would lead to 90° bonds.[‡] It is found that the $TiCl_2$•$^+$ fragment has an optimum angle of 126°, with an energy 7.24 kcal/mol below that of the linear geometry. In addition to the radial mismatch, this increase from 90° is due to Cl-Cl electrostatic repulsions, causing the metal to mix in some $d^3(^4F)$ character (which is only 2.78 kcal/mol higher in energy than the s^1d^2 state).[15] At the optimum angle of 126°, the remaining singly occupied orbital has a pure d character and lies in the symmetry plane bisecting the ClTiCl angle (Figure 4).

[‡]For the first row of the transition metal series, the radial mismatch between the s and d orbtials is quite large, especially compared to the other rows of the transition metal series. The computed ratio $\sqrt{\langle r_d^2\rangle / \langle r_s^2\rangle}$ for the s^1d^2 state is 0.56 for Sc, 0.46 for Ti^+, 0.67 for Y, 0.61 for Zr^+, 0.68 for La, 0.71 for Hf^+, and 0.77 for Th^+.

Figure 4. Singly Occupied Orbitals, (a) $ScCl_2$ and (b) $TiCl_2^+$

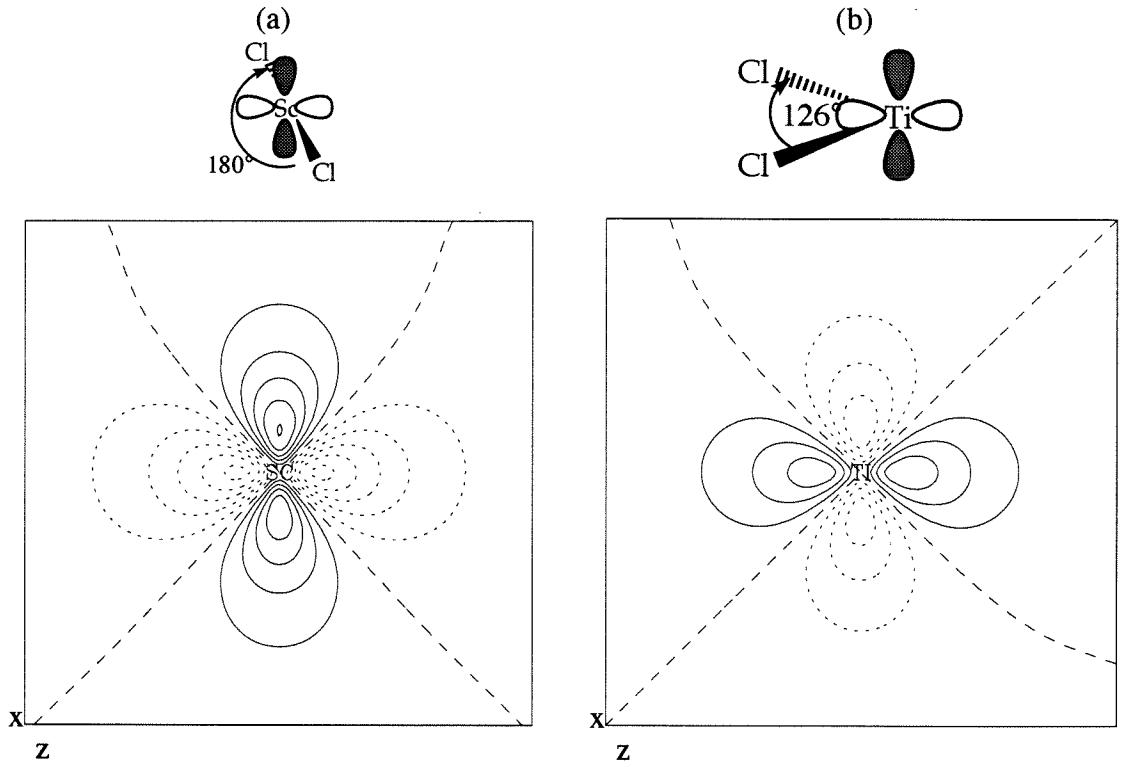

Cl_2MH Complexes

The optimum geometry for Cl_2ScH (Table 1) leads to a ClScCl angle that decreases from 180° to 140° as the H bonds to the d_{z^2} orbital in the ClScCl plane, leading to a planar molecule. On the other hand, with Cl_2TiH^+ the H bonds to the x^2 lobe of the $d_{z^2-x^2}$ orbital, leading to an angle of 84° while the ClTiCl angle decreases slightly from 126° to 120°, reflecting increased d character in the TiCl bonds accompanying the incorporation of s character into the MH bond (the M-H bonds are shown in . Thus, the geometries are explained by the difference in atomic character for Sc and Ti^+.

Figure 5. M-H Bonds in Cl_2MH (GVB-Pair) (a) Cl_2ScH and (b) Cl_2TiH^+

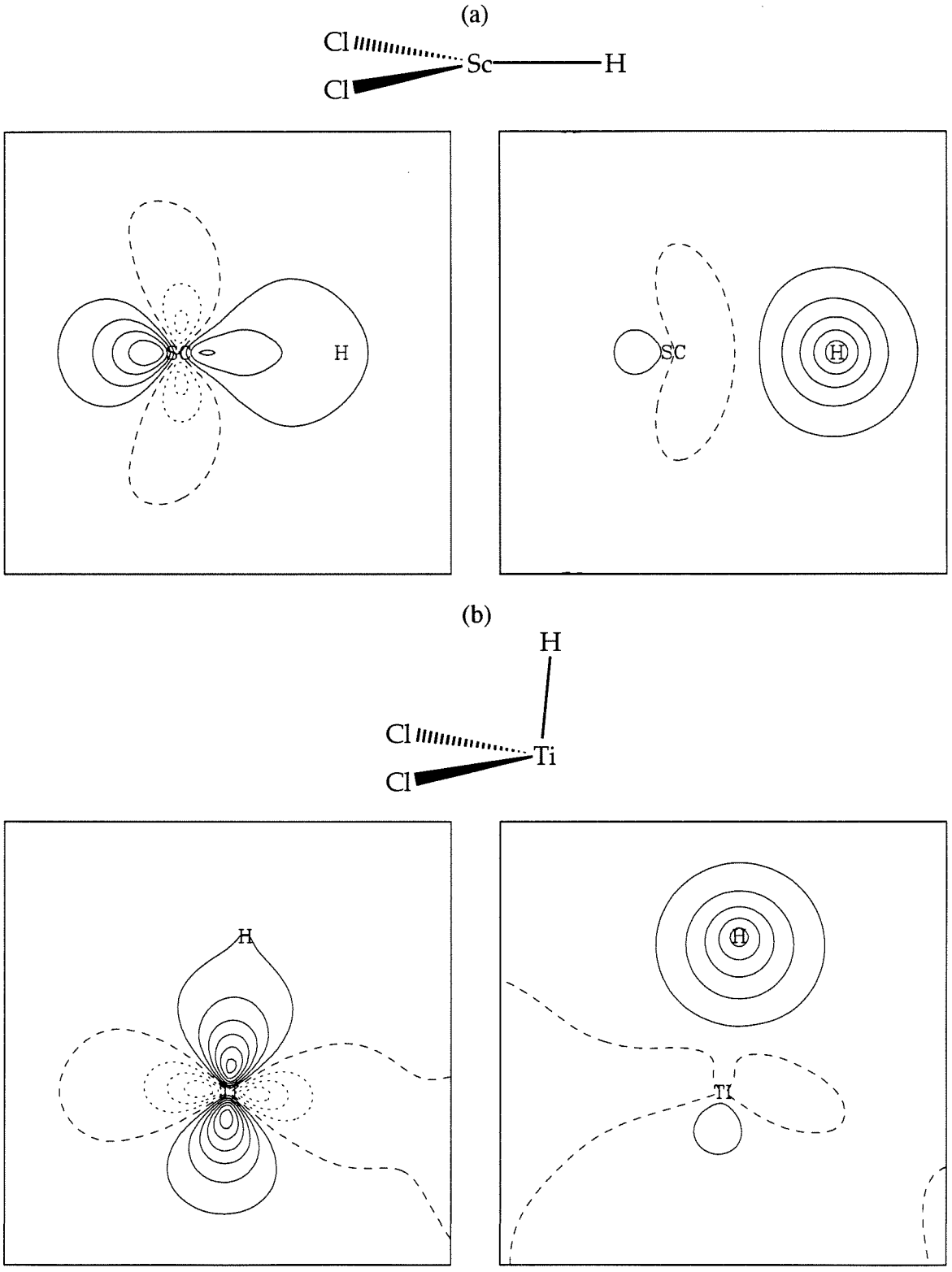

The neutral $Cl_2TiH\bullet$ was also studied. Since Ti has an s^2d^2 (^3F) ground state, the above arguments suggest that the *neutral* group 4 compounds would be planar. It is expected that the metal character of the Ti-Cl bonds is primarily of s character (like the group three cases) and the TiH bond to have no directionality imposed upon it. Indeed, as shown in Table 1, the geometry of this complex is planar.

As in the previous sections, the bonds of these three systems are correlated in GVB(3/6) wave-functions and the metal character is analyzed; the results are listed in Table 4. The metal character of the bonds for the Sc, Ti^+, and Ti systems differ significantly. In the cases of Sc and Ti, the metal sp contribution to both M-H and M-Cl bonds is much larger than for Ti^+.

It is seen that the metal ground state dictates the geometries for all Cl_2ScH, Cl_2TiH, and Cl_2TiH^+ and all of their fragments. The s^1d^2 metal ground state is a necessary condition for geometries that are compatible with the Ewen, *et al.*[3] syndiodirecting mechanism. The remaining group three[10] and four[8,9] metallocenes are known to polymerize α-olefins and complexes containing Zr and Hf have produced syndiotactic polymers.[9] To test the validity of the electronic model developed above, the remaining group three and four metallocene systems are studied using the same simple models.

Table 4. Metal Character of Metal-Ligand Bonds in Cl-M-H species

	Total Charge			MCl Bond				MH bond			
Species	M	Cl	H	M Occ.[a]	%s	%p	%d	M Occ.[a]	%s	%p	%d
ScH	+0.22	—	–0.22	—	—	—	—	0.81	40	37	30
ScCl	+0.47	–0.47	—	0.29	37	28	35	—	—	—	—
$ScCl_2$	+0.86	–0.43	—	0.28	32	30	38	—	—	—	—
ClScH	+0.73	–0.48	–0.24	0.21	25	38		0.75	43	37	20
Cl_2ScH	+0.87	–0.37	–0.13	0.33	24	33	44	0.93	19	18	63
TiH^+	+0.96	—	+0.04	—	—	—	—	1.05	47	15	37
$TiCl^+$	+1.22	–0.22	—	0.47	53	22	25	—	—	—	—
$TiCl_2^+$	+1.12	–0.06	—	0.65	19	20	61	—	—	—	—
$ClTiH^+$	+1.03	–0.14	+0.11	0.49	32	32	46	1.15	13	8	79
Cl_2TiH^+	+0.78	+0.01	+0.21	0.64	20	17	63	1.21	11	5	84
Cl_2TiH•	+0.70	–0.32	–0.06	0.34	2	35	39	1.00	16	12	72

Data based on Mulliken population analyses.
[a]The total number of electrons associated with the metal within a two-electron bond pair

Studies of Cl_2MH Species for M= Y, Zr^+, La, Hf^+

The atomic ground states for the four metals are listed in Table 5. Only the group four cations have the correct electronic structure to exhibit a non-planar geometry. Indeed, according to these data, Cl_2HfH^+ is expected to have a planar geometry. The group three and group four neutral complexes are all expected to have a planar geometry. It is found that Cl_2YH, Cl_2LaH, Cl_2ZrH, and Cl_2HfH all exhibit planar geometries while Cl_2ZrH^+ and Cl_2HfH^+ are non-planar (see Table 9). As will be discussed, hafnium is a special case, for which the ground state does not exclusively dictate the bonding.

Table 5. Atomic State Splittings for Y, Zr, La, and Hf

			Excitation Energy (eV)	
Metal	Ground State	Excited State	Theory[a]	Experiment[b]
Y	$^2D(s^2d^1)$	$^4F(s^1d^2)$	0.88	1.36
Zr+	$^4F(s^1d^2)$	$^2D(s^2d^1)$	2.08	1.71
La	$^2D(s^2d^1)$	$^4F(s^1d^2)$	0.34	0.36
Hf+	$^2D(s^2d^1)$	$^4F(s^1d^2)$	0.52	0.56

[a]Quartet state calculated at HF level, doublet state at GVB(1/2) PP level, correlating the s electrons
[b]Experimental data from ref. 15.

MH and MCl Complexes

The ground state of the metal is an effective guide for the bonding of the fully ligated complex, although it breaks down for hafnium. Hafnium and lanthanum present somewhat of a special case as the state splittings for these two metals are much smaller than in all other metals. Correspondingly, there is a much greater opportunity for excited states to mix with the ground state and direct the bonding. To study how this mixing affects the bonding, it is necessary to analyze the metal-ligand bonds. Thus, studies of MH and MCl assist in understanding the important interactions and states for these complexes.

In Table 6 the metal hydride and metal chloride bonds are correlated using GVB(1/2)-PP wave-functions, as was done for the Sc and Ti^+ systems. Previous computational studies[20] of ZrH^+ find that the $^3\Phi$ state is lower than the $^3\Delta$ state by 1.5 kcal/mol. This discrepancy is most likely due to the difference in metal basis sets: the previous study used a basis optimized for neutral Zr, while the current study used a basis recontracted for Zr^+. The important difference between these bases is the size of the 4s orbital is larger for the cation, allowing greater s-d mixing. Indeed, it is found in the current study that by forming $s+d_\sigma$ and $s-d_\sigma$ hybrids, the $^3\Delta$ state can readily reduce electron repulsion and form strong covalent bonds. In agreement with previous computational studies[21] of HfH^+, the current study finds the $^3\Delta$ state to be the ground state.

One important trend from Table 6 is the increase in metal d character in both the HfH^+ (31% d) and $HfCl^+$ (21% d) bonds, relative to the La (14% and 6% d) and Y (9% and 5% d) compounds. As has been stated earlier, optimal metal covalent bonds are formed when the metal character is about 60% d and 40% sp. This character can only be achieved when there is efficient mixing between the s and d orbitals. Such efficient mixing is controlled by two factors: the energy match and the size match[22] between the two sets of

orbitals. For Sc, Ti^+, Y, and Zr^+, the energy match, as measured by the s^2d^1-s^1d^2 splitting, reducing the effectiveness of the mixing.

The energy match is much better for La and Hf^+, so that one would expect a more efficient mixing between the s and d orbitals as manifested by a larger metal d contribution in covalent bonds. However, the size match between these two is also important for the mixing efficiency, as was found when comparing Co, Rh and Ir complexes;[23] the s and d orbitals are more similar in size for Hf^+ than for La (see note, page 43). An important difference between La and Hf is that Hf exhibits much stronger relativistic effects than La due to its lanthanide core. These effects include stabilization of the s and p electrons, with a subsequent contraction of the s and p orbitals, and a destabilization of the d electrons, with a subsequent enlargement of the d orbitals. These effects are manifested in the s^2d^1 ground state (an s^1d^2 ground state is expected by comparison with Zr^+ and Ti^+). The effects are also manifested in an ionic radius for Hf^+ (0.85 Å) that is very similar to that of Zr^+ (0.86 Å).[24] Thus, the mixing efficiency for Hf is greater than for La, allowing optimal M-L bonds to form. Forming these bonds requires the incorporation of the s^1d^2 state. Thus, although the Hf^+ ground state is s^2d^1, bonding ligands to the metal will favor the metal s^1d^2 state.

Table 6. States for MH and MCl, M=Y, Zr^+, La, and Hf^+

				Character of Metal Bonding Orbital			Single Occupied Orbital			Metal Valence Occupations		
Molecule	State	ΔE kcal/mol	Metal Charge	%s	%p	%d	%s	%p	%d	s	p	d
YH	$^3\Delta$	0.00	+0.40	34	21	45	71	20	9	0.92	0.33	1.36
	$^3\Pi$	5.59	+0.38	34	24	42	68	32	0	0.89	0.49	1.24
	$^3\Phi$	37.00	+0.35	51	19	30	0	0	100	0.33	0.41	1.90
	$^3\Sigma$	41.74	+0.30	57	21	22	0	0	100	0.40	0.35	1.96
YCl	$^3\Delta$	0.00	+0.51	27	20	52	82	13	5	0.89	0.26	1.35
	$^3\Pi$	7.86	+0.51	28	19	49	83	17	0	0.89	0.40	1.20
	$^3\Phi$	38.70	+0.53	35	22	44	0	0	100	0.08	0.41	1.97
	$^3\Sigma$	46.33	+0.54	38	25	38	0	0	100	0.09	0.46	1.91
ZrH^+	$^3\Delta$	0.00	+1.11	33	10	56	54	0	46	0.85	0.07	1.98
	$^3\Phi$	5.09	+1.09	38	13	50	0	0	100	0.35	0.10	2.46
	$^3\Sigma$	13.90	+1.07	45	13	42	0	0	100	0.42	0.12	2.39
	$^3\Pi$	16.70	+1.08	31	11	58	61	1.3	38	0.89	0.10	1.93
$ZrCl^+$	$^3\Delta$	0.00	+1.25	36	11	52	38	0	62	0.52	0.12	2.10
	$^3\Phi$	5.10	+1.31	34	15	51	0	0	100	0.15	0.15	2.40
	$^3\Sigma$	17.30	+1.34	39	16	45	0	0	100	0.16	0.19	2.31
	$^3\Pi$	22.10	+1.25	34	12	54	52	2	46	0.66	0.15	1.94
LaH	$^3\Delta$	0.00	+0.44	28	13	60	74	12	14	0.90	0.18	1.48
	$^3\Pi$	5.50	+0.44	27	16	57	70	30	0	0.86	0.43	1.27
	$^3\Phi$	29.90	+0.40	43	14	43	0	0	100	0.26	0.29	2.09
	$^3\Sigma$	35.70	0.353	47	18	35	0	0	100	0.30	0.30	2.04
LaCl	$^3\Delta$	0.00	+0.553	22	14	63	84	10	6	0.89	0.18	1.38
	$^3\Pi$	8.25	+0.55	22	19	67	84	16	0	0.88	0.41	1.15
	$^3\Phi$	30.90	+0.58	28	15	57	0	0	100	0.06	0.36	2.00
	$^3\Sigma$	40.20	+0.59	30	19	51	0	0	100	0.06	0.44	1.90
HfH^+	$^3\Delta$	0.00	+1.18	41	13	47	63	7	31	0.96	0.15	1.71
	$^3\Phi$	12.88	+1.16	42	14	40	62	13	2	0.97	0.24	1.63
	$^3\Sigma$	37.20	+1.10	63	11	26	0	0	100	0.57	0.11	2.22
	$^3\Pi$	42.90	+1.06	70	11	18	61	1.3	38	0.66	0.12	2.15
$HfCl^+$	$^3\Delta$	0.00	+1.24	36	14	50	75	4	21	0.91	0.17	1.69
	$^3\Pi$	15.70	+1.26	37	17	46	80	12	8	0.93	0.28	1.53
	$^3\Phi$	42.20	+1.30	48	14	38	0	0	100	0.20	0.20	2.29
	$^3\Sigma$	54.0	+1.31	54	16	30	0	0	100	0.24	0.26	2.19

Note: One of the singly occupied orbitals is a d orbital; thus, the character listed above for the singly occupied orbital is for the second orbital. Occupations and metal bonding character based on Mulliken population analyses.

MHCl

In contrast to the results for Sc and Ti^+, all the MHCl species for the remaining group three and four metals are bent (see Table 7). The main reason for this difference is the competition between (1) the accessibility of the correct states for bonding, (2) the efficiency of mixing between the s and d orbitals and (3) the correct metal hybridization for optimal metal-ligand bonds. In the first row the s-d mixing is very inefficient. In the case of scandium the s^1d^2 and s^2d^1 states are well separated in energy; in addition the radial mismatch is quite large, leading to little mixing between the s and d orbitals. In the second and third rows the s and d orbitals can mix more effectively, allowing bonds to both ligands which incorporate more d character, leading to bent geometries. Zr^+ builds in more d character into the bonds than does Y (Table 8), consequently, the $ClZrH^+$ angle is smaller than the ClYH angle.

Table 7. Geometries of ClMH, M=Y, Zr^+, La, Hf^+

Species	R(M-H)	R(M-Cl)	θ(Cl-M-H)
ClYH	1.96	2.54	124.2
$ClZrH^+$	1.82	2.38	111.8
ClLaH	2.14	2.73	117.7
$ClHfH^+$	1.80	2.34	109.8

Distances in Å, angles in degrees, geometries optimized for HF wave-function

However, it is noted La builds more metal d character into the bonds than does Hf^+. While La appears to exhibit a greater electronic preference for the s^1d^2 state, as manifested by a large metal d contribution to the bonds, it must be kept in mind the role that electrostatics play. In the case of La, the bonds are strongly polarized towards the ligands (away from La), as manifested by the metal occupation of each bond (Table 8), resulting in a La charge of nearly +1.0. In such a case, the bonding of La is more like Cl^- LaH^+ (with some $ClLa^+$ H^- character also), which would reduce the effect of the covalent-directed geometry. In the Hf^+ complex, the metal has been further ionized by only 0.20 electrons,

leading to much less polarized (more covalent) bonds, which would lead to a greater observed geometric effect for Hf^+ than for La.

Table 8. Metal character in ML bonds, ClMH, M=Y, Zr^+, La, Hf^+

	Total Charge			MCl Bond				MH bond			
Species	M	Cl	H	M Occ.[a]	%s	%p	%d	M Occ.[a]	%s	%p	%d
ClYH	+0.77	–0.47	–0.31	0.27	18	25	58	0.73	27	22	51
$ClZrH^+$	+1.19	–0.23	+0.05	0.45	27	13	62	1.07	25	13	62
ClLaH	+0.92	–0.54	–0.39	0.24	17	18	65	0.65	24	15	61
$ClHfH^+$	+1.20	–0.21	0.00	0.45	29	16	55	1.05	35	16	49

Data based on Mulliken population analysis of GVB(2/4) PP wave-functions
[a]The total number of electrons associated with the metal within a two-electron bond pair

Analysis of Cl_2MH, M = Y, Zr^+, La, and Hf^+

The geometries for the Y, Zr^+, La, and Hf^+ species are given in Table 9. Given the results from both the diatomic and triatomic species, one would anticipate planar geometries for Cl_2YH and Cl_2LaH and non-planar geometries for Cl_2ZrH^+. From the results of HfH^+, $HfCl^+$, and $ClHfH^+$, it is anticipated that hafnium's chemistry is directed largely by the s^1d^2 state, giving a non-planar geometry. However, the geometry and energetics should be tempered by the fact that the s^2d^1 state contributes strongly to the bonding. The angle between the plane and the M-H bond is nearly the same for Hf^+ (65.0°) and Zr^+ (68.0°), but the Hf^+ barrier height for the inversion (energy required for a planar geometry) is about half that of Zr^+.

Table 9. Geometries of Cl_2MH Complexes, M= Y, Zr^+, La, Hf^+

Metal	R(M-H)	R(M-Cl)	θ(Cl-M-Cl)	θ(Plane-H)	Barrier Height[a]
Y	1.966	2.533	116.9	0.0	0.0
Zr^+	1.801	2.350	115.8	68.0	9.619
La	2.157	2.732	116.3	0.0	0.0
Hf^+	1.795	2.335	121.5	65.0	4.27

Distances in Å, angles in degrees, geometries optimized at GVB(1/2) PP wave-function, correlating the M-H bond
[a]Energies in kcal/mol, based on GVB(1/2)*SD + Q wave-functions.

The values for the angle (84.4°) and barrier height (12.8 kcal/mol) are greater for Cl_2TiH^+ than for both Cl_2ZrH^+ and Cl_2HfH^+ due to the greater separation between the s^1d^2 and s^2d^1 states in energy (4.26 vs. 2.08 and –0.52 eV) for Ti^+ and because the mixing between the s and d orbitals is so inefficient, leading to a TiH bond that is over 80% d. As can be seen for the corresponding ZrH and HfH bonds, much more s character is mixed into these bonds (Table 10).

Table 10. Metal Character of Metal-Ligand Bonds in Cl_2MH Species, M=Y, Zr^+, La, and Hf^+

	Total Charge			MCl Bond				MH bond			
Species	M	Cl	H	M Occ.[a]	%s	%p	%d	M Occ.[a]	%s	%p	%d
Cl_2YH	+1.23	–0.45	–0.33	0.245	14	28	59	0.695	26	22	52
Cl_2ZrH^+	+1.28	–0.16	+0.04	0.498	23	13	64	1.049	20	10	70
Cl_2LaH	+1.384	–0.52	–0.35	0.224	15	21	64	0.666	28	6	66
Cl_2HfH^+	+1.42	–0.18	–0.05	0.418	23	18	59	0.977	31	17	52

Data based on Mulliken population analysis of GVB(3/6) PP wave-functions
[a]The total number of electrons associated with the metal within a two-electron bond pair

Investigating Thorium For Use in Syndiodirecting Catalysts

Thorocene complexes are known to be effective olefin polymerization catalysts.[25] Previous computational studies of thorium[6] indicate that its chemistry is qualitatively similar to that of Zr and Hf. Thus, studies were performed on Th^+ to determine if it has the correct electronic structure to form effective syndiodirecting catalysts.

One problem with thorium in particular, and with all other heavy metals in general, is that relativistic effects have a large influence on electronic structure. In particular, the orbitals with the greatest core penetration are stabilized: thus the s, and to some extent the p, orbitals are stabilized, and the d orbitals are destabilized. Another problem with describing the electronic structure of heavy metals is that spin-orbit effects are large. A manifestation of this problem occurs in the assignments of the atomic excitation spectrum for thorium.

A thorough discussion of this problem may be found elsewhere;[6] there is extensive mixing between the ^4F (s^1d^2) states and ^2D (s^2d^1) for Th^+. The ground state has been assigned by Minsky[26] to be 43% ^4F and 27% ^2D, with no dominant component. Because the leading component of the ground state is ^4F, it would be expected to exhibit chemistry similar to the other group 4 cationic compounds. However, because ^2D configuration mixes in so strongly in the ground state, the 7s and 6d orbitals are quite close in energy, as in the case of hafnium.

Using theoretical methods, Brusich[6] found that at the HF level, the ^4F state was favored by 0.86 eV over the ^2D state; however, at the fully correlated level, he found that the ^2D was 0.29 eV lower in energy than the ^4F state. The HF state will be more relevant to the current calculations, especially the geometric calculations (as these are performed at the HF level), but both calculations suggest the s and d orbitals are quite close in energy. By the arguments used above to understand the geometries for Hf complexes, it is anticipated that Th^+ complexes would exhibit non-planar geometries.

Cl_2ThH^+ does indeed exhibit the anticipated geometry (Table 11). It is interesting that with an inversion barrier of 5.60 kcal/mol, Cl_2ThH^+ favors a non-planar geometry to a greater extent than Cl_2HfH^+ (which has an inversion barrier of only 4.27 kcal/mol), but less than Cl_2ZrH^+. In addition, the angle that the M-H bond makes with the Cl_2M plane is slightly larger for the thorium complex than for either the zirconium or hafnium complexes. Thus, based solely on these simple considerations, thorocene catalysts are expected to show a syndiodirecting capability midway between that of zirconium and hafnium. For comparison purposes, the non-adiabatic potential energy surfaces for varying only the inversion mode are plotted in Figure 6. It is seen that this out-of-plane motion is endothermic for the group three complexes, while it is exothermic for the group four cationic complexes.

Table 11. Geometry of Cl_2ThH^+

Metal	R(M-H)	R(M-Cl)	θ(Cl-M-Cl)	θ(Plane-H)	Barrier Height[a]
Th+	2.098	2.662	110.4	71.0	5.60

Distances in Å, angles in degrees for optimized geometries for GVB(1/2) PP wave-function, correlating M-H bond.

[a]Energy in kcal/mol for GVB(1/2)*SD + Q wave-function

Figure 6. Energy of Inversion Mode, Cl_2MH complexes for GVB(1/2)*SD + Q wave-function

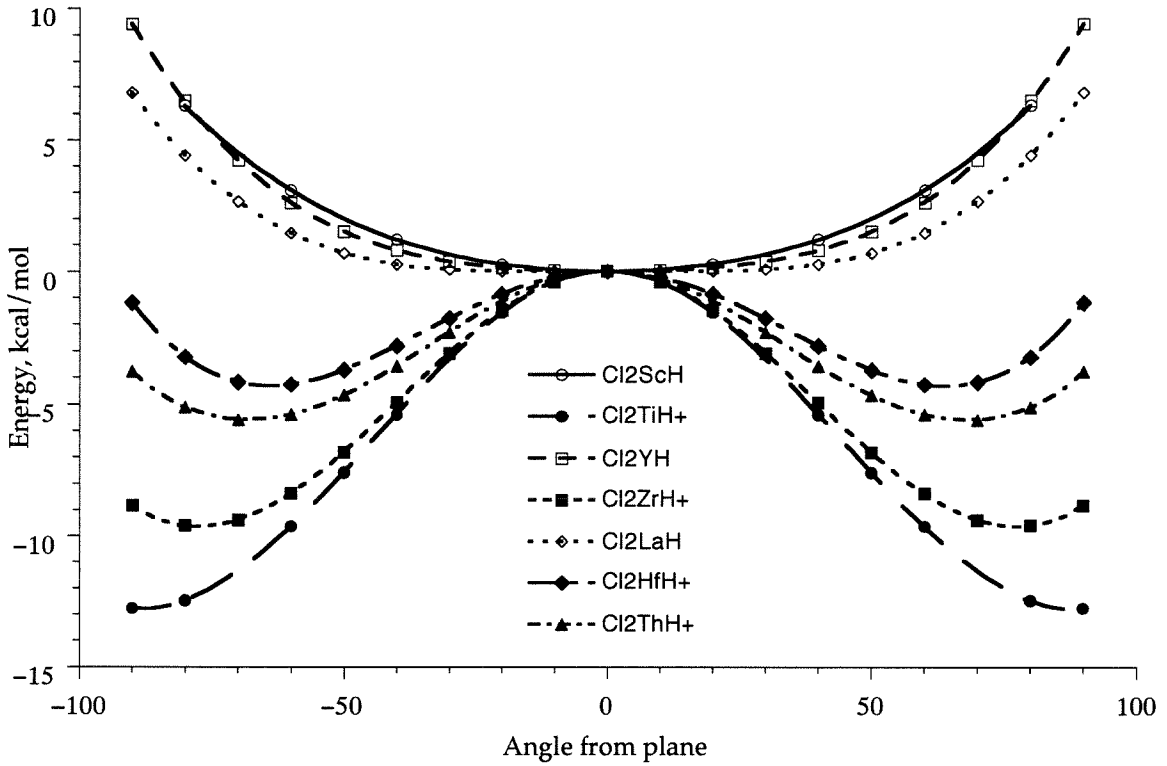

The models have considered only the electronic effects of the metal ground state on the geometries. While much insight has been gained from these model complexes, the inclusion of steric effects is necessary to fully understand these systems. In addition, while hydrogen is a reasonable electronic model for a covalently bond ligand and chlorine a reasonable model for an ionically bound ligand, it is still important to understand the bonding characteristics between sp^3 carbon and a metal and Cp and a metal. Thus, the metallocene alkyl complexes will be slowly built up, to see how ligand differences modify the understanding.

Studies of Dichlorometal Methyl Complexes

The first step towards building the full alkylated metallocene catalyst is correctly describing the M-C bond by studying $Cl_2M(CH_3)$. As shown in Table 12, Ti^+, Zr^+, Hf^+, and Th^+ complexes are all non-planar, whereas the Sc, Y, and La complexes are all planar. Geometries similar to the dichloro-metal-hydride geometries are expected for these systems. This expectation is borne out in the data. The largest differences between the hydride and the methyl systems for the bonding between the metal and chlorides: in the Y and La complexes, these bonds lengthen and the Cl-M-Cl angle increases, indicating that the M-Cl bond has a greater metal s orbital contribution; in a similar manner the ZrCl and HfCl bonds shorten, indicating stronger M-Cl bonding.

Table 12. Geometries of $Cl_2M(CH_3)$, M=Sc, Ti^+, Y, Zr^+, La, Hf^+, Th^+

Metal		R(M-Cl)	R(C-H)	θ(ClMCl)	θ(MCH)	θ(Plane-Me)	Barrier Height[a]
Sc	2.15	2.40	1.09	141.9	109.0	0	0
Ti^+	1.99	2.20	1.09	115.5	98.0	64.5	9.55
Y	2.33	2.546	1.092	130.0	112.0	0	0
Zr^+	2.357	2.149	1.090	114.9	110.2	63.1	8.87
La	2.529	2.749	1.094	131.5	112.0	0	0
Hf^+	2.150	2.344	1.090	118.3	111.0	63.3	5.53
Th^+	2.464	2.677	1.090	112.0	112.0	65.8	6.84

Distances in Å, angles in degrees for geometries optimized using HF wave-functions.
[a]Energy in kcal/mol for GVB(1/2)*SD + Q wave-function (except Th^+, which was computed using a MCPF wavefunction

The non-planar bias of $Cl_2Ti(CH_3)^+$ (64.5°, 9.55 kcal/mol barrier) is less pronounced than for Cl_2TiH^+ (84.4°, 12.8 kcal/mol barrier). The origin of this difference is probably electrostatic. The carbon carries a negative charge, leading to a repulsion between the chlorines and the methyl, whereas the hydrogen carries a positive charge, leading to an attraction. To test this idea, the methyl group was replaced by a silyl group (Table 13). The silicon has a positive charge and should be more similar to H. Indeed, a non-planar geometry with a 89.7° angle is found. Again, the corresponding Sc complex is found to be planar. It is also interesting to note that the Ti-Si bond is lengthened relative to the Sc-Si

bond; in all other cases, the Ti-R bond is shorter. This lengthening is probably partly due to the positive charge that resides on SiH_3 group and partly due to a weaker TiSi bond. The calculated inversion barrier is about 2 kcal/mol less than for the $Cl_2Ti(CH_3)^+$ even though the inversion angle is larger, indicating that the TiSi bond is weaker: the covalent geometric effect is not as strong. The Cl-Ti-Cl angle in $Cl_2Ti(SiH_3)^+$ is enlarged to the same value as the angle in Cl_2Ti^+, again due to the cationic nature of the SiH_3 group.

Table 13. Geometries of $Cl_2M(SiH_3)$, M=Sc, Ti^+

Metal	R(M-Si)	R(M-Cl)	θ(ClMCl)	θ(Plane-Si)	Barrier[a]
Sc	2.79	2.39	131.0	0.0	0.0
Ti^+	2.89	2.23	126.3	89.7	7.58

Distances in Å, angles in degrees for optimized geometries for a GVB(1/2) wave-function, correlating the M-Si bond

[a]Energies in kcal/mol for GVB(1/2)*SD + Q wave-functions

The metal ground state configuration has been shown to be an effective guide for understanding the ground state geometries of the model Ziegler-Natta catalysts, with the exception of Hf^+; in this case the metal d contributions are large enough so that the s^1d^2 state, which is only 0.56 kcal/mol higher than the ground state, controls the geometries observed. Through this electronic structure guide, one is led to two conclusions: first, group three complexes are not expected to exhibit syndiodirecting capabilities, and, second, thorium is a metal deserving attention for new syndiodirecting catalysts.

Studies of Metallocene Species

It is impractical to fully optimize the geometries of all these species. Reasonable geometries were assumed for the metallocene, based on crystal structure data this assumption is discussed more fully in the appendix of this chapter. In all cases, the metal-R distance was optimized (in the case of methyl, keeping a fixed CH_3 geometry) with an inversion angle of 0°. Using this metal-R distance, the optimum inversion angle was determined.

As there have been no reported crystal structures of titanocene-based syndiodirecting homogeneous catalyst systems, the geometry for the Cp_2Ti fragment was taken from crystal structure data of titanocene complexes[27] giving an average CpTiCp angle of 132.6°. Crystal structure data have been published for syndiodirecting catalyst precursors for both Zr (CpZrCp angle of 118°) and Hf (CpHfCp angle of 119.4°).

The results for the hydride complexes are listed in Table 14. Previously, it had been found that titanium complexes demonstrated a greater bias for non-planar geometries. However, based on the data in Table 14, it appears that this bias decreases for the metallocene complexes, as the inversion angle and inversion barriers have decreased for Cp_2TiH^+ relative to Cp_2ZrH^+. As shall be seen in the analysis of the metallocene methyl complexes, this decrease in bias is due to the large Cp-Ti-Cp angle used for the calculations. The potential energy surfaces for the inversion modes for these systems are plotted in Figure 7.

Table 14. Geometries of Cp_2MH Species

Metal	R(M-Cp)	θ(Cp-M-Cp)	R(M-H)	θ (Plane-H)	Inversion Barrier[a]
Sc	2.17	143.0	1.82	0.0	0.0
Ti^+	2.07	132.6	1.73	65.0	5.2
Y	2.388	118.0	2.03	0.0	0.0
Zr^+	2.19	118.0	1.91	70.0	4.22
La	2.531	118.0	2.254	0.0	0.0
Hf^+	2.20	119.4	1.88	50.0	0.50
Th^+	2.53	118.0	2.148	70.0	6.17

Distances in Å, angles in degrees

[a]Energies in kcal/mol, for GVB(1/2)*CpCI + Q wave-functions

Figure 7. Energy Surfaces for the Hydrogen Inversion in Cp_2MH Complexes for GVB(1/2)*CpCI + Q Wave-Function

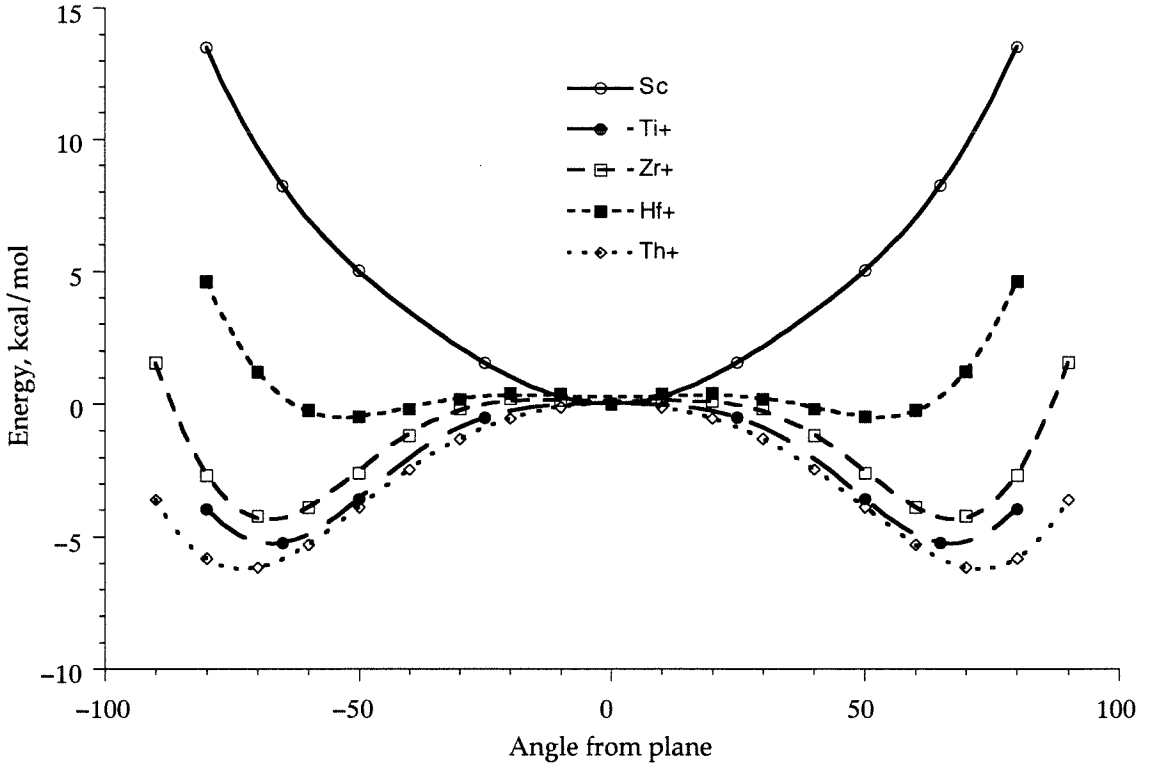

The geometries for the methyl complexes are listed in Table 15. For Ti case, two different angles are used. The first is the same angle as used for the Cp_2TiH^+ studies, 132.6°. In this case, the methyl group resides in the Cp_2Ti plane, in contrast to the prior results. Scanning the energy surface for the inversion, no other minima are found (see Figure 8), although the inversion mode is soft, requiring only 4.03 kcal/mol to move the methyl 50° out of the plane.

It is important to note that the ligand systems in the syndiodirecting catalyst contains a link between the two Cp-like ligands. As the steric interactions are going to be large in a system as crowded as Cp_2TiMe^+, a second Cp-Ti-Cp angle was tested. As there are no published crystal structures of titanium syndiodirecting catalysts, the angle from a known Zr based syndiodirecing catalyst precursor was used. At this Cp-Ti-Cp angle of 118°, it is found that there are two minima, at angles of 0° and 50°, of approximately equal energy

(within 1 kcal/mol), separated by a 6 kcal/mol barrier, and a third minimum 3 kcal/mol higher, separated by a 6 kcal/mol barrier.

Table 15. Geometries for $Cp_2M(CH_3)$ Species

Metal	M-Cp	CpMCp	M-C	Plane-Me	Inversion Barrier
Sc	2.17	143.0	2.28	0.0	0.0[a]
Ti^+	2.07	132.6	2.20	0.0	0.0[a]
Ti^+	2.07	118.0	2.26	0.0	0.0[a]
Y	2.388	118.0	2.631	0.0	0.0[b]
Zr^+	2.19	118.0	2.321	50.0	2.47[b]
La	2.531	118.0	2.702	0.0	0.0[b]
Hf^+	2.20	119.4	2.36	50.0	1.21[b]
Th^+	2.53	118.0	2.543	60.0	4.23[b]

Distances in Å, angles in degrees
[a]Energies in kcal/mol for GVB(1/2)*CpCI + Q wave-functions
[b]Energies in kcal/mol for CpMCPF wave-functions

This result is important for the homogeneous syndiodirecting catalysts, as it indicates that the link between two Cp-like ligands, which decreases the Cp-metal-Cp angle considerably, is quite important. Decreasing this angle reduces the steric congestion sufficiently to allow the methyl group to move out of the Cp_2M plane. It must be noted that these metallocene calculations suffer because the potentials that are derived are non-adiabatic: only the one particular internal coordinate (inversion) is allowed to vary, while the rest are fixed. Because of this restriction, there are calculational artifacts introduced via the strong steric interactions between the rings and the methyl, ones that would be relieved by allowing the structure greater freedom.

To more fully determine the effect of the linking group on the geometry of the metallocenium species, the geometries of Cp_2ZrMe^+ and $CH_2(C_5H_4)_2ZrMe^+$ were fully optimized at the HF level; the results are listed in Table 16. It is found that the free zirconocene methyl cation exhibits a nearly planar geometry (only 14.5° out of the plane) for a large CpZrCp angle of 137.94° and ZrCp distance of 2.26 Å. The tied zirconocene exhibits a non-planar geometry of nearly 23° for a smaller CpZrCp angle of 115.96° and a ZrCp distance of 2.26 Å. While a larger difference for the inversion angle was anticipated

based on the results previously discussed, this difference does prove that the linking group, by increasing the Cp-M-Cp angle, increases the out-of-plane bias for the metallocenium alkyls.

For comparison, previously optimized geometries for both the unlinked[28] and the silyl linked zirconocenium methyl cation[29,28] and the crystal structure of bis(cyclopenta-dienyl)zirconium dimethyl species[30] are listed. It is interesting that Yoshida, *et al.*[29] do not find a non-planar geometry for their silyl linked structure, even though the Cp-Zr-Cp angle is smaller than that found for the unlinked structure; they do find, however, that the inversion mode is very soft (only 3 kcal/mol is required to move the methyl group 60° out of the plane). It is quite possible that their basis sets for the $H_2Si(Cp)_2$ fragment, STO-3G, is inadequate to properly describe the Zr-Cp bonding, underestimating the amount of M→L charge transfer. Woo, Fan, and Ziegler,[28] in their studies of both unlinked and silyl linked zirconocenium methyl species, find even larger inversion angles than are found in the current study: 45.8° for $Cp_2Zr(CH_3)^+$ and 53° for $H_2Si(C_5H_4)_2Zr(CH_3)^+$; in agreement with Yoshida, *et al.*, Woo, Fan, and Ziegler report an inversion barrier of 1 kcal/mol. The qualitative results are consistent with the present study, in that non-zero inversion angles are found and that the linked systems exhibit a larger inversion angle.

It should also be noted that the optimized geometry for the Cp_2ZrMe^+ species is quite similar to the experimental geometry for the Cp_2ZrMe_2 species; the main difference being a slight opening of the CpZrCp angle, which would be expected because the methyl-Cp steric stress is reduced by removal of a methyl group. In addition, there is a slight lengthening of the ZrCp distance. This lengthening could be due to a number of factors, including the positive charge on the complex, leading to a slightly reduced backbonding from the metal to the Cp rings.

Table 16. Optimized Geometries of Cp_2ZrMe^+ and Linked $R(C_5H_4)_2ZrMe^+$ Species

Species	R(ZrCp)	R(ZrC)	θ(CpZrCp)	θ(CpZrC)	θ(plane-C)	Ref.
Cp_2ZrMe^+	2.26	2.26	137.94	110.3	14.5	this work
$CH_2(Cp)_2ZrMe^+$	2.24	2.26	115.96	119.9	22.7	this work
Cp_2ZrMe^+	2.19	2.18	138.6	nr	45.8	28
$SiH_2(Cp)_2ZrMe^+$	2.18	2.17	127.1	nr	53.0	28
$SiH_2(Cp)_2ZrMe^+$	2.215	2.263	123.6	118.2	0.0	29
Cp_2ZrMe_2	2.23	2.277	132.5	105.5	47.8	30

Distances in Å, angles in degrees. Values marked "nr" were not reported.

The triple minimum in the Cp_2TiMe^+ inversion potential is also interesting because it consists of two effects conspiring to cause this unusual potential: the steric effects, resulting in the 0° minimum, and the electronic effects , causing the two minima at 50° and 30°. Evidence that this is occurring comes from comparing the titanocenium-methyl results with those for the other metallocenium methyls. The geometry used for the methyl group in the titanocene calculations was that calculated for $Cl_2Ti(CH_3)^+$ methyl group's geometry, which is flattened somewhat compared to the standard tetrahedral methyl angles. For the other metallocenes, a tetrahedral methyl group was found in the $Cl_2M(CH_3)^+$ calculations, and was thus used for the metallocene calculations. In these cases, the inversion potential had the expected double well potential, as there were much less steric strain in these complexes. The calculated zirconocenium methyl inversion mode is qualitatively similar to that for titanocenium-methyl if the $Cl_2Ti(CH_3)^+$ methyl geometry is used: minima are found at 0° and ±35° inversion angles, with barriers of about 2.5 kcal/mol separating them.

The potential energy surfaces for the inversion mode for the $Cp_2M(CH_3)$ complexes are plotted in Figure 8. All three group three metallocenes have a minima only at a planar structure (0°), although the stiffness of the inversion mode varies considerably. Scandium, due to its small size, has considerable bad steric interactions as the methyl group is moved out of the plane; thus, it requires about 16 kcal/mol to move the methyl 50° out of the plane. Y requires about 3.6 kcal/mol, while for La the motion essentially no energy is required for the motion. This result is similar to the one from the Cl_2LaH system, and is quite

interesting. One reason for it is the lack of steric stress exerted by the Cp rings in the lanthanocene complex, compared to the Sc and Y complexes, due to the long La-Cp distances; thus, free motion is allowed. But it does suggest that, of all three group three complexes, La would show the most promise as a syndiodirecting catalyst.

Figure 8. Energy Surfaces for the Inversion Mode in $Cp_2M(CH_3)$ Complexes for GVB(1/2)*CpCI + Q or CpMCPF Wave-Functions

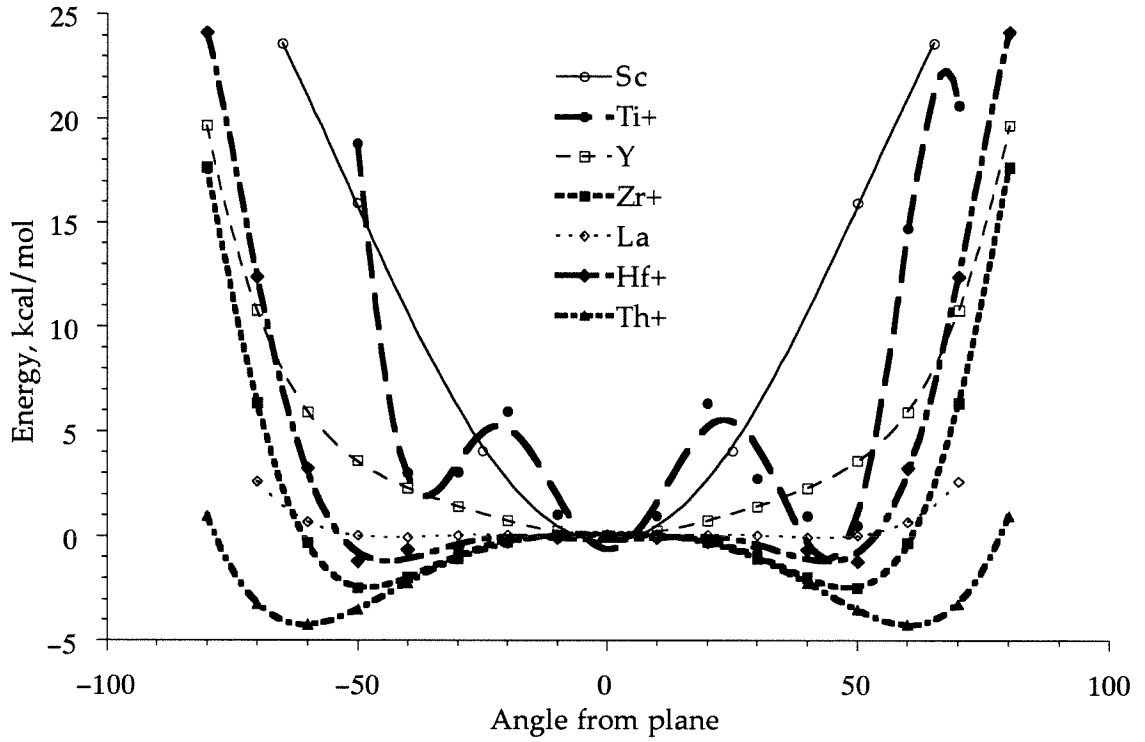

Thorium is apparently the "best" of the group four cations, due to its having the highest inversion barrier (about 5 kcal/mol) compared to Zr (about 2.5 kcal/mol) and Hf (about 1.2 kcal/mol) and the largest out-of-plane angle. Part of this superiority is due, like La, to longer M-Cp distances. Both Zr and Hf have about the same M-Cp distances, about 2.2 Å. Because of this similarity in structure, the steric stresses between the zirconocene and hafnocene complexes should be similar; any difference in behavior between catalysts based on the two metals is likely electronic in origin.

Conclusions

Cationic, group four, Ziegler-Natta model complexes, including thorium, have a strong bias for having the alkyl or hydride ligand move out of the plane described by the metal and the other two ligands. In the case of hydrides, the preference is quite dramatic, whereas for methyl complexes the preference is tempered by steric and electrostatic repulsions. The group three neutral complexes are planar and require significant amounts of energy to move the alkyl group out of the plane. The non-planar geometries have been used by Ewen, *et al.*[3], as a basis for their syndiodirecting mechanism. Thus, group four metals, due to the metal electronic structure, exhibit geometries consistent with this mechanism and are *known to form syndiodirecting catalysts*, while group three metals exhibit geometries that are inconsistent with this mechanism. *No group three metal is known to form a syndiodirecting catalyst.*

In general, the differing preference for the non-planar geometry decreases as one moves down the periodic table: Ti^+ and Sc have the greatest difference, while Hf^+ and La have the smallest difference. Indeed, it is found that an inversion of up to 50° requires no energy for La complexes. Thus, of all of the group three metals, La shows the greatest promise for having the correct *electronic structure* to be used in a syndiodirecting catalyst. This prediction must be qualified by the fact that the steric requirements necessary for syndiospecificity[§] have not been assessed: La is much larger, and thus the standard syndiodirecting ligand system (linked Cp and Fluorenyl groups) may be too far away from the reaction center to direct the enantioselectivity of the incoming monomer. The same is true for Th. While the thorocenium-methyl species shows the greatest preference for non-planarity, this preference is most likely due to the enlarged wedge area. It is not obvious

---

[§]Molecular-mechanics simulations are described for Zr systems in Chapter III; the longer La-Cp distances render the transfer of even qualitative results from these calculations suspect.

that the syndiodirecting ligand environment will exert enough enantioselectivity to produce a syndiotactic polymer.

An useful comparison can be made between the zirconocene and hafnocene catalysts. Due to the relativistic contraction, hafnium and zirconium complexes have remarkably similar geometries and the steric stresses exerted by the ligand environment around the metal should be nearly the same for both. Thus, any differences that arise between catalysts with equivalent ligand environments should be due solely to the difference in metal electronic structure. From the calculations, it is found that zirconocene complexes have a greater bias for out-of-plane motion than do hafnocene complexes. Thus, zirconium based catalysts are expected be more strongly syndiodirecting than the analogous hafnium based catalysts. Experimental work by Ewen and Elder[31] support this conclusion. They find that within the catalyst system $(CH_3)_2C$(cyclopentadienyl)(1-fluorenyl)MCl_2 [^{i}Pr(Cp)(Flu)MCl_2], trityl tetrakis(pentafluoro-phenyl)borate [CPh_3 $B(C_6F_5)_4$], M= Zr, Hf, Zr based catalysts are more syndiospecific than the Hf based catalyst (based on a comparison of relative pentad concentrations containing stereoerrors; see Table 17).**

Table 17. Errors in Syndiospecific Polypropylene produced with Zr and Hf catalysts

Catalyst System	%rmmr	1/2 %[xrmx]
^{i}Pr(Cp)(Flu)$ZrCl_2$/CPh_3 $B(C_6F_5)_4$	1.4	0.50
^{i}Pr(Cp)(Flu)$HfCl_2$/CPh_3 $B(C_6F_5)_4$	4.6	1.9

Data taken from reference 31. Polymerization temperature was 20° C. Zr polymerization run in toluene, Hf run in bulk.

To date, there has been no direct experimental evidence for or against the nonplanar structures, other than the syndiotactic polymerization data. Some indirect evidence comes from experiments coupled with calculations of [η^5-1,2-$(CH_3)_2C_5H_3]_2ZrCH_3^+ \bullet CH_3B(C_6F_5)^-$

**While an α-carbon rearrangement has been postulated to account for observed stereoerrors (see Chapter I), and would be anticipated to affect the quantitative conclusions from the data, the data should still be qualitatively valid.

a well defined, cationic catalyst. From NMR studies, Yang *et al.*[5] find that the methyl resides out of the Cp-Zr-Cp plane, with a barrier to interchange between the methyl and the borate anion of 18.3±0.2 kcal/mol at 80° C. It must be kept in mind that this value includes the cation-anion interaction, which is the major cause of the inversion barrier and difficult to separate from other effects. In an attempt to understand this exchange and determine the magnitude of the component effects, Castonguay and Rappé[1b] calculated the energy surface using molecular mechanics. In the presence of the counterion, they calculated the interchange barrier to be about 10 kcal/mol; in the absence of the counterion they found the barrier to be about 4 kcal/mol, so that the counterion accounts for 60% of the barrier. Taken together, these other results suggest that 7.3 of the 18.3 kcal/mol barrier is due to a non-planar bias. This value is in reasonable agreement with the value of about 6 kcal/mol for the Ti^+ species, although it is considerably larger than the value of 2.5 calculated for the Zr^+ species.

It is generally accepted that the group four catalysts are far superior than group three catalysts in their activities. Previously, Steigerwald and Goddard[14a] showed the related reaction $Cl_2MH + D_2 \rightarrow Cl_2MD + HD$ has a smaller barrier for Ti^+ than for Sc and Ti. They showed that at the transition state, the metal character in the M-H bonds is 100% d, and hence increased metal d character in M-H bond leads to a lower barrier for insertion. The group four cationic complexes have the greatest metal d character in the M-H bonds, and thus should be better catalysts. In addition, part of the superiority of group four cationic catalysts is due to the influence the ground state geometry has on the energy of the transition state. For the group three catalysts, there is a significant reorganization energy associated with olefin complexation that is not present in the group four cationic systems. Assuming that the intrinsic olefin binding energy is the same for both the group three and the corresponding group four systems (most likely it would be stronger for the cations) and that the olefin binding requires a 50° out-of-plane angle, the results presented suggest that

Ti^+ has a 9-12 kcal/mol, Zr^+ a 4 kcal/mol, and Hf^+ a 1.2 kcal/mol greater olefin binding energy than the corresponding group three complexes[††] in the Cossee-Arlman mechanism. Since the intrinsic binding of the olefin is greater for the cationic than the neutral species, the affinity of the group four systems for the binding step is expected to be even greater. Previous theoretical results suggest that the intrinsic binding energy to $Cl_2Ti(CH_3)^+$ may be as large as 50 kcal/mol in the gas phase.[1]

The calculations for the neutral group four species suggest that Ti(III), Zr(III), and Hf(III) systems would have lower activity, due to the ground-state geometric effects described above. Indeed, the only insertion reactions found experimentally for Ti(III) systems are into the Ti-H bond of Cp^*_2TiH and 2-butyne into $Cp^*_2Ti(CH_3)$.[32]

An interesting series of results described above points to the importance of the linking group in the rigid, stereodirecting metallocenes. Comparing the results of Cp_2TiMe^+, in which two different Cp-Ti-Cp angles were considered, and considering the fully optimized geometries of $Cp_2Zr(CH_3)^+$ and $H_2C(C_5H_4)_2Zr(CH_3)^+$, the conclusion is drawn that smaller Cp-M-Cp angles (creating a more open wedge) are necessary for the appearance of the non-planar effect.

It is interesting to compare the current results with those previously published for related metallocene complexes. It has been previously discussed that Yoshida *et al.*[29] find planar geometries for silyl-linked metallocenes of Ti^+, Zr^+, and Hf^+, in contrast to the results shown here. It is interesting to note that they find non-planar geometries for the metallocenium *hydride* complexes for all three metals: Zr has the largest (58.1°) and Hf the smallest (9.0°) inversion angles, in qualitative agreement with the results discussed above: Zr^+ complexes have a greater out-of-plane bias than do Hf^+ complexes. Ti has a 42.7° inversion angle, but the Cp-Ti-Cp angle was larger than for the zirconium and hafnium complexes, thus decreasing the relative out-of-plane bias for the Ti complex. In addition,

---

[††]It is assumed that the polymer must have an out-of-plane angle of about 50° away from

both Woo, Fan, and Ziegler[28] and Jolly and Marynick[1a] found a non-coplanar structure for Cp_2TiMe^+. Jolly and Marynick discounted their results as being unimportant, as they calculate the inversion barrier to be about 3 kcal/mol.

Examining the experimental data of Ewen *et al.*,[3] it is found that the linking group has a dramatic effect on the syndiospecificity, in agreement with the results described above. In comparing the syndiotacticity of the resulting polymers[‡‡] from the two catalyst precursors shown in Figure 9, the isopropyl-linked catalyst system (Figure 9a), which has a Cp-Zr-Cp angle of 117.9°, produces polypropylene with a syndiotacticity of 72%, while the dimethylsilyl-linked catalyst system (Figure 9b), which has a Cp-Zr-Cp angle of 128.2°, produces polypropylene with a syndiotacticity of 24%. In addition, Ewen *et al.* also determined the percentages for the two types of errors, single and double insertion errors (see Chapter I) for both systems: the isopropyl system had 2.25% m errors and 2.8% mm errors, while the dimethylsilyl system had 10.5% m errors and 6% mm errors. A preponderance of double errors indicates errors in enantioface selectivity based on site control, while excess single errors can indicate two types of errors, reverse enantioface errors within a chain control stereoselectivity or site migration without insertion within a migratory insertion stereoselectivity. The results from the current study are consistent with an increased Cp-M-Cp angle leading to greater site migration errors, and so are wholly consistent with these stereopolymerization data.

Qualitatively, the polymerization results reinforce the ideas developed above: namely that (1) the greater the non-planar effect, the greater the syndiodirecting capability of the catalyst; (2) the larger the wedge (or, correspondingly, the smaller the CpMCp angle), the greater the non-planar effect; and (3) the stereoerrors due to the breakdown of the non-planar effect are site migration or "inversion" errors, leading to single insertion errors. Thus, in contrast to the isodirecting catalysts, in which larger linking groups are

---

the plane in order to make room for the incoming monomer.

acceptable, the syndiodirecting catalysts require as small a linking group as possible for greater stereocontrol.

Figure 9. Syndiotactic Catalyst Precursors

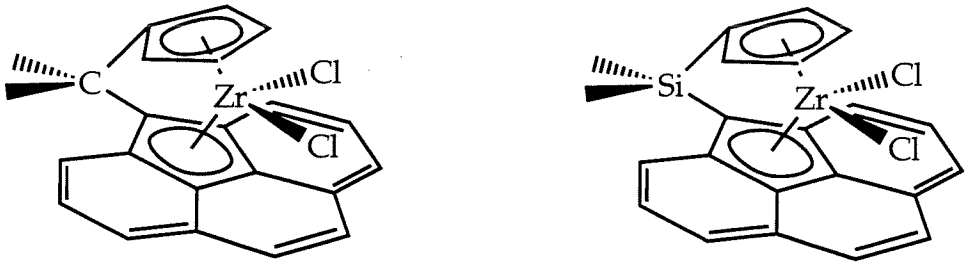

(a) (b)

Most calculations of the transition state for ethylene insertion into MCH_3 bonds have shown that the barrier is about 10-15 kcal/mol higher than the complexation step.[1,28,29] In solution there should be a barrier for the complexation step, due to displacement of weakly coordinated solvent molecule or counterions. Thus, the three solution phase energy profiles in Figure 10 are possible for the reaction sequence. For the group three systems (a), the insertion step is expected to be rate-determining as the complexation step would be endothermic, due to (1) the large reorganization energy, (2) a small intrinsic binding energy, and (3) the energy required for solvent displacement. For the group four cations, the binding step should be exothermic (b); the most recent calculations for metallocene complexes calculate a binding energy of about 30 kcal/mol for all three systems.[1] This exothermicity means that if the insertion barrier is small enough, the binding step may be rate-determining (c), with the barrier due to solvent or counterion displacement. Currently the most widely accepted profile for the group 4 cations is that shown in (b).

[‡‡]Based on %rrrr pentads for a polymer produced at a polymerization temperature of 60° C

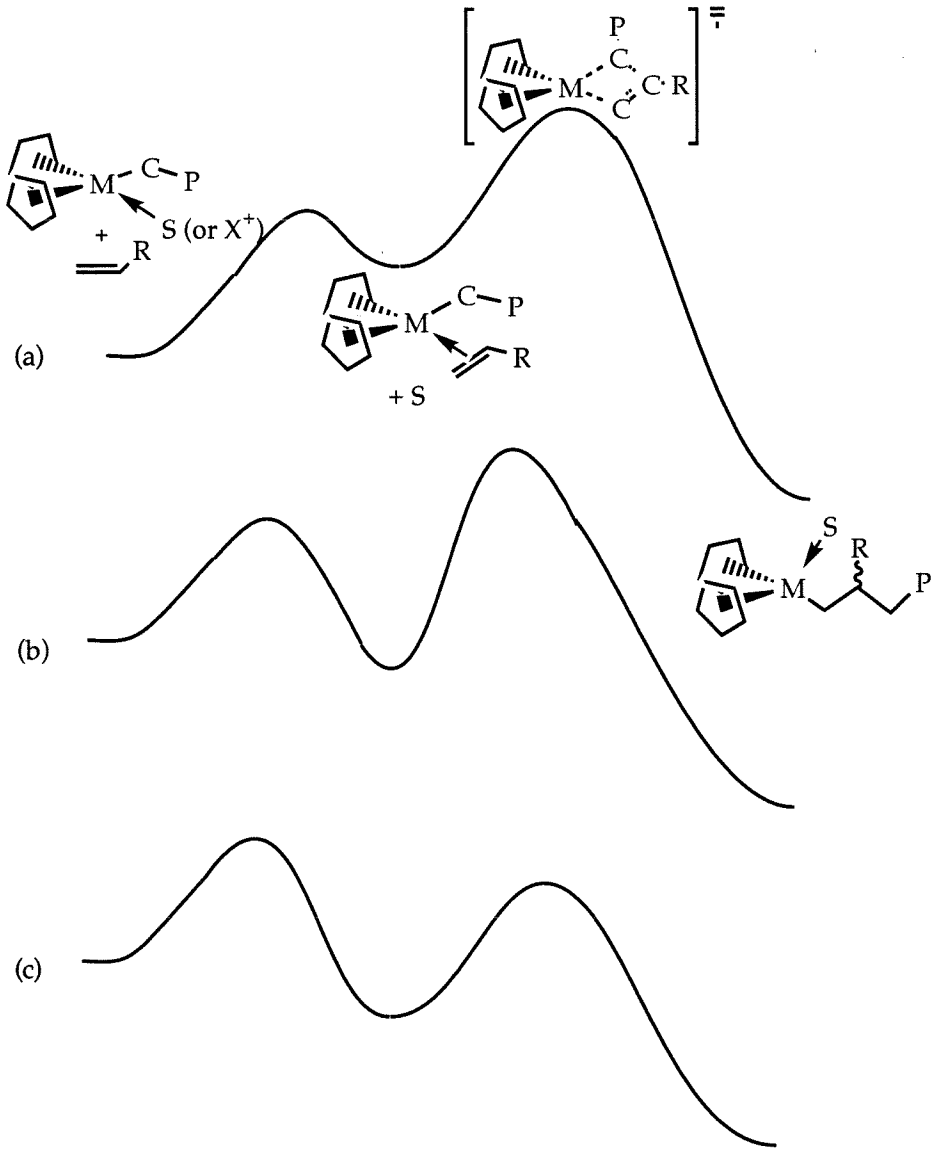

Figure 10. Solution-Phase Energy Profiles for (a) Endothermic Olefin Binding, Rate Determining Insertion Step, (b) Exothermic Olefin Binding, Rate Determining Insertion Step, and (c) Exothermic Olefin Binding, Rate Determining Binding Step.

Isotopic substitution experiments have been performed to test the importance of an α-agostic assisted mechanism in the insertion step, with differing results for the group 3 and group 4 systems.[2a,b,33] In scandium systems a deuterium kinetic isotope effect (KIE) is observed, while for Ti^+ systems no such KIE is observed, and for Zr^+ a KIE is sometimes observed. The differences in the results can be rationalized using the above reasoning. Since the rate-determining step for the group 3 systems would be insertion, experiments

would always be expected to show a KIE for a mechanism involving α-agostic assistance for olefin insertion. If, on the other hand, olefin binding is rate-determining, as, for example, with an unhindered group 4 alkyl cation, little or no KIE would be observed, even if the (faster) olefin insertion step occurred with α-agostic assistance.

Appendix: Calculational Details

Methods

The Hartree-Fock (HF) level of theory, a generalization of simple Molecular Orbital (MO) theory, is a standard beginning point for much electronic structure calculations. While popular and relatively inexpensive computationally, it has severe shortcomings, the most important of which is that it describes the interaction amongst electrons in only an average, static manner (*i.e.*, HF includes only static correlation). The instantaneous interactions between electrons as they move around within the molecule (*i.e.*, dynamic correlation) are not described properly.

The simplest manner in which to include some of the dynamic correlation missing in HF wave-functions is through Generalized Valence Bond (GVB) theory.[34] A more detailed description of the method is found in Chapter V of this thesis, but a short description will be given here. In the HF theory, each molecular orbital is assumed to contain two electrons; thus these two electrons occupy the same region of space. GVB represents an introduction of Valence Bond (VB) theory, in which each bonding pair is formed in the manner:

$$\Psi^{VB} = \big(l(1)r(2) + r(1)l(2)\big)\big(\alpha(1)\beta(2) - \beta(1)\alpha(2)\big)^{\S\S} \qquad (1)$$

[§§]Note that r and l refer to the atomic orbitals centered on the right and left centers of the bond respecitvely, 1 and 2 refer to electrons 1 and 2, and α and β refer to the standard spin functions.

into HF theory. Whereas HF wave-functions will not properly describe bond dissociation events, GVB wave-functions will.

While the GVB wave-function provides a superior description of a covalent bond, it does not describe properly the correlation among the remaining electrons. To properly calculate the energetics of different geometric configurations, it is necessary to include more electron-electron correlation in the wave-functions. Two methods are used to introduce this correlation into the wave-functions: Configuration Interaction (CI) theory and Modified Coupled Pair Functional (MCPF) theory.[35]

In CI theory in general, the manner in which correlation is introduced is by allowing other "excited states" (with relation to the HF ground state) to mix into the wave-function. It is known that the ground state wave-function from HF theory is not the correct ground state, so that the HF excited states are not true excited states. Allowing the different states to mix to give the lowest energy results in a wave-function that is a more correct description of the ground electronic state. However, as the number of orbitals grows, the number of excited states grows roughly exponentially. Thus, an important consideration for CI theory is which excitations to include. It has been found that in general, single and double substitutions (the excitation of a single electron into all virtual orbitals and the excitation of two electrons into all virtual orbitals respectively) provide a sufficient amount of correlation to give a good description of the ground state. For Hartree-Fock, this wave-function is denoted as HF*SD.

A better wave-function than HF*SD, which allows excitations from only the HF ground state (reference), allows excitations from multiple references; in such a manner are higher levels of substitution (such as triple and quadruple) achieved to effectively describe the important bonds of a molecule. Thus, a wave-function used for this study takes the two states of a GVB(1/2) wavefunction and allows all single and double excitations; this wavefunction is denoted GVB(1/2)*SD.

One severe shortcoming of CI theory is that it is not size consistent. Via the Davidson correction,[36] CI wave-functions can be made approximately size consistent. Thus, all reported values for CI wave-functions include the Davidson correction. However, as the number of electrons being correlated grows, the quality of CI wave-functions deteriorates. A wave-function that is very similar HF*SD, and yet maintains size-consistency, comes from MCPF theory. This single reference correlation method has been shown to give very good results for wave-functions in which the dominant configuration represents greater than 90% of the correlated wave-function.[23b]

For the metal-chloride systems all single and double excitations from the GVB(1/2) wavefunctions (two configurations) were allowed, denoted as GVB*SD. For the Cp_2MH systems, this GVB*SD calculation was not practical, and a restricted set of excitations was utilized. For accurate energies, it is imperative that the metal be described as well as possible, so a CI wave function was calculated using the two GVB-PP configurations as references, but restricting the reference space to the M-H bond and the six π-orbitals on the Cp's. This wave function, denoted as GVB*CpCI, should adequately describe the metal-Cp interactions.

MCPF calculations were used for the $Cp_2M(CH_3)$ systems, as the HF wave-function represents a truly dominant (>90%) configuration. Again, a restricted set of excitations was used for these calculation, and the wave-function is denoted as CpMCPF. It was impossible to use only six Cp π-orbitals, due to extensive mixing between the ring orbitals, especially as the methyl group moved in the plane. The minimum number necessary for a consistent description of the methyl motion was used, either 7 or 8. In addition, the M-C and three C-H bonds were included in the reference space

It is found that electron correlation is critical to describing the inversion properly for the metallocenes. As can be seen for Hf^+, the inversion is not present at the HF level, and it is underestimated for both Zr^+ and Th^+. The most important excitations present in the

correlated wave-functions describe the Cp-Zr bonding (mainly metal to ligand charge transfer). It is known metallocenes require highly correlated wave-functions to properly describe the metal to ligand and ligand to metal charge transfers. However, the early metals do not likely involve much ligand to metal backbonding, so HF was hoped to be a reasonable description.

Figure 11. Total and Relative Energies at Inversion Angles 0° and 50°, $Cp_2M(CH_3)^+$, M=Y, Zr^+, La, Hf^+, Th^+, HF and MCPF Wave-Functions.

	$\theta = 0°$		$\theta = 50°$		ΔE	ΔE
Metal	HF	MCPF	HF	MCPF	HF	MCPF
Y	–461.4817162766	–461.80636398	–461.4741718081	–461.80063619	4.734	3.594
Zr^+	–469.8170189553	–470.16792023	–469.8178750062	–470.17186196	–0.537	–2.473
La	–454.8044856723	–455.07583086	–454.8022927927	–455.07579977	1.376	0.020
Hf^+	–472.1284024996	–472.45740808	–472.1221535980	–472.45933576	3.921	–1.210
Th^+	–446.4514864974	–446.78777759	–446.4547494462	–446.79337674	–2.048	–3.514

Total energies in hartree, relative energies in kcal/mol

All GVB calculations were performed with the perfect-pairing restriction for a single valence bond structure. The calculations were carried out using the GVB suite of programs,[37] the MOLECULE-SWEDEN suite,[38] and the PS-GVB suite of programs.[39] Unless otherwise noted, only the M-R bond was correlated in a single GVB pair (GVB(1/2)). Reported charges were calculated using the Mulliken approximation.[40]

Basis Sets and Effective Core Potentials

In addition to the method used for including electron correlation, the choice of basis set is of great importance. As the size of the calculation grows roughly as N^4, where N is the number of basis functions, it is of paramount importance to use a basis set that is large enough to adequately describes the chemistry, but no larger. It has been found that describing the valence orbitals with two functions (called a double-ζ basis set) gives enough freedom in the valence space to allow a good description of the geometries of the molecules. While such bases are inadequate to describe bond forming and breaking

reactions, they are sufficient for the purposes of this work. When calculating energetic differences between geometries for the dichloro systems, polarization functions were added to the alkyl ligands bonded to the metal, to improve the description of this bond.

For all the carbon atoms the Dunning-Huzinaga double-ζ basis (9s5p/3s2p) was used and included polarization functions (ζ=0.75) for the $Cl_2M(CH_3)$ systems for energetic calculations. The hydrogen basis set was the unscaled set of Dunning-Huzinaga (5s/3s) if bonded directly to the metal, otherwise it was the scaled set (4s/2s) (ζ=1.2); for energetic calculations the (5s/3s) set was augmented by a polarization function (ζ=0.60).

In the cases of larger atoms, with many core electrons that do not participate directly in the chemistry occurring in the valence space, it is often desirable to replace these core electrons with functions, to reduce the number of basis functions in the calculations. Such effective core potentials (ECP's) and their corresponding basis sets have been derived for many atoms of the periodic table, and provide an inexpensive and reliable manner by which to reduce the computational demands. ECP's were utilized to describe the core electrons of the metals, chlorine, and silicon.[41] These ECP's were derived from all electron atomic calculations. For chlorine and silicon, the Ne core is replaced so that there are seven and four valence electrons, respectively, the ECP's and basis sets come from the work of Rappé, Smedley, and Goddard.[42]

For the metals, the outer core electrons (3s and 3p for Sc, Ti; 4s and 4p for Y, Zr; 5s and 5p for La, Hf) were treated explicitly, except in the case of thorium, where only the outer core p electrons (6p) were treated explicitly. Thus, 8+3=11 electrons were treated explicitly for all the metals except for thorium (9 electrons). For all metals except thorium, the basis sets and ECP's are from the work of Hay and Wadt.[43] For the cations, it was found that the published basis sets (and as shall be seen for Hf^+, the ECP's) did not properly describe the cationic state splittings (see Table 18). It was found that a simple

recontraction of the basis sets for the cation improved the splittings considerably; the basis sets recontracted for the cations are listed in Table 19.

The basis set and ECP for Th is from the work of Wadt;[44] this set includes f functions. The f functions were found to be unnecessary for geometry optimizations by Brusich,[6] and so were not used for geometry optimizations of thorium complexes. The f functions, however, were used for energetic calculations.

Table 18. Absolute Energies and State Splittings for Metal Cations Ti^+, Zr^+, and Hf^+, Published and Recontracted Basis Sets.

Ion	Basis/ ECP Set	State (Calc Level)	Absolute Energy (hartree)	$\Delta E(E(s^2d^1) - E(s^1d^2))$ (eV)	
				Calculated	Experiment[a]
Ti^+	Published	(s^2d^1) (GVB)	–57.07539410		
		(s^1d^2) (HF)	–57.28405926	–5.68	–3.08
	Recontracted	(s^2d^1) (GVB)	–57.14591199		
		(s^1d^2) (HF)	–57.30232219	–4.26	–3.08
Zr^+	Published	(s^2d^1) (GVB)	–45.67949738		
		(s^1d^2) (HF)	–45.77755286	2.67	1.71
	Recontracted	(s^2d^1) (GVB)	–45.71049159		
		(s^1d^2) (HF)	–45.78682461	2.08	1.71
Hf^+	Published	(s^2d^1) (GVB)	–48.03792516		
		(s^1d^2) (HF)	–48.05894528	–0.57	0.56
	Modified	(s^2d^1) (GVB)	–48.02438346		
		(s^1d^2) (HF)	–48.00536705	0.52	0.56

[a]Experimental data from ref. 15

Table 19. Recontracted Basis Sets for Metal Cations Ti^+, Zr^+, and Hf^+, Based on Basis Sets from the Work of Hay and Wadt[43]

	Ti^+		Zr^+		Hf^+	
	ζ	c	ζ	c	ζ	c
ns	4.3720	-0.3667	1.9760	-0.9250	1.950	-1.2395
	1.0980	0.8360	1.1540	1.1040	1.1830	1.5882
	0.4178	0.4025	0.3910	0.6723	0.3897	0.4886
(n+1)s	1.0980	-0.0603	1.1540	-0.0542	1.1830	-0.0505
	0.4178	-0.2949	0.3910	-0.2773	0.3897	-0.4845
	0.1452	0.5837	0.1001	0.9160	0.1656	0.8887
	0.0523	1.0000	0.0334	1.0000	0.0424	1.0000
np	12.52	-0.463	4.1920	-0.0949	1.9720	-0.6343
	1.491	0.6346	0.8764	0.6873	1.3540	1.0511
	0.4859	0.4598	0.3263	0.4112	0.4134	0.5708
(n+1)p	0.0530	1.0000	0.0724	1.0000	0.0804	1.0000
	0.016	1.0000	0.0243	1.0000	0.0274	1.0000
nd	20.2100	0.0287	2.2690	0.0488	0.8226	0.3585
	5.495	0.1433	0.7855	0.3884	0.2585	0.5163
	1.699	0.3706	0.2615	0.4742	0.0762	1.0000
	0.484	0.4739	0.0802	1.0000		
	0.1157	1.0000				

When developing ECP's for the metals, it is important to determine which state should be used, as this state influences the quality of the ECP. For all the metals, the ECP's were derived for the s^1d^{n-1} states. For Sc-Zr, these ECP's reasonably reproduce the experimental state splittings when recontracted bases (Table 19) are used (see Table 2 and Table 5) In the case of La and Hf, however, the published ECP's and basis sets do not give the correct state splittings (they are inverted; see Table 20). In order to correct for this misordering of the states, an empirical modification was made to the ECP. It is desired that such a modification would only affect the relative energies of the s and d orbitals and *not change the size of the orbitals in the valence region.* This last point is quite important, as such a modification would affect the manner in which the element bonds.

Table 20. Total Energies and State Splittings, La and Hf+ for (a) Published and (b) Modified ECP's and Basis Sets.

Atom/Ion	Basis/ ECP Set	State (Calc Level)	Absolute Energy (hartree)	$\Delta E(E(s^2d^1) - E(s^1d^2))$ (eV)	
				Calculated	Experiment[a]
La	Published	(s^2d^1) (GVB)	–30.76400796		
		(s^1d^2) (HF)	–30.77016612	–0.17	0.36
	Modified	(s^2d^1) (GVB)	–30.73346530		
		(s^1d^2) (HF)	–30.71925845	0.39	0.36
Hf^+	Published	(s^2d^1) (GVB)	–48.03792516		
		(s^1d^2) (HF)	–48.05894528	–0.57	0.56
	Modified	(s^2d^1) (GVB)	–48.02438346		
		(s^1d^2) (HF)	–48.00536705	0.52	0.56

[a]Experimental data from ref. 15

Effective core potentials have the form:

$$\sum_k c_k r^{n_k} e^{-\zeta_k r^2} \qquad (2)$$

for each potential term (s, p, d, f, g, etc.), where n_k varies from 0 to 2 and r is the distance from the nucleus. As it is desired to change the relative orderings of the calculated states so that the experimental values are reproduced, it is necessary to either stabilize the s orbital or destabilize the d orbital. The d orbital was destabilized by modifying the contribution to the potential nearest the nucleus ($n_k = 0$), making sure that the size in the valence region was not modified considerably. Thus, the coefficient of the term with the largest exponent (describing the region nearest the nucleus) for $n_k = 0$ was changed so that the experimental state splittings were reproduced. These coefficient modifications are listed in Table 21. It can be judged how successful these modifications to the ECP's are by recontracting the two d primitives for the inner d orbital for La: before the modification, the coefficients were 0.36575 and 0.535653, and after were 0.2646 and 0.5250, indicating the new ECP successfully modified the energy without changing the size of the d orbitals. Because the change was so minor, the published basis set for La was used in all calculations with the modified ECP (the Hf^+ basis is listed in Table 19).

Table 21. Modified ECP's for La and Hf+

Atom	Potential Term	ζ	c_k (old)	c_k (new)
La	d-f	18.5050798	137.4078176	6000.000000
Hf	d-g	32.0227449	217.5811427	5000.000000

For energetic calculations of Sc and Ti compounds, a modified basis set, derived from the FOURS basis set of Rappé and Goddard,[45] was used in conjunction with the ECP's developed by Hurley *et al.*[46] This set is listed in Table 22.

Table 22. Basis Sets Developed for the Hurley *et al.* ECP's

	Sc		Ti^+	
	ζ	c	ζ	c
ns	11.12	0.01680	12.40	-0.175
	4.205	–0.37353	4.7170	0.3863
	1.169	0.62961	1.340	–0.6408
	0.431	0.60351	0.4880	–0.6040
(n+1)s	4.205	0.05078	4.7270	–0.0607
	1.169	–0.12935	1.340	0.1574
	0.431	–0.27675	0.4880	0.3321
	0.0825	0.54725	0.10723	–0.8070
	0.03376	1.0000	0.04483	1.0000
np	1.494	0.4730	1.7110	0.4719
	0.4602	0.6220	0.5256	0.6256
(n+1)p	0.08925	1.0000	0.10723	1.0000
	0.03376	1.0000	0.04483	1.0000
nd	15.132864	0.0390	20.120	0.0343
	4.204818	0.1779	5.4950	1.711
	1.303034	0.4429	1.6990	0.4456
	0.368257	1.0000	0.4840	0.5422
	0.081226	1.0000	0.1157	1.0000

Geometries

When using quantum mechanics to study molecular geometric information, it is ideal to fully optimize the energy with respect to the nuclear coordinates, as geometry optimizations assure that no geometric artifacts are introduced into the computations. This

process is generally performed using gradient methods,[47] in which the gradient (first derivative of the energy with respect to the nuclear coordinates) is used to determine a more optimal geometry. The time for the gradient computation is dependent on both the quality of the wavefunction (simpler methods are cheaper computationally) and the size of the molecule; the time of the computation grows as roughly 3N, where N is the number of nuclei, and also with the number of basis functions (see above). For the smaller systems (dichlorometal hydrides and alkyls), it is feasible to perform full geometry optimizations, as there are at most 7 atoms and a small number of basis functions. The geometries of the Cl_2MH were optimized at the GVB(1/2) level, in which the M-H bond was correlated, while the geometries of $Cl_2M(CH_3)$ were optimized at the HF level. These levels, HF and GVB, have been determined to give very satisfactory geometries when compared to geometries optimized at much higher levels of correlation. For the larger metallocene systems, in which the number of atoms and basis functions is much larger, full optimizations for every species were clearly impossible.

In performing the geometric calculations on the metallocenes, only the M-R distance was optimized. The rings were fixed such that the metallocene fragment would have a symmetry plane relating the two rings, and that the unique apex of each ring points toward the alkyl group. The C-C and C-H bond lengths in the rings were fixed at 1.40 and 1.08 Å respectively. The metal-ring centroid geometries are reported with other geometric parameters; the rings were assumed to be perpendicular to the metal-centroid bond. In addition, the methyl groups were frozen in reasonable geometries based on the optimized geometries of $Cl_2M(CH_3)$, which are given in Table 12.

Geometries used for the titanocene complexes are from crystal structure data of titanocenes.[27] Two different values were used for the CpTiCp angle: 132.6°, based on the free titanocene data,[27] and 118.0°, based on syndiospecific zirconocene catalyst data.[3] For Y, Zr, La, and Th metallocene complexes, the latter CpMCp angle was used. The scandocene data was taken from the work of Bercaw and coworkers.[4] The yttrocene data

from the work of Marsh, *et al.*,[48] the zirconocene data is from Ewen, *et al.*,[3] the lanthanocene data from the work of Scholz, *et al.*,[49] the hafnocene data from the work of Ewen, *et al.*,[50] and the thorocene data from the work of Sperlet, *et al.*[51]

References

1. (a) Jolly, C. A.; Marynick, D. S. *J. Am. Chem. Soc.*, **1989**, *111*, 7968. (b) Castonguay, L. A.; Rappé, A. K. *J. Am. Chem. Soc.*, **1992**, *114*, 5832. (c) Koga, N.; Morokuma, K. *Chem. Rev.*, **1991**, *91*, 823. (d) Kawamura-Kuribayashi, H.; Koga, N.; Morokuma, K. *J. Am. Chem. Soc.*, **1992**, *114*, 2359. (e) Kawamura-Kuribayashi, H.; Koga, N.; Morokuma, K. *J. Am. Chem. Soc.*, **1992**, *114*, 8687. (f) Seigbahn, P. E. M. *Chem. Phys. Lett.*, **1993**, *205*, 290. (g) Weiss, H.; Ehrig, M.; Alrichs, R. *J. Am. Chem. Soc.*, **1994**, *116*, 4919. (h) Yoshida, T.; Koga, N.; Morokuma, K. *Organometallics*, **1995**, *14*, 746.

2. (a) Piers, W. E.; Bercaw, J. E. *J. Am. Chem. Soc.*, **1990**, *112*, 9406. (b) Krauledat, H.; Brintzinger, H. H. *Angew. Chem., Int. Ed. Engl.*, **1990**, *29*, 1412. (c) Leclerc, M. K.; Brintzinger, H. H. *J. Am. Chem. Soc.*, **1995**, *117*, 1651.

3. Ewen, J.; Elder, M.; Jonew, R.; Haspeslagh, L.; Atwood, J.; Bott, S.; Robinson, K. *Makromol. Chem., Macromol. Symp.*, **1991**, *48/49*, 253.

4. Burger, B. J.; Thompson, M. E.; Cotter, W. D.; Bercaw, J. E. *J. Am. Chem. Soc.*, **1990**, *112*, 1556.

5. Yang, X.; Stern, C. L.; Marks, T. J. *J. Am. Chem. Soc.*, **1991**, *113*, 3623.

6. Brusich, M., Ph. D. Thesis, California Institute of Technology, 1988.

7. See for example references 3, 4, 8, 9, and 10. For a more complete listing, see references Chapter I.

8. See for example Kaminsky, W.; Kulper, K.; Brintzinger, H. H.; Wild, F. R. W. P. *Angew. Chem., Int. Ed. Engl.*, **1985**, *24*, 507. For a more complete listing, see references in Chapter I.

9. See for example ref. 3 and Ewen, J. A.; Jones, R. L.; Razavi, A.; Ferrara, J. D. *J. Am. Chem. Soc.*, **1988**, *110*, 6255. For a more complete listing, see references in Chapter I.

10. Coughlin, E. B.; Bercaw, J. E. *J. Am. Chem. Soc.*, **1992**, *114*, 7606.

11. Jolly, C. A.; Marynick, D. S. *Inorg. Chem.*, **1989**, *28*, 2893.

12. Lauher, J. W.; Hoffmann, R. *J. Am. Chem. Soc.*, **1976**, *98*, 1729.

13. Bierwagen, E. P.; Bercaw, J. E.; Goddard, W. A., III, *J. Am. Chem. Soc.*, **1994**, *116*, 1481.

14. (a) Stiegerwald, M. L.; Goddard, W. A., III *J. Am. Chem. Soc.*, **1984**, *106*, 308. (b) Stiegerwald, M. L.; Goddard, W. A., III *J. Am. Chem. Soc.*, **1985**, *107*, 5027. (c) Rappé, A. K.; Goddard, W. A., III *J. Am. Chem. Soc.*, **1980**, *102*, 5114. (d) Rappé, A. K.; Goddard, W. A., III *Potential Energy Surfaces and Dynamics Calculations*, Truhlar, D. G., Ed.; Plenum Press: New York, 1981; pp. 661-684. (e) Rappé, A. K.; Goddard, W. A., III *J. Am. Chem. Soc.*, **1982**, *104*, 297.

15. Moore, C. E. *Atomic Energy Levels*; Vol. I, NBS Ref. Data Series, NBS 35, U.S. Government Printing Office, Washington, DC, 1971; pp. 259-290.

16. See for example Hoffmann, R. *Angew. Chem., Int. Ed. Engl.*, **1982**, *21*, 711.

17. Low, J. J.; Goddard, W. A., III *J. Am. Chem. Soc.*, **1986**, *108*, 6115.

18. Steigerwald, M. L., Ph. D. Thesis, California Institute of Technology, 1984.

19. Schilling, J. B.; Goddard, W. A., III; Beauchamp, J. L. *J. Am. Chem. Soc.*, **1986**, *108*, 582.

20. Schilling, J. B.; Goddard, W. A., III; Beauchamp, J. L. *J. Am. Chem. Soc.*, **1987**, *109*, 5565.

21. Ohanessian, G.; Brusich, M.; Goddard, W. A., III *J. Am. Chem. Soc.*, **1990**, *112*, 7179.

22. Ohanessian, G.; Goddard, W. A., III *Acc. Chem. Res.*, **1990**, *23*, 386.

23. (a) Perry, J. K.; Goddard, W. A., III; Ohanessian, G. *J. Chem. Phys.*, **1992**, *97*, 7560. (b) Perry, J. K., Ph. D. Thesis, California Institute of Technology, 1994.

24. Douglas, B.; McDaniel, D. H.; Alexander, J. J. *Concepts and Models of Inorganic Chemistry, Second Edition*, John Wiley and Sons, Inc.: New York, 1983, p. 220.

25. Yang, X. M.; Stern, C. L.; Marks, T. J. *Organometallics*, **1991**, *10*, 840.

26. Minsky, N, Ph. D. Thesis, Hebrew University, Jerusalem, 1969.

27. See for example (a) Beauchamp, A. L.; Cozak, D.; Mardhy, A. *Inorg. Chim. Acta*, **1984**, *92*, 191. (b) Erker, G.; Korek, U.; Petrenz, R.; Rheingold, A. L. *J. Orgaonmet. Chem.*, **1991**, *421*, 215. (c) Erker, G.; Korek, U.; Rheingold, A. L. *J. Organomet. Chem.*, **1993**, *454*, 113.

28. Woo, T. K.; Fan, L.; Ziegler, T. *Organometallics*, **1994**, *13*, 2252.

29. Yoshida, T.; Koga, N.; Morokuma, K. *Organometallics*, **1995**, *14*, 746.

30. Hunter, W. E.; Hrncir, D. C.; Bynum, R. V.; Penttila, R. A.; Atwood, J. L. *Organometallics*, **1983**, *2*, 750.

31. Ewen, J. A.; Elder, J. A. *Makromol. Chem., Macromol Symp.*, **1993**, *66*, 179.

32. Luinstra, G. A. Ph. D. Thesis, Rijksuniversiteit Groningen, 1991, p. 30.

33. (a) Clawson, L.; Soto, J.; Buchwald, S. L.; Steigerwald, M.; Grubbs, R. H. *J. Am. Chem. Soc.*, **1985**, *107*, 311. (d) Brintzinger, H. H., unpublished results.

34. (a) Bobrowicz, F. W.; Goddard, W. A., III *Methods of Electronic Structure Theory*, Schaefer, H. F., III, Ed.; Plenum Publishing Corp.: 1977. (b) Goddard, W. A., III; Ladner, R. C.; *J. Am. Chem. Soc.*, **1971**, *93*, 6750. (c) Ladner, R. C.; Goddard, W. A., III *J. Chem. Phys.*, **1969**, *51*, 1073. (d) Hunt, W. J.; Hay, P. J.; Goddard, W. A., III *J. Chem. Phys.*, **1972**, *57*, 738.

35. (a) Chong, D. P.; Langhoff, S. R. *J. Chem. Phys.*, **1986**, *84*, 5606. (b) Ahlrichs, R.; Scharf, P.; Ehrhardt, C. *J. Chem. Phys.*, **1984**, *82*, 890.

36. Davidson, E. R. *The World of Quantum Chemistry*, Daudel, R.; Pullman, B., Eds., Reidel: Dordrecht, 1974.

37. The GVB suite of programs, written at Caltech under the supervision of Goddard, W. A., III, *et al.*, Caltech, unpublished.

38. MOLECULE-SWEDEN is an electronic structure program system written by J. Almlöf, C. W. Baushlicher, M. R. A. Blomberg, D. P. Chong, A. Heiberg, S. R. Langhoff, P.-A. Malmqvist, A. P. Rendell, B. O. Roos, P. E. M. Siegbahn, and P. R. Taylor.

39. Murco N. Rignalda, Jean-Marc Langlois, Burnham H. Greeley, Robert B. Murphy, Thomas V. Russo, Christian Cortis, Richard P. Muller, Bryan Marten, Robert E. Donnelly, Jr., Daniel T. Mainz, Julie R. Wright, W. Thomas Pollard, Yixiang Cao, Youngdo Won, Gregory H. Miller, William A. Goddard, III, and Richard A. Friesner, PS-GVB v2.1, Schrödinger, Inc., 1994.

40. Mulliken, R. S. *J. Chem. Phys.*, **1955**, *23*, 1833.

41. (a) Melius, C. F.; Goddard, W. A., III *Phys. Rev. A.*, **1974**, *10*, 1528. (b) Redondo, A.; Goddard, W. A., III; McGill, T. C. *Phys. Rev. B.*, **1977**, *15*, 5038.

42. Rappé, A. K.; Smedley, T. A.; Goddard, W. A., III *J. Chem. Phys.*, **1981**, *85*, 1662.

43. Hay, P. J.; Wadt, W. R. *J. Chem. Phys.*, **1985**, *82*, 299.

44. Wadt, W. R. *J. Am. Chem. Soc.*, **1981**, *103*, 6053.

45. Rappé, A. K.; Goddard, W. A., III, *The FOURS Basis*, unpublished.

46. Hurley, M. M.; Pacios, L. F.; Christiansen, P. A.; Ross, R. B.; Ermler, W. C.; *J. Chem. Phys.*, **1986**, *84*, 6840.

47. For a good introduction to this topic, see Szabo, A.; Ostlund, N. S. *Modern Quanum Chemistry: Introduction to Advanced Electronic Structure Theory, Second Revised Edition*, Macmillan: New York, 1989.

48. Marsh, R. E.; Schaefer, W. P.; Coughlin, E. B.; Bercaw, J. E. *Acta Cryst.*, **1992**, *C48*, 1773.

49. Scholz, J.; Scholz, A.; Weimann, R.; Janiak, C.; Schumann, H. *Angew. Chem., Int. Ed. Engl*, **1994**, *33*, 1171.

50. Ewen, J. A.; Jones, R. L.; Razavi, A.; Ferrara, J. D. *J. Am. Chem. Soc.*, **1988**, *110*, 6255.

51. Sperlet, M. R., *et al. Acta Cryst.*, **1992**, *C48*, 2135.

Chapter III

Molecular Mechanics Investigations of Syndiospecific Zirconocene-Based Ziegler-Natta Catalysis

Abstract

Molecular mechanics simulations are described for zirconocene-based Ziegler-Natta catalysts. The origins of syndiospecificity are examined, studying the interactions directing the enantioface selectivity of the catalysts. These interactions are studied within the context of two possible selectivity mechanisms: chain end and enantiomorphic site control.

Particular attention is paid to studying the assumptions of the syndiospecific mechanism described in Chapter II (previously proposed by Ewen and co-workers). It is found that the syndiospecificity from catalysts of the type isopropyl(cyclopentadienyl)(1-fluorenyl)zirconium [^{i}Pr(CpFlu)Zr] results from a cooperation between site control and chain end control mechanisms. Other known catalysts are studied, including those that produce hemiisotactic polypropylene and those in which a chain control mechanism is operative. Qualitative arguments are given to understand the stereospecificity of each. Finally (cyclopentadienyl)(pentamethylcyclopentadienyl)zirconium (CpCp*Zr) is studied and found to have chain control and site control mechanisms operative in competing enantioselectivities.

Introduction

In Chapter II, electronic effects causing a pyramidal geometry for the group four metallocenium catalysts were discussed that provide a rationale for the migratory insertion syndiopolymerization mechanism. Much experimental work can be explained by this formally enantiomorphic site control model. While this geometric assumption implicit in the mechanism has been proven (Chapter II), the other assumption, namely the absolute enantioface selectivity required, has not yet been fully proven.

In addition, recent experimental evidence[1] shows that achiral catalysts* can produce polymers with respectable tacticities. In the case of propylene polymerization, the bis (pentamethylcyclopentadienyl)metal dichloride [$Cp^*_2MCl_2$, M = Zr, Hf] catalyst precursor will produce mildly syndiotactic polymer, while bis(cyclopentadienyl)metal dichloride [Cp_2MCl_2] produces slightly isotactic polymer. Changing the monomer to 1-butene improves the tacticity considerable, although the stereodirecting nature of these catalysts is still not as effective as the C_s or C_2 symmetric catalysts. However, simple steric arguments based on monomer-ligand repulsions that have successfully explained the stereodirecting ability of the C_s and C_2 symmetric catalysts are unable to account for the stereodirecting nature of these catalysts. Obviously, more subtle steric interactions are occurring between the chain and the ligands.

It has been reasonably well established that the ligand environment provides the majority of the control for stereodirecting catalysts, either iso- or syndiodirecting. Although the majority of the stereochemistry is dictated by the ligands, there may be some chain control occurring, either with or against the site control. Erker[2] has been studying this problem using unlinked isodirecting catalysts. However, few studies using linked

---

*While the isopropyl(cyclopentadienyl-1-fluorenyl) based catalysts are also achiral, polymer motion introduces chirality at the metal center. With these achiral catalysts, no such chirality can be introduced.

ligands have been directed at this problem: how much of the control occurs via the site, and how much via the chain.

It is also of interest to understand how the chain/ligand interaction affects the absolute enantioselectivity of the catalyst. It is accepted that the α-olefin complexes and inserts such that the olefin pendant and polymer are transoid to each other, in order to minimize repulsions between them. With such an arrangement, it is relatively straightforward to understand isospecific polymerization: the polymer occupies an empty quadrant (I) within the ligand environment (Figure 1a) and a transoid monomer complexation naturally directs the pendant group to the other empty quadrant (III) (Figure 1b). Thus, the chain and ligand environment work in a cooperative manner to direct the enantioselectivity.

Figure 1. Most Favored Positions for (a) Polymer and (b) Polymer and Monomer for Bis(Indenyl)Metal Catalysts

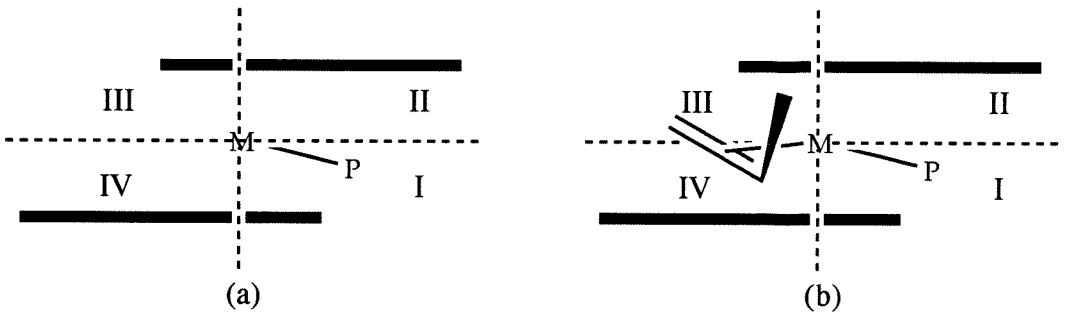

With syndiospecific catalysts, a transoid monomer-polymer orientation results in bad steric contacts between either the polymer and the ligand or the monomer and the ligand. It is not obvious which is favored. Ewen, *et al.*,[3] used molecular models and suggested that it is most important to relieve the chain-ligand steric stress. Other groups have performed molecular mechanics calculations with varying results: calculations by Corradini and Guerra[4] suggest that the chain adopts the least sterically crowded position, forcing the monomer to complex with the monomer methyl group directed toward the fluorenyl group. However, their calculations are incomplete, as they do not include a chiral

β-carbon (their "polymer" is an isobutyl group). Calculations by Fierro, *et al.*,[5] suggest that there is no absolute enantioface selectivity for a given metal orientation, which is necessary for the migratory insertion mechanism; instead, they find chain control is the operative mechanism, although they do not discuss this result in depth.

If it is the case that the chain adopts the least sterically crowded conformation, and that this conformation and the ligand environment choose a particular enantioface, then the chain is playing a larger role in the stereodirecting nature of the catalyst than is currently thought. Thus, while the pyramidal geometric assumption of migratory insertion has been validated for group four metal cations (see Chapter II), it is still necessary to assess the steric interactions in these catalysts. To this end, molecular mechanics simulations were conducted.

Stereochemical Notation

A brief discussion of the stereochemical notation used in this chapter will be given here. For a prochiral olefin, there are two non-superimposable faces, *re* and *si*. As defined by Hanson,[6] the two faces of propene are:

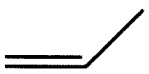

re

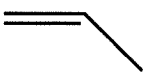

si

The chirality (*R* or *S*) at tetracoordinate carbons is defined by the standard Cahn-Ingold-Prelog rules.[7] This notation has been extended to tetracoordinate metals,[8] where the hapticity of the ligand defines the precedence in otherwise ambiguous situations. Thus, the precedence for isopropyl(cyclopentadienyl-1-fluorenyl)zirconium(ethyl)(ethylene) [^{i}Pr(CpFlu)Zr(C_2H_5)(C_2H_4)] is as marked:

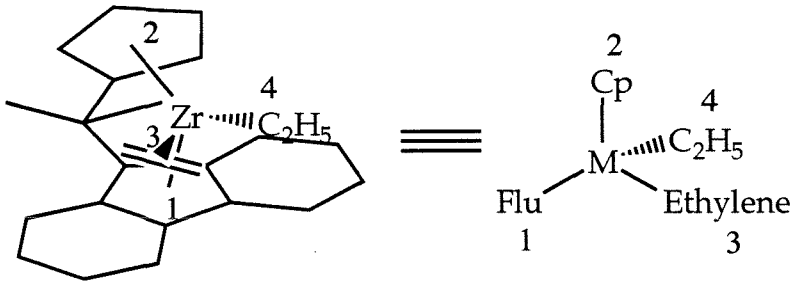

giving an *R* metal orientation. In addition, substituting linked metallocenes can also introduce a chirality at the bridgehead carbon on the ring. In this case, the stereochemical notation follows that introduced by Schlögl,[9] in which the ring carbons are considered as each bound to the metal, giving tetracoordinate carbons. In this case, the notation follows the standard Cahn-Ingold-Prelog rules, giving for the two stereoisomers of isopropyl(3-methyl-1-cyclopentadienyl-1-fluorenyl)zirconium dichloride [^{i}Pr(CpMeFlu)$ZrCl_2$] with precedence and absolute configuration as marked (the chiral carbon is denoted with a *):

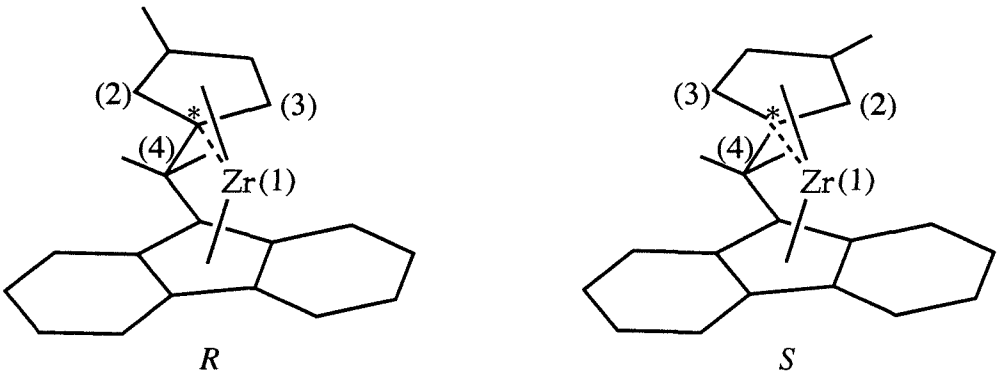

Isotactic chains are defined as chains in which each chiral carbon has the same absolute configuration, leading to meso (*m*) dyads (pairs of chiral carbons). Syndiotactic chains are characterized by racemic (*r*) dyads.

Previous Molecular Mechanics Investigations

Molecular mechanics simulations have been used to understand the enantioselectivity of the homogeneous and heterogeneous catalysts. Guerra, Corradini, and coworkers[10] have used rigid catalysts and conformational searches of torsion angles to

study heterogeneous,[11] isodirecting homogeneous,[12] and syndiodirecting homogeneous[13] catalysts. Using simple models, they are able to account for much of the observed stereochemistry. In the case of the chiral, isodirecting homogeneous catalysts, they find that a single enantioface is preferred; in the case of the C_s syndiodirecting catalysts, they find that each of the two metal orientations (*R* or *S*) prefer a different enantioface. However, there are three possible flaws with their calculations: the ligand environment is assumed to be rigid, the force field employed is relatively primitive, and, particularly in the case of the syndiodirecting catalyst, they did not study the effect of β-carbon chirality on the enantioface selectivity.

Using the MM2 force field, Yu, Chien and coworkers have studied both isospecific homogeneous[14] and syndiospecific homogeneous[5] propylene polymerization, using apparently rigid catalyst environments. It is not obvious that this force field is necessarily a correct one to use in these circumstances. In the case of the isospecific polymerization, they conclude that enantioface selectivity errors are rare, and that the observed errors can be accounted for by three processes: 1) chain exchange between two catalysts of different absolute configurations, 2) catalytic site isomerization, and 3) chain isomerization at the metal center. This final process has also been proposed by Busico, *et al.*[15] and Leclerc and Brintzinger;[16] the other two processes are novel and unlikely. In the case of the syndiospecific polymerization, they find that a chain control mechanism, and not an enantiomorphic site control mechanism, is responsible for the observed enantioface selectivities.

Kawamura-Kuribayashi, Koga, and Morokuma[17] performed a mixed *ab initio*, molecular mechanics investigation of isodirecting and syndiodirecting homogeneous catalysts. With a rigid catalyst framework derived from *ab initio* calculations, they used the MM2 force field to determine the steric interactions driving the enantioface selectivity of the catalysts. They conclude that the site control is *indirect*, in that the site influences the

polymer conformation, which in turn expresses the enantioface selectivity of the catalyst. Their calculations show that the two different metal orientations (*R* and *S*) each prefer a different stereoface, thus agreeing with the work of Guerra, Corradini, and coworkers.[13]

Rappé and coworkers have performed the most rigorous molecular mechanics calculations on the isodirecting[18] and syndiodirecting[18a] homogeneous catalysts, imposing no geometric constraints on the catalysts, and by using force fields developed for these catalyst systems. They propose specific substitutions on the ligand environment to improve the enantioface selectivity of the catalysts. However, their calculations improperly predict that the syndiodirecting catalyst will actually be *isodirecting*.

Developing Force Fields

Force field simulations, which approximate a molecule as nuclei related by specific forces, have been used with tremendous success for molecules containing main group elements. These atoms lend themselves well to these simulations, as they have well defined states and corresponding valencies that are general for a large collection of molecules. Simulations involving transition metals have been less successful, as transition metals have more accessible states for bonding, a larger variety of orbitals involved in bonding (s, p, and d vs. just s and p for the main group elements), and more flexible valencies. This greater flexibility leads to the richer chemistry of the transition metals, but also leads to greater difficulty in modeling transition metal complexes.

For the complexes of interest, molecular mechanics should provide a reasonable model. In these early metal complexes, the important bonding states are reasonably well separated, and the geometries associated with these states are well defined. In addition, the majority of the interactions of interest are between the ligands, the polymer chain, and the monomer, which, as they contain exclusively carbon and hydrogen, are well described by standard force fields. Recent successes in describing the geometries of early metal

complexes[18,19] give further confidence to using molecular mechanics to describe the complexes of interest.

Recently, Rappé and Goddard[20] have developed a general force field (the "Universal Force Field" or UFF) for the entire periodic table. In this force field, actually a set of rules, the parameters are derived based on simple relationships: the element, its hybridization, and its connectivity. The energy for this force field can be written as:

$$E = E_R + E_\theta + E_\phi + E_\omega + E_{VdW} + E_{el} \quad (1)$$

where the component parts are the bond stretch, angle bend, dihedral angle torsion, inversion, non-bonded, and electrostatic terms respectively; there are no cross-terms (such as bond stretch-angle bend interactions). The UFF does a good job predicting the structures of the catalyst precursors of interest; however the predicted vibrational spectrum is incorrect for the Zr-Cl and Zr-C bonds (see Table 1). Thus, the UFF will be used as a starting point and will be modified such that the geometries and vibrational spectra of saturated metallocenes are consistent with experimental results. The development of the force field will be described here, and the parameters are listed in the appendix.

A force field was recently developed for zirconium and hafnium catalyst precursors (dichloro species) by Doman, Hollis, and Bosnich.[19] It is an empirical force field using experimental geometries and vibrational frequencies of metallocene dichloride species. This is a conceptually simpler force field than the UFF, in that only bond, angle, torsion, and Van der Waals terms are included. However, geometries of substituted metallocene derivatives are well reproduced, giving confidence that it is possible to model these catalysts and catalyst precursors.

It is desired to ultimately describe the 14-electron cationic catalysts, which are unsaturated. The problem is made difficult by the lack of experimental data: these complexes cannot be isolated. Thus, a first step to developing the force field for the unsaturated complexes is developing a force field for the saturated catalyst precursors.

Two complexes were used to fit the necessary force field terms: Cp_2ZrCl_2 and $Cp_2Zr(CH_3)_2$, as there are structural[21] and vibrational[22,19] data available for both. Table 2 contains the calculated and experimental data, and the appendix contains the details of the derived force field. To test the applicability of this empirical force field, two other structures were tested: the syndiodirecting catalyst precursor ^{i}Pr(CpFlu)$ZrCl_2$ and substituted ethylene bis(3-methyl-1-indenyl)zirconium dichloride precursor that is aspecific. The good match for both can be seen in Figure 2 and Figure 3.

Table 1. Comparison between Calculated (UFF) and Experimental Data, Cp_2ZrCl_2, $Cp_2Zr(CH_3)_2$

	Cp_2ZrCl_2		$Cp_2Zr(CH_3)_2$	
Parameter	Calculated	Experimental[b]	Calculated	Experimental[c]
R(Cp-Zr)	2.17	2.19	2.17	2.23
R(Zr-Y)	2.50	2.46	2.31	2.28
θ(Cp-Zr-Cp)	129.5	133.3[d] or 126.0[e]	128.5	132.5
θ(Cp-Zr-Y)	106.5		107.1	105.5
θ(Y-Zr-Y)	98.8	97.8	94.7	95.1
ν(Zr-Y)	449	332, 356, 360	583, 622, 645	462
ν(Zr-Cp)[f]	250, 305, 351	260, 270, 290	248, 265	288, 212
ν(Cp-Zr-Cp)	247, 318	123, 175		
ν(Y-Zr-Y)	124, 174	158, 185		
ν(Y-Zr-Cp)	460	144		

[a]Distances in Å, angles in degrees, frequencies in cm^{-1}. Y is Cl for Cp_2ZrCl_2 and C for $Cp_2Zr(CH_3)_2$
[b]Structural data from reference 21a, vibrational data from reference 22a, based on Raman spectra
[c]Structural data from reference 21b and 21c. Stretching frequencies from reference 22a, based on IR and Raman spectra, bending frequencies from 22d, based on IR and Raman spectra.
[d]Reference 22b
[e]Reference 22c
[f]As there was extensive mixing in the computed Cp-Zr modes, leading to difficulty in assigning a Cp-Zr stretching mode, Cp tilt modes were used instead to compare with experimental values.

The force fields developed for the saturated systems were used to describe the unsaturated systems with one modification. While the electronic effect causing an inversion barrier is most important for retention of the metal chirality following an insertion, it may also be indirectly involved in the enantioselectivity of the ligand environment. Thus, this potential was incorporated into the force field by modifying the

appropriate parameters so that the *ab initio* inversion potential calculated for $Cp_2Zr(CH_3)^+$ (see Chapter II) was described properly for a similarly fixed metallocene environment.

It is important to determine what is the "appropriate" parameter to modify in the procedure described above. There are two possibilities: the Cp_CZrC angle term (where Cp_C is the ring centroid) or the inversion term defined by the four centers Zr, C, Cp_C, Cp_C. To determine which is the appropriate parameter, force constants for the bond stretch and angle bending terms of Cl_2ZrH^+ were calculated at the Hartree-Fock level, using a geometry that has the M-H bond 20° out of the plane. Using these force constants and the calculated geometric parameters, the geometries and energetics of the inversion motion were calculated. A barrier of 10.774 kcal/mol, with minima at 68°, was calculated using this simple force field, compared to the *ab initio* value of 9.13 kcal/mol. Thus, according to these model systems, it is necessary to modify only the Cp_CZrC angle term.

Table 2. Comparison between Calculated (Force Field from This work) and Experimental Data, Cp_2ZrCl_2, $Cp_2Zr(CH_3)_2$

	Cp_2ZrCl_2		$Cp_2Zr(CH_3)_2$	
Parameter	Calculated	Experimental[b]	Calculated	Experimental[c]
R(Cp-Zr)	2.23	2.19	2.24	2.23
R(Zr-Y)	2.48	2.46	2.29	2.28
θ(Cp-Zr-Cp)	125.1	133.3[d] or 126.0[e]	126.48	132.5
θ(Cp-Zr-Y)	107.39		108.59	105.5
θ(Y-Zr-Y)	97.7	97.8	90.39	95.1
ν(Zr-Y)	335, 339	332, 356, 360	456, 459	462
ν(Zr-Cp)[f]	218	260, 270, 290	217, 255, 273	288, 212
ν(Cp-Zr-Cp)	107, 138, 153	123, 175	199	
ν(Y-Zr-Y)	180, 191	158, 185		
ν(Y-Zr-Cp)	169	144	273, 305	

[a]Distances in Å, angles in degrees, frequencies in cm^{-1}. Y is Cl for Cp_2ZrCl_2 and C for $Cp_2Zr(CH_3)_2$
[b]Structural data from reference 21a, vibrational data from reference 22a, based on Raman spectra
[c]Structural data from reference 21b and 21c. Stretching frequencies from reference 22a, based on IR and Raman spectra, bending frequencies from 22d, based on IR and Raman spectra.
[d]Reference 22b
[e]Reference 22c
[f]As there was extensive mixing in the computed Cp-Zr modes, leading to difficulty in assigning a Cp-Zr stretching mode, Cp tilt modes were used instead to compare with experimental values.

Figure 2. Isopropyl(Cyclopentadienyl-1-Fluorenyl)Zirconocene Dichloride: Experimental (Black) and Calculated (Gray) Structures

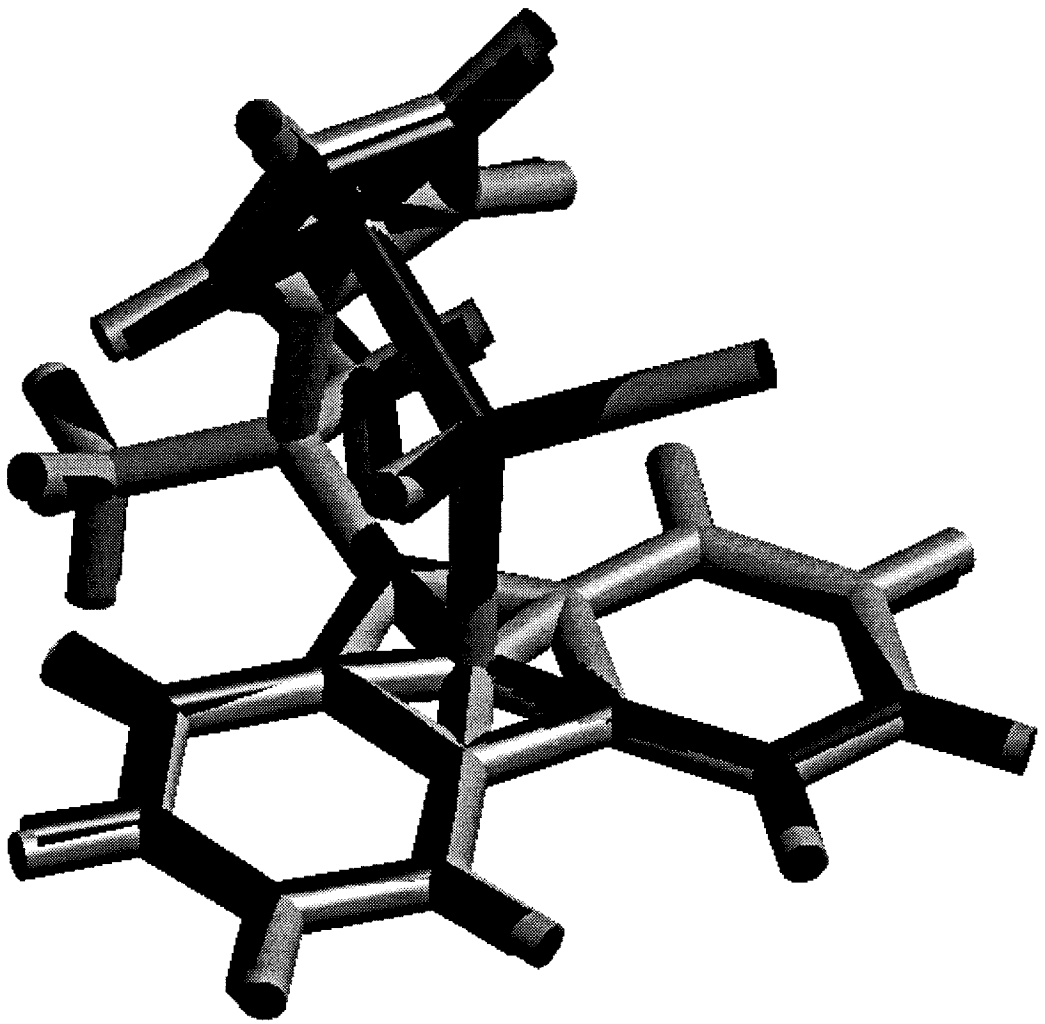

Figure 3. Ethylene Bis(3-Methyl-1-Indenyl)Zirconium Dichloride: Experimental (Black) and Calculated (Gray) Structures

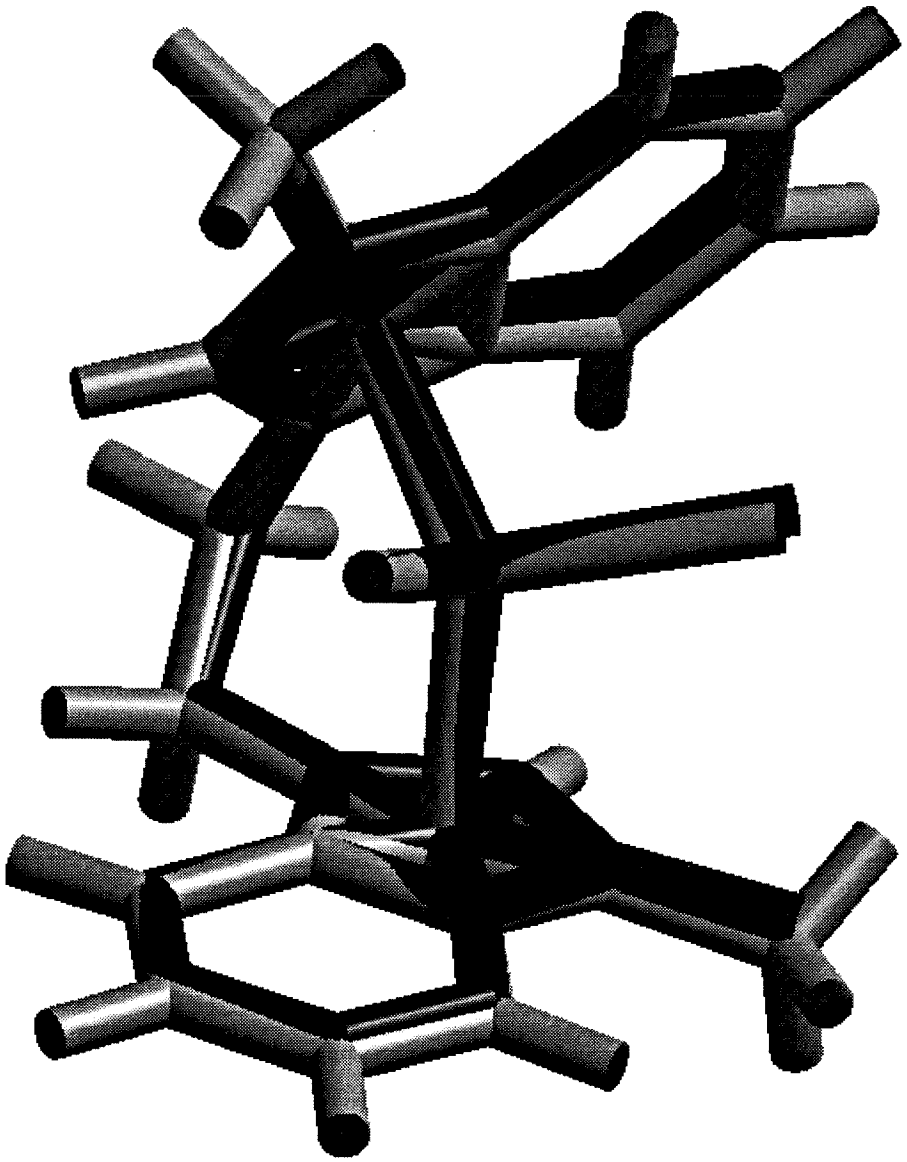

M-Cp interactions

An important interaction in these complexes is between the metal and the cyclopentadienyl (Cp). This interaction is handled[23] through the use of a dummy atom (CpR) located at the center-of-mass of the Cp (the ring centroid); this dummy atom is bound to the five carbons of the Cp ring as well as the metal. The interactions between this CpR atom and the other atoms to which it is bonded are described explicitly within the

force field. However, in the actual calculations the forces on the CpR atom are distributed to the ring carbons, giving the proper 3N-6 (N is the number of true atoms) vibrational frequencies

M-Olefin Binding

It is necessary to include Zr-olefin parameters to describe the metal-olefin binding in the catalyst system. As the metal olefin binding is qualitatively similar to the metal cyclopentadienyl binding, a center-of-mass construct was also used to describe this binding. However, there is no experimental data from zirconocene complexes for use in these systems. Two sources of data were used: experimental geometries from niobocene alkyl olefin complexes[24] and the *ab initio* structural data for both dichloro zirconium[18a] and zirconocene[17] systems. In all cases, an alkyl-Zr-olefin centroid angle of about 90° was observed, so that this geometric parameter was used with an angle force constant of 100 kcal/mol. The metal-olefin centroid distance varied from 2.175 Å for the niobocene complex to 2.458 Å for the dichloro zirconium systems to 2.859 Å for the zirconocene complexes. The niobium-olefin distance was discarded as being a poor description for these systems, as there is evidence of strong metal to ligand back-bonding in these systems (the olefin C-C bond distance is 1.431, compared to 1.34 for free olefin) which would not be present in the zirconocenium catalysts. A value of 2.50 was chosen as a reasonable Zr-olefin distance, and the parameters were chosen to reproduce this result for the zirconocenium-methyl-ethylene system. Finally, C-Zr-olefin torsional parameters were chosen to maintain a planar Zr-C-C-C configuration.

General Considerations

The enantioface selectivity will be dictated by the steric forces acting on the monomer upon bonding to the metal and inserting into the metal carbon bond. It is assumed that there will not be a qualitative difference between the steric forces felt upon

complexation and upon insertion, so that the system can be well modeled by the olefin complex. The systems used include the metallocene catalyst, propylene, and an oligomer containing two propylene groups terminated by an ethyl group (Figure 4); the two chiral carbons (β and δ) have a racemic relationship to each other, thus modeling a syndiotactic chain. In all cases, The chain was assumed to have a nearly trans backbone; deviations from such an arrangement were tested and found to be higher in energy.

Figure 4 Oligomer Used for Simulations (a) *R*-β-Carbon (b) *S*-β-Carbon

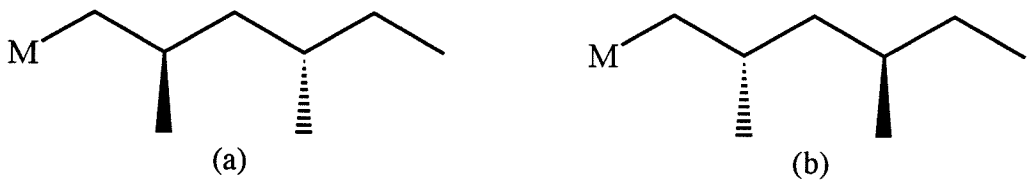

(a) (b)

There are two important dihedral angles that determine the orientation of the polymer within the ligand environment: the $CpZrC_\alpha C_\beta$ and the $ZrC_\alpha C_\beta C_\gamma$. Exhaustive searches of the dihedral space described by these two angles were used to determine the most favorable polymer conformation. Once the most favored conformation was found, a full minimization of the catalyst structure was performed. All calculations were performed using Caltech modified modules of Molecular Simulation, Inc. (MSI) Polygraf/Biograf moldules, version 330, MSI, Burlington, MA.

Results and Discussion

Isopropyl(cyclopentadienyl-1-fluorenyl) ^{i}Pr(CpFlu)Zr System

The first system studied is the classic syndiodirecting catalyst system: ^{i}Pr(CpFlu)Zr (polymer)(propylene). There are three chiral centers (olefin, metal, and beta carbon), giving a total of 8 stereoisomers, four of which are unique diastereomers. The four diastereomers that have a metal *R* chirality were studied.

The results are summarized in Table 3. Note that for both β-carbon orientations, the *re* stereoface of the propylene is preferred over the *si* stereoface by 4-5 kcal/mol. In all four cases, the polymer adopts the conformation proposed by Ewen[3] and Corradini and Guerra[4] (

Figure 5) in which it occupies the less sterically crowded quadrant (III) for an *R* metal. The favored monomer orientation places the pendant group transoid to the polymer (quadrant IV). Thus for this metal orientation (*R*), the *re* face is favored.

Table 3. Energetics for Different Propylene, Polymer Diastereomers

Metal Chirality	β-Carbon Chirality	propylene face	incipient dyad	FF Energy (kcal/mol)	Rel. Energy (kcal/mol)
R	*R*	*re*	*r*	251.023	0.000
R	*R*	*si*	*m*	256.403	5.380
R	*S*	*re*	*m*	256.609	5.586
R	*S*	*si*	*r*	260.534	9.511

Figure 5. Preferred (a) Polymer Conformation and (b) Monomer Orientation for *R* Metal

However, it is also interesting to note that there is a relatively large enantioselectivity based on the chirality of the β-carbon. This selectivity can be understood by considering Figure 6, in which the polymer is drawn in the most favored conformation (as shown in Figure 5). The most favored rotamer around the C_α C_β bond directs the β-H towards the Cp ring. The two disfavored rotamers for the *S* orientation are shown in Figure 6(a) and (b) and for the *R* orientation in (d) and (e). Thus, with this preferred H-

position, the two different β-C orientations are shown in Figure 6(c) and (f). It can be seen that the remaining polymer chain can either be directed back towards the ligand system (Figure 6(c), β-*S* orientation, disfavored) or away from the ligand system (Figure 6(f), β-*R* orientation, favored).

Figure 6. Rotamers About C_α C_β Bond for (a-c) *S*-β-Carbon and (d-f) *R*-β-Carbon (for *R*-^{i}Pr(CpFlu)Zr Catalyst)

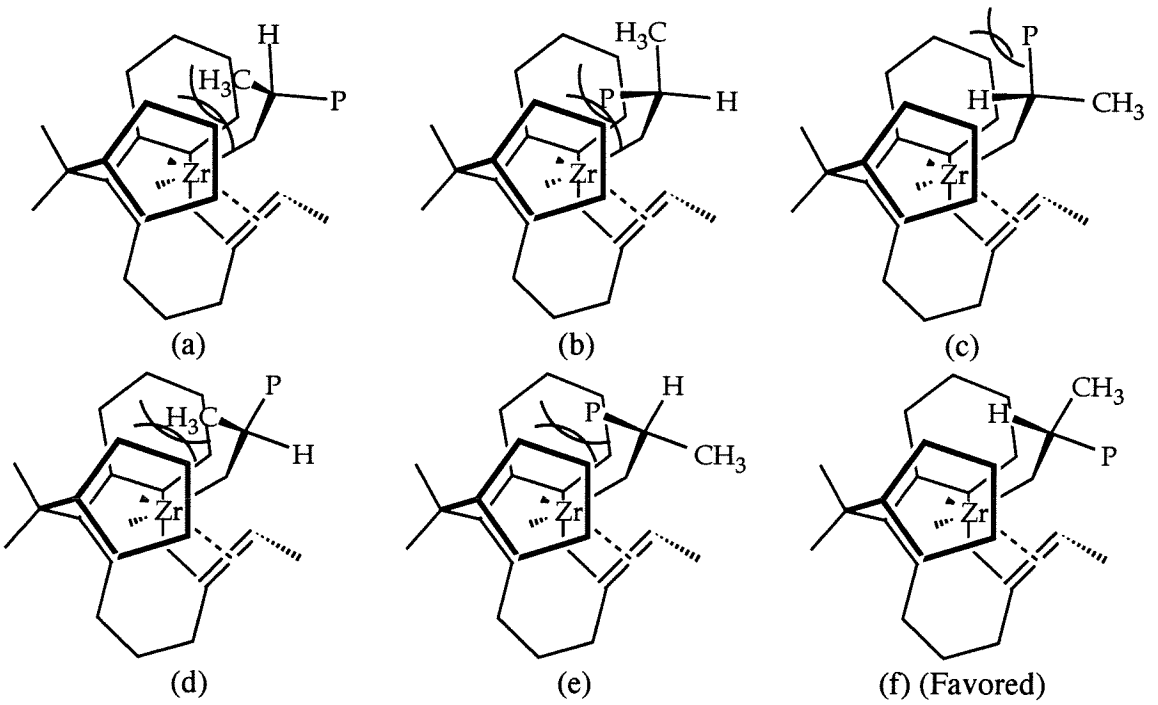

Thus, it is found that two effects combine to produce the observed syndiotactic polypropylene: the migratory insertion-site control and the control by chain. The enantioface selectivity of the metal site is calculated to be 4-5 kcal/mol. Such an enantioselectivity is consistent with the migratory insertion control of the stereochemistry of the insertion. In addition, there is a 5 kcal/mol preference based on the chirality of the β-carbon, consistent with chain control.

A test was performed to determine the influence of the β-methyl substituent on the enantioselectivity, by replacing the β-methyl with a hydrogen. In this case, the *re* face

selectivity is reduced 4-5 kcal/mol to 0.3173 kcal/mol, a dramatic change. The main reason for this large change is that the polymer can adapt a conformation in which it is directed towards the fluorenyl ligand, allowing the *si* face a less hindered approach (Figure 7). If the polymer is in the same conformation as shown in Figure 7(a) (directed towards the Cp), the *re* face is favored by 3.68 kcal/mol.

Figure 7. Monomer-Polymer Conformation with Achiral β-Carbon (a) *re* Face (b) *si* Face

(a) (b)

Conformations in which the polymer chain is directed at the fluorenyl ligand (as in Figure 7(b)) were tested for the syndiotactic chain (results listed above) and the *si* monomer face. In the case of the *S*-β-carbon, the polymer directed toward the fluorenyl is only 0.6 kcal/mol lower than when directed toward the Cp; in the case of the *R*-β-carbon, it is about 3.3 kcal/mol higher in energy when directed toward the fluorenyl.

Thus, it is found that the β-methyl plays two important roles in the selectivity of the syndiodirecting catalyst. First, it causes the polymer to prefer a conformation in which it is directed toward the Cp ligand, which in turn causes an enantioface preference for the *re* face of the monomer (for an *R* metal chirality), regardless of the chirality of the β-carbon. This enantioface selectivity is a necessary component of the chain migratory insertion mechanism to explain the observed syndioselectivity of the catalysts. A second role for the β-methyl is that it serves, via the carbon chirality, as a double stereo-differentiation agent.

Cp_2Zr and Cp^*_2Zr

Recent experiments by Resconi, Abis, and Franciscono[1] with the achiral catalysts Cp_2Zr and Cp^*_2Zr show that at low temperatures both are capable of producing mildly stereoregular polypropylene. In the case of the Cp* catalyst the polymer is syndiotactic, and in the case of Cp the polymer is isotactic. The mechanism of stereocontrol must be via the chain end. It is puzzling why methylating the rings would cause a change in the enantioface selectivity, and such inversion is not accounted for by Resconi, Abis, and Franciscono.

The obvious difference in steric bulk forces different polymer conformations in the two catalysts. In the case of Cp*, the enormous bulk of the methyls forces the polymer to have the least contact with the catalyst, forcing it to be nearly planar within the catalyst wedge (Figure 8). The monomer will approach such that minimal steric contact is made with the β-methyl, so that the pendant group is transoid to the β-methyl. In the case shown for the *R*-carbon, the *re* enantioface is calculated to be preferred by 0.79 kcal/mol. The magnitude of this preference is qualitatively consistent with the results from the more syndiodirecting ^{i}Pr(CpFlu) ligand. In that case, the experimental racemic dyad excess (rde) is about 90%,[3] and the calculated enantioface selectivity is of the order of 5 kcal/mol. In the case of Cp*, the rde is about 17%,[1] with a calculated selectivity of 0.8 kcal/mol.

For the case of Cp_2Zr, the calculated enantioface selectivity is 0.21 kcal/mol for the incipient *syndiotactic* insertion. In this case the stereocenter is quite removed from the metal center. As is shown in Figure 9, the most favorable chain conformation has the polymer pointing away from the monomer, and at the β-carbon the hydrogen is directed back towards the Cp's. The monomer adopts an orientation such that the pendant group is transoid to the polymer, although the preference is weak. It is possible that in this case the assumption that the enantioface selectivity of the monomer coordination is qualitatively the same as the enantioface selectivity of the insertion may be wrong, as in the olefin binding

the stereocenter is sufficiently distant from the metal center to exert only a very weak enantioselectivity. In the transition state the chain may come in closer contact with the ligand environment, modifying the selectivity of the insertion. It is also likely that the counterion plays a large role in determining the enantioface selectivity, especially in light of the small energetics involved.

Figure 8. Enantioselectivity of Cp^*_2Zr (a) Favored and (b) Disfavored Monomer Approach

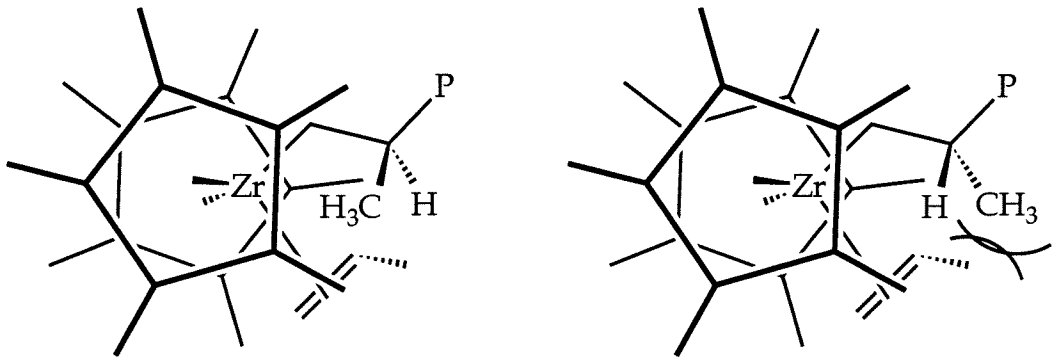

Figure 9. Preferred Chain Conformation and Enantioselectivity for Cp_2Zr (β-*R*, *re* Face)

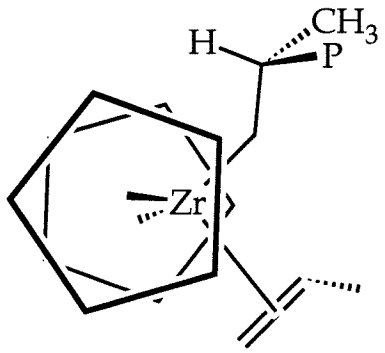

Isopropyl(3-methyl-1-cyclopentadienyl-1-fluorenyl) ^{i}Pr(CpMeFlu) Zr System

The methyl substitution on the cyclopentadienyl ring introduces a fourth chiral element into the molecule and dramatically changes the polypropylene produced by this catalyst compared to the simpler ^{i}Pr(CpFlu) system. In this case, the resulting

polypropylene (hemiisotactic) has an alternating regular-irregular arrangement of the methyls along the polymer backbone (Figure 10).[3,25] The odd numbered carbons have the same relative configuration (isotactic), while the even numbered carbons have a random arrangement. In a perfect hemiisotactic chain, relative stereochemistries occur in pairs: (rr)(mm)(mm)(rr)(mm)(rr)(rr), etc., with a net 0% excess of *m* over *r* dyads.

Figure 10. Hemiisotactic Polypropylene

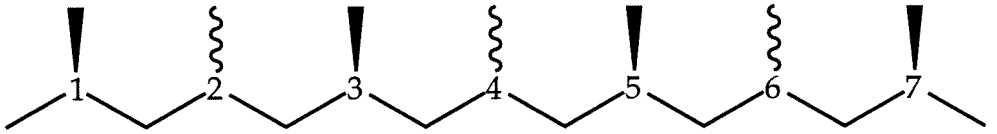

Including the propylene, there are 16 possible enantiomers, 8 of which are unique diastereomers. The eight possibilities, and their energies, are listed in Table 4.

Table 4. Energetics for Propylene, Catalyst diastereomers, *S*-^{i}Pr(CpMe)FluZr System

Metal Chirality	β-Carbon Chirality	enantioface	Incipient tacticity	FF Energy (kcal/mol)	Relative Energy (kcal/mol)
R	*R*	*re*	*syndio*	230.538	2.788
R	*R*	*si*	*iso*	234.626	6.876
R	*S*	*re*	*iso*	237.284	9.534
R	*S*	*si*	*syndio*	238.976	11.226
S	*R*	*re*	*syndio*	234.810	7.060
S	*R*	*si*	*iso*	229.071	1.321
S	*S*	*re*	*iso*	234.036	6.286
S	*S*	*si*	*syndio*	227.750	0.000

For the *S*-ligand system (Figure 11(a)), the *R* metal environment has the polymer residing on the more sterically hindered side of the catalyst (Figure 11(b)); the *S* metal environment has the polymer residing in the less sterically hindered area (Figure 11(c)). All further discussion will be with respect to this *S*-ligand system. The mechanism proposed by Ewen, *et al.*[3,25] to account for the polymer produced invokes the migratory insertion mechanism. According to them, when the metal is in an *R* configuration (more sterically crowded environment), the catalyst displays no enantioface selectivity, giving an insertion of random chirality (even carbons in Figure 10); when the metal is in an *S*

configuration, the catalyst has a preference for the *si* stereoface (based on the enantioselectivity of the ^{i}Pr(CpFlu) catalyst).

Figure 11. (a) *S*-^{i}Pr(CpMeFlu)Zr System with (b) *R*-Metal Orientation and (c) *S*-Metal Orientation

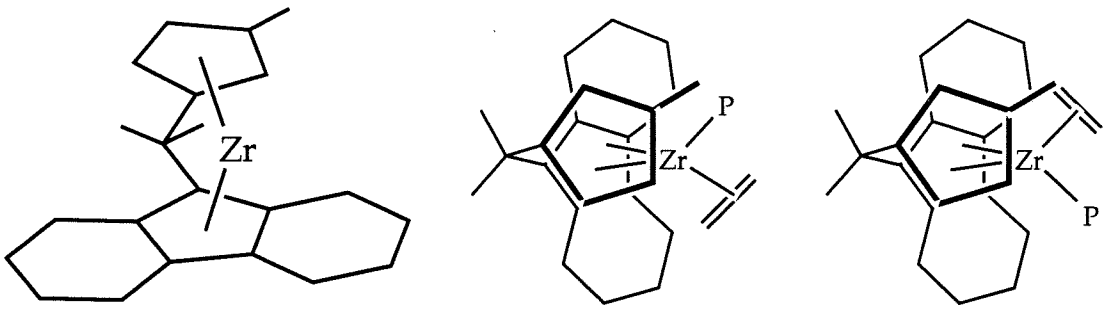

(a) (b) (c)

Considering first the *S*-metal configuration, the *si* stereoface is preferred over the *re* stereoface by about 6 kcal/mol. This represents a slight increase (1 kcal/mol) in the enantioface selectivity with respect to the syndiodirecting catalyst ^{i}Pr(CpFlu)Zr. In addition, the enantioselectivity based on the chain chirality has decreased to about 1 kcal/mol. Thus, the major stereoselectivity occurs via the site, with little chain control. These results are consistent with the mechanism proposed by Ewen, *et al.*

Consider now the *R*-metal. Given that the preferred enantioface for an *S*-metal is *si*, following the insertion the chain will migrate to give an *R*-metal orientation and an *R*-β-carbon. Examining Table 4, it is found from the calculations that, for the *R*-β carbon arrangement, the *re* face is preferred by about 4.2 kcal/mol. This preference is smaller than that expressed by the syndiodirecting catalyst, but it is larger than anticipated given the tacticity of the polymer. The hemiisodirecting catalysts, depending on the co-catalyst, appear to show a preference for *m* or *r* dyads: when the co-catalyst is methylalumoxane (MAO), the catalyst shows a preference for *r* dyads, giving a 10% *r* dyad excess, and when the co-catalyst is $B(C_6F_5)_4^-$, the catalyst shows a preference for *m* dyads, giving a 10% *m* dyad excess.[3] Given the results above, an excess of *r* dyads (greater than 10%) would be expected in all cases.

It is worthwhile checking to see if a chain control mechanism is possible given the calculated data. For the *S* orientation of the β-carbon, the enantioface selectivity strongly favors the *si* face , by about 6 kcal/mol. Thus, the insertion following an *S*-β-carbon will always give an *R*-β-carbon (*r* dyad). However, for the *R*-β orientation, the *si* face is favored by only about 1.5 kcal/mol. The insertion following an *R* carbon will likely give an *m* dyad, but the preference is much weaker. Following this line of reasoning, pentad[†] sequences expected by this model would be:

mmrr, mmmr, rmrr, mmmm, rmmr, rrrr, rrrm, and mrrm

All of these are expected by the migratory insertion mechanism except the rmrr pentad. All pentads of the type xmrx (rmrr, rmrm, and mmrm) are forbidden by the migratory insertion mechanism, although they are observed in small amounts; the chain control mechanism accounts for their existence. However, analyzing the relative pentad frequencies predicted by this mechanism clearly shows that it is inconsistent with experimental data. The chain control mechanism would expect the two pentads rrrr and rrrm to account for over 50% of the observed pentads, while experimentally they account for only 20-25% of the observed pentads.[3]

CpCp*Zr

This is an interesting catalyst as it affords the possibility of an unlinked, syndiodirecting ligand environment. Given that the bis(cyclopentadienyl) and bis(pentamethylcyclopentadienyl) systems were able to produce polymers of mild stereoregularities at low temperatures, it is possible that this system would also be able to produce mildly syndiotactic polypropylene. The data for the *R*-metal arrangement is shown in Table 5.

[†]A pentad contains 5 adjacent chiral carbons and is designated by the stereochemistry of the

Table 5. Energetics for Polymer, Monomer Diastereomers, *R*-metal Configuration

β-Carbon Chirality	propylene face	incipient tacticity	FF Energy (kcal/mol)	Rel. Energy (kcal/mol)
R	*re*	*syndio*	267.328	0.436
R	*si*	*iso*	266.892	0.000
S	*re*	*iso*	268.211	1.319
S	*si*	*syndio*	267.430	0.538

As for the case of the ^{i}Pr(CpFlu)Zr catalyst, it is found that an *R*-metal exhibits an enantioface selectivity. In this case, the *si* face is favored by at least 0.44 kcal/mol. Note, however, that the preferred insertion, with respect to the β-carbon, gives an isotactic insertion; in the case of ^{i}Pr(CpFlu) the preferred insertion gives a syndiotactic insertion relative to the β-carbon. Thus, the two forms of stereoselectivity are competing: the site model, with the chain migration, exhibits an enantioselectivity based on the metal chirality, which for the *R*-metal orientation is the *si* face and for the *S*-metal orientation is the *re* face, giving syndiotactic polypropylene. The β-carbon, however, exhibits a preference leading to isotactic polypropylene.

Examining the polymer and monomer conformations can assist in understanding this phenomenon. The polymer will adapt conformations similar to those in the Cp_2Zr system, in which the chain is directed away from the incoming monomer (Figure 12). Due to the bulky Cp* ligand, one β-carbon configuration will be preferred, that which has the polymer directed away from the Cp* (for an *R*-metal this is the *R*-carbon) (Figure 12(a) vs. (b)). The preferred monomer face is that which directs the methyl away from the Cp* (for an *R*-metal this is the *si* face) (Figure 12(c) vs. (d)).

---

dyads comprising the pentad.

Figure 12. Polymer Conformations for CpCp*Zr (a) *R*-Carbon (b) *S*-Carbon and Monomer Faces (c) *re* (d) *si*

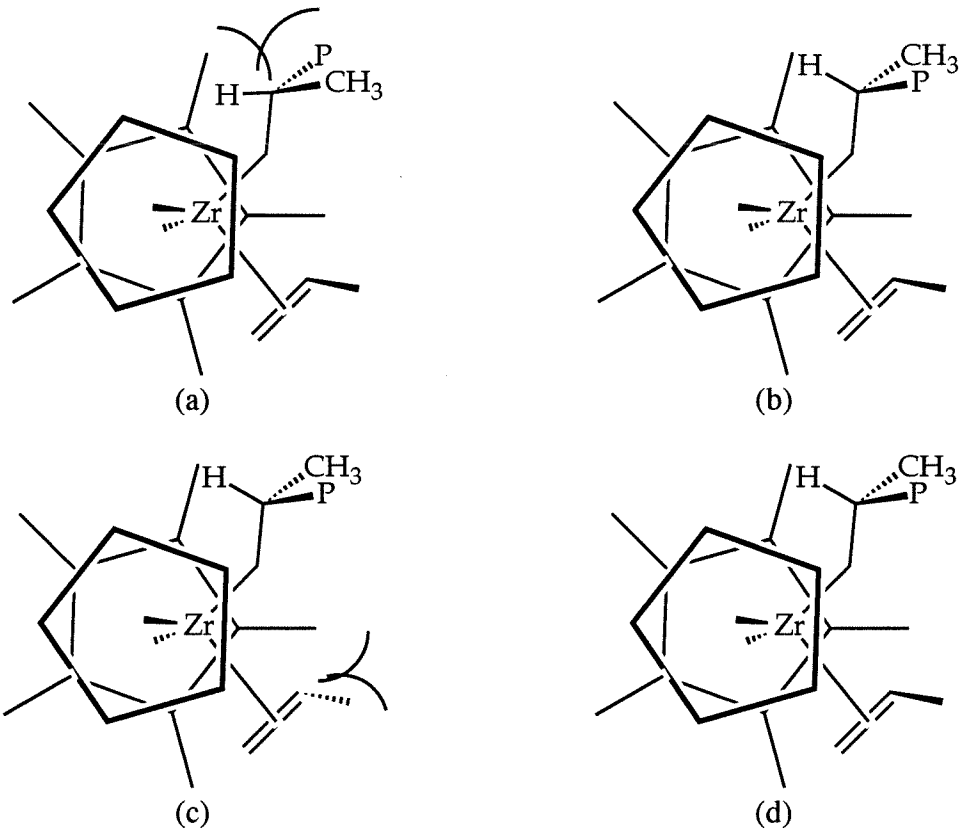

A dimethylsilyl linked analog for this catalyst system has been studied by Ewen and coworkers;[3] they find that this silyl linked system is weakly syndiodirecting at 60° C in the polymerization of propylene (14% rrrr pentads, 2% mmmm pentads by NMR analysis), in qualitative agreement with the results presented above. However, preliminary results of the linked system (with an isopropyl group rather than a dimethylsilyl group) show that the polymer adopts a different conformation in the linked system. The unlinked system has a large (about 130°) Cp-Zr-Cp* angle, which allows the polymer to adopt the conformations shown in Figure 12. Linking the two Cp groups reduces the Cp-Zr-Cp* angle to about 125°, increasing the steric congestion in the rear of the system. In this case the polymer adopts conformations qualitatively similar to those shown in Figure 5 and Figure 6. Thus, in the linked system the chain and site control would be expected to operate to favor the

same insertion, as they do in the ^{i}Pr(CpFlu)Zr catalyst. In the unlinked system, the two mechanisms operate to favor different insertions.

Thus, a system has been found in which the two effects, chain end control and enantiomorphic site control (via the migratory insertion-enantioface selectivity), are competing rather than working together, as for the ^{i}Pr(CpFlu)Zr. This would be an interesting system to study, to gauge the relative importance of the two effects. Given the energetics listed in Table 5, the effects are likely too small for propylene. In their studies of Cp^*_2Zr, Resconi, Abis, and Franciscono[1] find that using 1-butene rather than propylene results in polymers of very respectable syndiotacticities, having an r dyad excess of up to 64% at low temperatures. Thus, polymerization of 1-butene with this catalyst system would be of interest.

Appendix: Force Field Description

Force field descriptions approximate the energy of a molecule as a sum of the different terms describing the interactions within the molecule. The Universal Force Field (UFF) was used as a basis for the derived force filed used for this study. The interactions included in the description are bond stretches, angle bends, dihedral angle torsions, inversions, van der Waals interactions, and electrostatic interactions, so that the energy can be written:

$$E = E_R + E_\theta + E_\phi + E_\omega + E_{VdW} + E_{el} \qquad (2)$$

Using this energy expression, structural optimizations are straightforward. Standard gradient techniques are used to perform these minimizations. In addition, vibrational data are also straightforward to obtain, via the second derivative matrix for the above expression. A brief description of each term will be given, along with the derived parameters. Note that no inversion terms were included beyond those in the UFF. The force constant for the inversion defined by Zr, C, CpR, CpR was set to 0, as this inversion was included via the CpR-Zr-C angle term.

Bond Terms

The UFF was used as the basis for the force fields developed for this study. The most important terms are those involving the metal; consequently, the most care was taken to derive these terms. The bond stretch and angle bend force constants and equilibrium values were chosen to reproduce experimental stretching frequencies and crystal structure values. The values are shown in Table 6. The functional form used is a simple harmonic:

$$E = \frac{1}{2}\kappa\left(r - r_e\right)^2 \tag{3}$$

where κ is the force constant and r_e is the equilibrium distance.

Table 6. Force Constants and Equilibrium Parameters for Bond Terms

Bond*	κ (kcal/mol • Å^{-2})	r_e(Å)
Zr–Cl	200.0	2.40
Zr–C_3	200.0	2.24
Zr–Cp	600.0	2.15
Zr–olefin	600.0	2.40
Cp-C_R	300.0	1.1733

*C_R and C3 are Biograf representations for resonant and sp^3 carbons respectively

Angle Terms

As for the bond terms, the angle terms were chosen to reproduce experimental geometries and frequencies, when available. The data is listed in Table 7; the functional form used is a harmonic cosine expansion:

$$E = \frac{1}{2}\kappa\left(\cos(\theta) - \cos(\theta_e)\right)^2 \tag{4}$$

where κ is the force constant and θ_e is the equilibrium angle.

Table 7. Force Constants and Equilibrium Parameters for Angle Terms

Angle*	κ (kcal/mol)	θ_e(degrees)
Cl-Zr-Cl	63.2227	109.4710
Cp-Zr-Cl	67.9317	109.4710
Cp-Zr-Cp	50.0	125.00
C_3-Zr-C_3	80.0	109.4710
Cp-Zr-C_3	48.5022	105.00†
Cp-Zr-C_3	48.5022	95.00‡
Cp-C_R-C_3	10.0	180.0
C_R-C3-C_R	100.0	100.0
olefin-Zr-C_3	100.0	90.0
Zr-olefin-C_2	100.0	90.0
C_2-C_2-C_3	100.0	120.0
Cp-C_R-H	100.0	180.0
C_R-Cp-X	10.0	90.0
Cp-C_R-C_R	0.0	54.0
C_R-Cp-C_R	0.0	72.0

*C_R, C_2, and C_3 are Biograf representations for resonant, sp^2 and sp^3 carbons, respectively; X is a representation for any atom in that position.
†Angle derived for neutral complexes
‡Angle derived for cationic complexes

Torsion Terms

The torsional energy expression is given by a Fourier expansion:

$$\sum_n v_n \cos(n\theta) \tag{5}$$

where v_n is the barrier for the n-fold dihedral torsion. The parameters are listed in Table 8.

Table 8. Torsional Parameters

Dihedral*	v_0	v_1	v_2	v_3	v_4
C3-Zr-olefin-C2	40.0	0.0	–40.0	0.0	0.0
Zr-olefin-C2-H	10.0	0.0	0.0	0.0	–10.0
Zr-olefin-C2-C3	10.0	0.0	0.0	0.0	–10.0

*C2 and C3 are Biograf representations for sp^2 and sp^3 carbons, respectively.

Van der Waals Terms

For the organic parts of the molecule, the Van der Waals terms were taken from the Dreiding force field,[26] and are shown in Table 9. For zirconium, the Van der Waals terms

from UFF were used, as there are no Dreiding parameters for Zr. Two different functional forms were used, an exponential-6 (exp-6) was used in conjunction with the Dreiding parameters:

$$D_e\left\{\left[\left(\frac{6}{\zeta-6}\right)e^{\zeta\left(1-\frac{R}{R_e}\right)}\right]-\left[\left(\frac{\zeta}{\zeta-6}\right)\left(\frac{R_e}{R}\right)^6\right]\right\} \tag{6}$$

and the Lennard-Jones 6-12 (L-J 6-12) was used in conjunction with the UFF parameter:

$$D_e\left\{\left[\frac{R_e}{R}\right]^{12}-2\left[\frac{R_e}{R}\right]^6\right\} \tag{7}$$

where in both cases R_e is the equilibrium bond distance and D_e is the well depth. For the exponential-6 form, an exponential scaling term (ζ) is also necessary.

Table 9. Van der Waals Terms

Atom	R_e (Å)	D_e (kcal/mol)	ζ	form
Zr	3.124	0.0690	—	L-J 6-12
H	3.195	0.0152	12.382	exp-6
C	3.983	0.1467	14.034	exp-6
Cl	3.95	0.283	13.861	exp-6

Electrostatic Terms

This contribution to the energy is given by the expression:

$$E = \sum_{\text{all pairs } ij} \frac{q_i q_j}{r_{ij}} \tag{8}$$

where the interaction between all atom pairs separated by more than two bonds are included in the energy expression.

The UFF has been designed to use charges calculated by the Charge Equilibration algorithm[27] for determining charges. It was decided that the charges generated from this method are not reasonable representations for the actual charges on the system; for Cp_2ZrCl_2, the charges calculated for each of the five components of the molecule (2Cp, Zr and 2Cl) are: Zr +0.66, Cl –0.52, Cp +0.20. The charge equilibration method was

designed for classical situations and fails in properly describing the electronegativity of the cyclopentadienyl ring; in addition, the metal charges are underestimated, compared to quantum chemical metal charges (of the order +1.2). Thus, another method that has given reliable charges was used: performing electrostatic-potential fits (with charges centered at the nuclei) to Hartree-Fock wave-functions.[28,29] Using this method, the charges of Cp_2ZrCl_2 are Zr +1.27, Cl –0.46, Cp –0.175, which are more reasonable given the nature of the structure.

These atom centered charges were calculated for smaller systems using the electrostatic-potential fits, and used to determine the charges of the basic components of the system (Cp, Zr, Cl, CH_3). Thus, charges were determined for the system $Cp_2Zr(CH_3)^+$ and divided to compute the component charges: Zr +1.57, Cp –0.075, and CH_3 –0.98. It is assumed that for larger systems (such as $Cp^*_2Zr(CH_3)^+$) the components retain the same charge, and that the charge equilibration algorithm is valid for each component. Thus, for $Cp^*_2Zr(CH_3)^+$, the charges for Cp* were determined by using the charge equilibration algorithm (with a total Cp* charge of –0.075) to give the following charges: C_{ring} +0.03, C_{methyl} –0.41, H +0.12. For linked ligands (for example ^{i}Pr(CpFlu)), the atomic charges were computed using a total ligand charge of twice that of an individual Cp, giving a total charge of –0.15 for the cationic systems.

References

1. Resconi, L.; Abis, L.; Franciscono, G. *Macromolecules*, **1992**, *25*, 6814.
2. See for example Erker, G.; Psiorz, C.; Krüger, C.; Nolte, M. *Chem. Ber.*, **1994**, *127*, 1551. See also reference 49 from Chapter I.
3. Ewen, J. A.; Elder, M. J.; Jones, R. L.; Haspeslagh, L.; Atwood, J. L.; Bott, S. G.; Robinson, K. *Makromol. Chem., Macromol. Symp.*, **1991**, *48/49*, 253.
4. Corradini, P.; Guerra, G. *Prog. Polym. Sci.*, **1991**, *16*, 239.
5. Fierro, R.; Yu, Z.; Rausch, M. D.; Dong, S.; Alvares, D.; Chien, J. C. W. *J. Poly. Sci. A, Polym. Chem.*, **1994**, *32*, 661.
6. Hanson, K. R. *J. Am. Chem. Soc.*, **1966**, *88*, 2731.
7. Cahn, R. S.; Ingold, C.; Prelog, V. *Angew. Chem., Int. Ed. Engl.*, **1966**, *5*, 394.
8. Stanley, K.; Baird, M. C. *J. Am. Chem. Soc.*, **1975**, *97*, 6598.
9. Schlögl, K. *Topics in Stereochemistry, Vol. 1*, Allinger, N. L., Eliel, E. L., Eds., Interscience: New York, 1967, 39.
10. For a summary of their work, see Corradini, P.; Guerra, G. *Prog. Polym. Sci.*, **1991**, *16*, 239.
11. Guerra, G.; Cavallo, L.; Venditta, V.; Vacatello, M.; Corradini, P. *Makromol. Chem., Macromol. Symp.*, **1993**, *69*, 237., and references therein.
12. (a) Corradini, P.; Guerra, G.; Vacatello, M.; Villani, V. *Gaz. Chim. Ital.*, **1988**, *118*, 173. (b) Venditto, V.; Guerra, G.; Corradini, P.; Fusco, R. *Polymer*, **1990**, *31*, 530.
13. Cavallo, L.; Guerra, G.; Vacatello, M.; Corradini, P. *Macromolecules*, **1991**, *24*, 1784.
14. Yu, Z.; Chien, J. C. W. *J. Polym. Sci., A. Polym. Chem.*, **1995**, *33*, 125.
15. (a) Busico, V. *Abstr. Int. Symp. Stereosel. Polym.*, **1994**, 73. (b) Busico, V.; Cipullo, R. *J. Am. Chem. Soc.*, **1994**, *116*, 9329.
16. Leclerc, M.; Brintzinger, H. H. *J. Am. Chem. Soc.*, **1995**, *117*, 1651.

17. Kawamura-Kuribayashi, H.; Koga, N.; Morokuma, K. *J. Am. Chem. Soc.* ,**1992**, *114*, 8687.

18. (a) Castonguay, L. A.; Rappé, A. K. *J. Am. Chem. Soc.*, **1992**, *114*, 5832. (b) Hart, J. R.; Rappé, A. K. *J. Am. Chem. Soc.*, **1993**, *115*, 6159.

19. Doman, T. N.; Hollis, T. K.; Bosnich, B. *J. Am. Chem. Soc.*, **1995**, *117*, 1352.

20. Rappé, A. K.; Casewit, C. J.; Colwell, K. S.; Goddard, W. A., III; Skiff, W. M. *J. Am. Chem. Soc.*, **1992**, *114*, 10024.

21. (a) Hunter, W. E.; Hrncir, D. C.; Bynum, R. V.; Pentilla, R. A.; Atwood, J. A. *Organometallics*, **1983**, *3*, 750. (b) Prout, K..; Cameron, T. S.; Forder, R. A.; Critchley, S. R.; Denton, B.; Rees, G. V. *Acta Cryst.*, **1974**, *B30*, 2290. (c) in *Comprehensive Organometallic Chemistry, volume 3*, Wilkinson, G., Ed., p 570.

22. (a) Samuel, E.; Ferner, R.; Bigorgne, M. *Inorg. Chem.*, **1973**, *12*, 881. (b) Druce, P. M.; Kingston, B. M.; Lappert, M. F.; Spalding, T. R.; Srivastava, R. C. *J. Chem. Soc. (A)*, **1969**, 2106. (c) Maslowsky, E.; Nakamoto, K. *Appl. Spectr.*, **1971**, *25*, 187. (d) Balducci, G.; Bencievenni, L.; DeRosa, G.; Gigli, R.; Martini, B.; Nunziante Cesaro, S. *J. Mol. Struct.*, **1980**, *64*, 163.

23. Goddard, W. A., III, unpublished results.

24. Burger, B. J.; Santarsiero, B. D.; Trimmer, M. S.; Bercaw, J. E. *J. Am. Chem. Soc.*, **1988**, *110*, 3134.

25. Ewen, J. A.; Elder, M. J.; Harlan, C. J.; Jones, R. L.; Atwood, J. L.; Bott, S. G.; Robinson, K. *ACS-Polymer Preprints*, **1991**, *32*, 469.

26. Mayo, S. L.; Olafson, B. D.; Goddard, W. A., III *J. Phys. Chem.*, **1990**, *94*, 8897.

27. Rappé, A. K.; Goddard, W. A., III *J. Phys. Chem.*, **1991**, *95*, 3358.

28. (a) Chirlian, L. E.; Francl, M. M. *J. Comp. Chem.*, **1987**, *8*, 894. (b) Woods, R. J.; Khalil, M.; Pell, W.; Moffat, S. H.; Smith, V. H., Jr. *J. Comp. Chem.*, **1990**, *11*, 297. (c) Breneman, C. M.; Wiber, K. B. *J. Comp. Chem.*, **1990**, *11*, 361.

29. Murco N. Ringnalda, Jean-Marc Langlois, Burnham H. Greeley, Robert B. Murphy, Thomas V. Russo, Christian Cortis, Richard P. Muller, Bryan Marten, Robert E. Donnelly, Jr., Daniel T. Mainz, Julie R. Wright, W. Thomas Pollard, Yixian Cao,

Youngdo Won, Gregory H. Miller, William A. Goddard, III, and Richard A. Friesner, PS-GVB v2.1, Schrödinger, Inc., 1994.

Chapter IV

Conclusions of the Computational Studies

Abstract

A brief summary of the results from Chapters II and III is presented within the context of the syndiodirecting mechanism. General rules are proposed for guiding the synthesis of syndiodirecting ligands, and experiments are proposed to test the ideas described.

Introduction

As has been stated earlier, the mechanism for syndiodirecting α-olefin polymerization is still an unsettled question. The exact nature of the alternating enantioface selectivity for these catalysts is still unclear. Analysis of the insertion errors reveals errors suggestive of both site and chain control. An attractive mechanism was proposed by Ewen, *et al.*[1] that states the enantioselectivity is due entirely to the site, and that the alternating nature of the enantioselectivity is due to a chain migration following every insertion.

This mechanism is controversial, as there has been no apparent reason for the chain migration. Previous evidence for the mechanism consists of: (1) the dominant errors are of a double type (see Chapter I) according to Ewen, *et al.*,[1] strongly suggesting site control; and (2) the existence of hemiisotactic-directing catalysts that are very similar in structure to the syndiodirecting catalysts. These hemiisodirecting catalysts have a single methyl substitution, filling one of the two open quadrants of the syndiodirecting catalysts (see Chapter I). With the migratory insertion mechanism of stereocontrol, it is very simple to understand the production of hemiisotactic polymer: one side of the catalyst is aspecific, while the other side of the catalyst is enatioselective, and the chain alternates between these two, forcing alternating specific and aspecific insertions.

Besides the migratory insertion, one other assumption of the Ewen, *et al.*, mechanism is that the chain adapts a conformation that is the least sterically stressful, forcing the monomer to approach with a more sterically hindered path. Such conformations have support in the molecular mechanics calculations of Guerra, Corradini, and co-workers,[2] who find that the most favored polymer conformation is indeed the one envisioned by Ewen, *et al.* However, neither group has addressed the issue of how the chirality of the β-carbon on the chain affects the proposed mechanism.

Summary of Results

A brief summary of the results from the proceeding two chapters is presented. The most striking result from Chapter II is the difference between the group three and group four transition metal structures. Due to their metal electronic ground state, the group four cationic structures have a predisposition to the non-planar geometries assumed by Ewen, *et al.*[1] for their syndiodirecting mechanism, whereas it is found that the group three structures have a bias for planar structures. It is also found that the metal thorium has the correct electronic structure to cause pyramidal structures for thorocene-based catalysts. Among the group four metals, it is found that the bias towards planarity (based on $Cp_2M(CH_3)^+$ calculations) is as follows $Ti^+ > Th^+ > Zr^+ > Hf^+$. Within the group three metals, it is found that La, while preferring planar structures, requires essentially no energy for out-of-plan motions.

It is also found that the steric congestion within the wedge modifies the non-planar bias for the group four metals. As the Cp-M-Cp angle is reduced, the non-planar bias for the systems increases.

Examining the steric forces exerted by the ligand environments, it is found that the nature of the enantioface selectivity is two-fold for the catalyst system isopropyl(cyclopentadienyl)(1-fluorenyl)zirconium (^{i}Pr(CpFlu)Zr): both the chirality of metal environment (when the polymer is in a non-planar position) and the chirality of the β-carbon conspire to select one enantioface. These two directing forces are computed to be of equal selectivity. However, given the calculated results for the hemiisodirecting catalyst system isopropyl(3-methyl-cyclopentadienyl)(1-fluorenyl)zirconium, in which the chain control is also calculated to be strong (in apparent contrast to the experimental results), it appears likely that the stereocontrol exerted by the chain is overestimated in these calculations: the chain control exists, but is small. Thus, the majority of the enantioface selectivity comes from the site.

According to these results, first a series of rules for catalyst design are proposed and second a series of catalysts are proposed.

Rules for Design of Effective Syndiodirecting Catalyst

1. Zr and Th should be the most effective metals. Hf exhibits the least electronic bias, whereas Ti exhibits the greatest. However, Ti is also the smallest atom, leading to greater steric crowding in the Ti^+ metallocene systems, reducing the non-planar bias.

2. Lanthanum has the greatest electronic bias of the group three for making a syndiodirecting catalyst.

3. Use the smallest linking groups between the two Cp-like ligands, to reduce the Cp-M-Cp angle.

Proposed Catalysts

1. ^{i}Pr(CpFlu)Th should be an effective syndiodirecting catalyst. The electronic bias, coupled with the more open wedge (due to longer Th-Cp distances) should make this a good syndiospecific catalyst. Due to the larger size of Th, it will show a reduced steric congestion in the reactant area, thus possibly allowing the polymerization of olefins substituted at the three, as well as four, position on the monomer.

2. ^{i}Pr(CpFlu)La: of the group three metals, this would be expected to show the greatest possibility for syndiodirecting polymerization. As with thorium, sterically demanding monomers are possible.

3. CpCp*Zr and CpCp*Y polymerizing 1-butene: These two systems, with identical ligand environments, are expected to show different enantioselectivites. The CpCp*Zr is expected to produce a polymer that is somewhat syndiotactic (has an excess of racemic dyads), whereas the CpCp*Y is expected to produce a polymer that is somewhat isotactic (has an excess of meso dyads). As is seen for related systems,[3] monomers larger than propylene will be necessary to produce polymers with respectable dyad excesses,

either racemic or meso. These two catalysts would represent the first example of a ligand environment that produces different polymers on different metals.

References

1. Ewen, J. A.; Elder, M.; Jones, R.; Haspeslagh, L.; Atwood, J.; Bott, S.; Robinson, K. *Makromol. Chem., Macromol. Symp.*, **1991**, *48/49*, 253.

2. See for example Corradini, P.; Guerra, G. *Prog. Polym. Sci.*, **1991**, *16*, 239.

3. Resconi, L.; Abis, L.; Franciscono, G. *Macromolecules*, **1992**, *25*, 6814.

Part 2:

Concurrent Resonance Calculations

Chapter V

Introduction and Description of Program

Abstract

A brief discussion of molecular orbital, valence bond and Generalized Valence Bond electronic structure methods are presented to provide context for a discussion of computational resonance theory. This resonance theory is developed in a manner such that the inherent parallel structure of the algorithm is discovered. This parallel structure will be exploited in the following chapters for the development of concurrent algorithms.

A general outline of the program design features and architecture follows the resonance discussion. These features are included to give the program as great a flexibility as possible. Three novel elements that will be discussed at length are the use of the C++ programming language, the use of the Tcl command language, and the mixing of these two languages to produce "Tcl Enabled Objects."

Introduction

Over the years, most chemists develop a familiarity with the valency concept of chemical bonding in which each two-electron bond is localized between atoms. The great success of this concept has been its predictive power for structure and reactivity. However, as Pauling,[1] Slater,[2] and Hückel[3] first discovered, there are certain classes of molecules for which the valency concept breaks down. In these cases, no single valence structure adequately describes the molecule. The classic example of this valence bond model breakdown is benzene (C_6H_6). Although the valence bond model suggests a cyclohexatriene structure, benzene exhibits unusual stability and reactivity for such a structure. In addition, the crystal structure shows that each C-C bond has the same length, midway between single and double bond lengths (1.40 Å); a cyclohexatriene-like structure would be expected to have alternating short (1.33 Å) and long bonds (1.54 Å).

To remedy this failure, a resonance between valence bond structures is invoked:

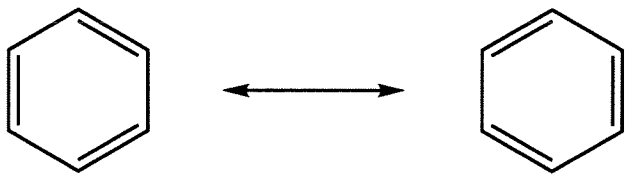

Such a description allows one to continue using the valence bond language and concepts for bonding, with the understanding that the extra stability comes from a quantum mechanical superposition of valence structures. Within this framework, the total molecular wave-function is written (ignoring normalization):

$$\Psi = c_A \Psi_A + c_B \Psi_B \tag{1}$$

where the left valence structure is represented by Ψ_A and the right valence structure is represented by Ψ_B. Because benzene is symmetric, the two coefficients are equal. Again ignoring normalization, the energy of this system is given by the expression:

$$E_{AB} = \frac{\left\langle \Psi^A + \Psi^B \middle| \hat{\mathbf{H}} \middle| \Psi^A + \Psi^B \right\rangle}{\left\langle \Psi^A + \Psi^B \middle| \Psi^A + \Psi^B \right\rangle} = \frac{H_{AA} + H_{BB} + 2H_{AB}}{2 + 2S_{AB}} = \frac{H_{AA} + H_{AB}}{1 + S_{AB}} \tag{2}$$

because H_{AA} and H_{BB} are equal. In the above expression $\langle \Psi_A | \hat{H} | \Psi_B \rangle = H_{AB}$ is called the resonance matrix element and $S_{AB} = \langle \Psi^A | \Psi^B \rangle$ is the overlap matrix element.

An alternate framework with which to describe benzene is the delocalized molecular orbital approach pioneered by Hückel. Using this approach, Hückel derived his well known aromaticity rule for π-electrons: if the number of electrons within the π-framework of the molecule is 4n+2, where n is a whole number, the molecule is formally aromatic. Both approaches have their strengths, and are mathematically quite similar. However, because the language of valence is so important and useful in chemistry, resonance is quite important.

Although resonance has found great utility within organic chemistry, its utility can be generalized to any situation in which a single valence structure is inadequate to describe the system. For example, to describe the charge transfer (either hole or electron transfer) in conjugated dienes Ψ_A and Ψ_B:

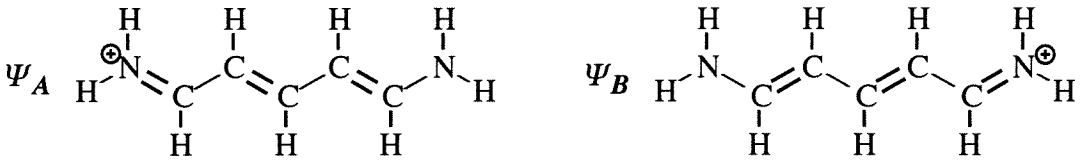

it is necessary to compute cross-matrix elements, H_{AB}, where each molecular orbital of Ψ_A overlaps some or all orbitals of Ψ_B. In this case the electron (or hole) transfer rate is proportional to $|T_{AB}|^2$, where:

$$T_{AB} = \frac{H_{AB} - S_{AB}H_{AA}}{1 - S_{AB}^2} \tag{3}$$

Generalizing further, it is possible to use the concept of resonance to describe systems in which more than two valence structures are necessary to describe a molecule.

One such example is the cyclopentadienyl anion (which has six π electrons, and thus meets the Hückel aromaticity criterion); it is formally a resonance between five valence structures:

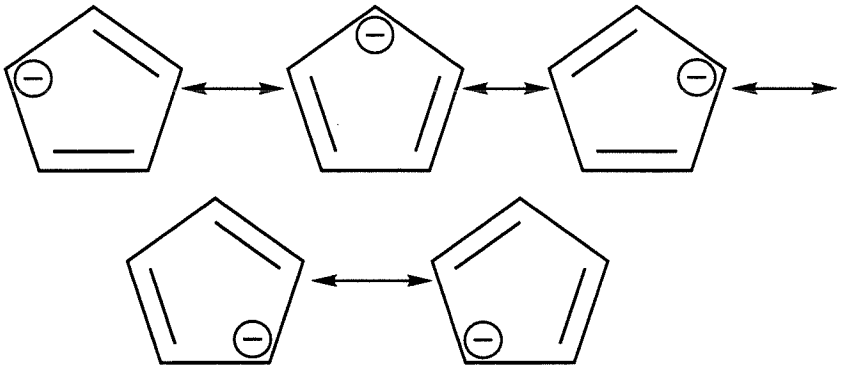

Such multi-state resonance descriptions are conceptually approaching a non-orthogonal configuration interaction (CI) wave-function. In this case, typically more than two valence structures (configurations) are used to describe the electronic structure of the molecule.

Although non-orthogonal CI's have been successfully computed in the past,[4] their computational complexity has limited their utility. Because of the Pauli Principle, each wave-function must be antisymmetrized:

$$\Psi^A = \sum_n (-1)^{P_n} \wp_n \left(\phi_i \phi_j \cdots \phi_N\right) \tag{4}$$

where N is the number of occupied orbitals, $\wp_n$ is an operator that generates the n^{th} permutation, and P_n is the number of interchanges necessary to obtain this permutation. There are N! permutations. Computing the two-electron contribution to H_{AB} involves calculating elements of the form:

$$E_{2e} = \sum_{ij} \left\langle \phi_i \phi_j \left| \frac{1}{r_{ij}} \right| \phi_i \phi_j \right\rangle \sum_m \sum_n (-1)^{P_m} (-1)^{P_n} \wp_m \left(\phi_k \phi_l \cdots \phi_N\right) \wp_n \left(\phi_k \phi_l \cdots \phi_N\right) \tag{5}$$

If the orbitals are orthogonal, there is only one permutation of the remaining orbitals for each wave-function that gives a non-zero value, leading to computational dependency of N^2 operations. On the other hand, if every orbital in Ψ_A can overlap every orbital in Ψ_B, every permutation of the remaining orbitals in (5) is non-zero, leading to a computational

dependency of $(N!)^2$. However, if they can be made practical, non-orthogonal CI approaches have two distinct advantages over orthogonal CIs:

1) the component states Ψ_A and Ψ_B can be chosen to be chemically meaningful descriptions of the system; thus, the interpretation of the results is more straightforward than an orthogonal CI
2) this "better" choice of basis states reduces the number of states needed to accurately describe the system

Electronic reorganization problems such as electron transfer and interpretation of photoelectric spectra lead naturally to a few-state description in terms of non-orthogonal basis states.

To simplify this computational problem, Voter and Goddard[5] showed that a pair of unitary transformations exist that (a) leave the total energy, E_{AB}, unchanged* and (b) reduce the computational effort to order N^2. These unitary transformations, when applied to Ψ_A and Ψ_B, transform the wave-functions such that each orbital of Ψ_A overlaps exactly one orbital of Ψ_B and is orthogonal to all others. This *biorthogonalization* procedure makes the resonance calculation tractable.

Despite the computational savings obtained with clever transformations such as biorthogonalization, many systems of interest, particularly for non-orthogonal CI's and electron transfer studies, remain too large for practical H_{AB} calculations with existing computer codes; in addition, multi-state resonance calculations, as with the cyclopentadienyl anion, are not handled gracefully by existing programs.[6] Improvements are necessary to study such systems. Most importantly, the underlying parallel structure of the theory has not been examined. Such an examination will be undertaken in order to take advantage of concurrent computation.

---

*Unitary transformations amongst occupied orbitals for closed shell wave-functions always leave the energy unchanged.

Background Theory

A brief review of valence bond, molecular orbital (Hartree-Fock), and Generalized Valence Bond theory will be presented to facilitate the discussion of the resonance method. Valence bond theory has been tremendously powerful for understanding chemistry. However, strict valence bond (VB) theory is computationally expensive, due to the non-orthogonality of the orbitals. The valence bond wave-function for the hydrogen molecule is written as:

$$\Psi^{VB} = A\left[(l(1)r(2) + r(1)l(2))\alpha\beta\right] \tag{6}$$

where A is the antisymmetrizer operator, l and r are the hydrogen 1s orbitals on the left and right centers respectively, and the indices (1) and (2) refer to the first and second electrons. The two s-orbitals have a finite overlap: they are non-orthogonal, retaining their localized, atomic character. In contrast, the molecular orbital (MO) wave-function for hydrogen is:

$$\Psi^{MO} = A\left[((l+r)(1)(l+r)(2))\alpha\beta\right] \tag{7}$$

The MO treatment results in delocalized orbitals. However, expanding the MO wave-function shows that it cannot properly describe the dissociation of the molecule:

$$\Psi^{MO} = (l+r)(1)(l+r)(2)(\alpha(1)\beta(2) - \beta(1)\alpha(2)) =$$

$$(l(1)l(2) + l(1)r(2) + r(1)l(2) + r(1)r(2))(\alpha(1)\beta(2) - \beta(1)\alpha(2)) \tag{8}$$

It contains the valence bond description of the bond (the inner two terms) plus high energy ionic terms in which both electrons are localized on either the right or the left center (the outer terms).

The Generalized Valence Bond (GVB) theory[7] can be thought of as a hybrid between the two methods. It maintains the superior description for covalent bonds of the VB theory and also maintains a computationally inexpensive method for including this description within the mathematical framework of MO theory.

The starting point for molecular orbital theory is an antisymmetrized product of molecular orbitals $\Psi_A = |\phi_a\alpha\phi_a\beta\phi_b\alpha\phi_b\beta\phi_c\alpha\phi_c\beta...|$, where each molecular orbital $\phi_\mu = \sum_i c_{\mu i}\chi_i$ is a sum of atomic orbital. These molecular orbital coefficients, $c_{\mu i}$, are optimized to give the "best" orbitals, those that minimize the energy. The molecular orbitals of Ψ_A are constructed to be mutually orthogonal and doubly occupied (for a closed shell system). GVB (within the perfect-pairing approximation) replaces each doubly occupied orbital with a pair of non-orthogonal orbitals, with all pairs being mutually orthogonal:

$$\Psi^{GVB} = A\left[\left(\phi_a\phi_b + \phi_b\phi_a\right)\alpha\beta\left(\phi_c\phi_d + \phi_d\phi_c\right)\alpha\beta\left(\phi_e\phi_f + \phi_f\phi_e\right)\alpha\beta\ldots\right] \tag{9}$$

Intuitively it is unnecessary to describe all pairs with this GVB description; only the valence orbitals would benefit, and then only the orbital of chemical interest.

The above GVB wave-function, due to the non-orthogonal orbitals, will be computationally expensive. However, an alternate, mathematically equivalent description is possible within the context of orthogonal orbitals, the Natural Orbital (NO) representation. The overlapping orbitals ϕ_a and ϕ_b from above describe a bond between atomic orbital χ_1 and χ_2. If these orbitals are rewritten as sums and differences of the atomic orbitals (ignoring normalization):

$$\begin{aligned}\bar{\phi}_a &= \chi_1 + \chi_2 \\ \bar{\phi}_b &= \chi_1 - \chi_2\end{aligned} \tag{10}$$

where these two natural orbitals are now mutually orthogonal. We can rewrite equation (9) now in terms of these natural orbitals for all of the pairs:

$$\Psi^{GVB} = A\left[\left(c_a^2\bar{\phi}_a^2 + c_b^2\bar{\phi}_b^2\right)\alpha\beta\left(c_c^2\bar{\phi}_c^2 + c_d^2\bar{\phi}_d^2\right)\alpha\beta\left(c_e^2\bar{\phi}_e^2 + c_f^2\bar{\phi}_f^2\right)\alpha\beta\ldots\right] \tag{11}$$

where the 2 superscript for the orbitals denotes a doubly occupied orbital, and the sum $c_\mu^2 + c_\nu^2 = 1$ for each pair. Thus, this wave-function can ultimately be written as a sum of

closed shell, doubly occupied determinants. This ability to rewrite the GVB wave-function in such a form will be important later on.

Resonance Method

The computational theory of resonance matrix elements was developed by Voter and Goddard to examine the resonance energy between valence bond (and generalized valence bond (GVB))[7] wave functions and is described elsewhere.[5,8] The following discussion will highlight those parts of the theory that assist in understanding the parallel algorithm.

Consider the resonance energy between two closed shell wave-functions:

$$E_{AB} = \frac{\left\langle \Psi^{A} + \Psi^{B} \middle| \hat{\mathbf{H}} \middle| \Psi^{A} + \Psi^{B} \right\rangle}{\left\langle \Psi^{A} + \Psi^{B} \middle| \Psi^{A} + \Psi^{B} \right\rangle} = \frac{H_{AA} + H_{BB} + 2H_{AB}}{2 + 2S_{AB}} \tag{12}$$

$\Psi^{X} = \left|\phi_i^X \phi_j^X \phi_k^X \ldots\right|$ is a normalized, antisymmetrized molecular wave function, ϕ_i^X are the molecular orbitals (MO's) for wave-function X, and each orbital of Ψ^A may overlap every orbital of Ψ^B. As discussed above, this computation is terribly expensive due to the necessary $(N!)^2$ computations, where N is the number of occupied orbitals. The computational demands were reduced by Voter and Goddard,[5,8] who showed that it was possible to simplify the problem by transforming the orbitals of Ψ^A and Ψ^B such that:

$$\left\langle \overline{\phi}_i^A \middle| \overline{\phi}_j^B \right\rangle = \lambda_{ij}^{A,B} \delta_{ij} \tag{13}$$

where each orbital of Ψ^A overlaps only *one* orbital of Ψ^B, and is orthogonal to all others.

Biorthogonalization reduces the resonance matrix element evaluations to a form very similar to the standard Hartree-Fock (HF) computation:

$$H_{AB} = \left\langle \overline{\Psi}^A \middle| \hat{H} \middle| \overline{\Psi}^B \right\rangle \text{ and } S_{AB} = \prod_{ij} \lambda_{ij}^{A,B} \tag{14}$$

where the overlap has been replaced by a product of the individual orbital overlaps. Expanding the above expression over molecular orbitals leads to:

$$H_{AB} = 2\sum_i \eta_i h_{ii}^{AB} + \sum_{ij} \eta_{ij}\left(2J_{ij}^{AB} - K_{ij}^{AB}\right) \quad \eta_i = \frac{S_{AB}}{\lambda_i},\ \eta_{ij} = \frac{S_{AB}}{\lambda_i \lambda_j} \tag{15}$$

$$h_{ii}^{AB} = \left\langle \bar{\phi}_i^A(\chi_1) \middle| \hat{h} \middle| \bar{\phi}_i^B(\chi_1) \right\rangle, \text{ the one electron term} \tag{16}$$

$$J_{ij}^{AB} = \left\langle \bar{\phi}_i^A(\chi_1)\bar{\phi}_j^A(\chi_2) \middle| \frac{1}{r_{12}} \middle| \bar{\phi}_i^B(\chi_1)\bar{\phi}_j^B(\chi_2) \right\rangle, \text{ the coulomb term} \tag{17}$$

$$K_{ij}^{AB} = \left\langle \bar{\phi}_i^A(\chi_1)\bar{\phi}_j^A(\chi_2) \middle| \frac{1}{r_{12}} \middle| \bar{\phi}_j^B(\chi_1)\bar{\phi}_i^B(\chi_2) \right\rangle, \text{ the exchange term} \tag{18}$$

where χ_1 and χ_2 are electrons.

Generalizing this result to the open-shell case requires treating the alpha and beta spin systems separately when performing the biorthogonalization. This treatment is necessary in order to produce transformations which leave the energy unchanged:

$$H_{AB} = \sum_{i\alpha} \eta_{i\alpha} h_{i\alpha,i\alpha}^{AB} + \sum_{i\beta} \eta_{i\beta} h_{i\beta,i\beta}^{AB} + \sum_{i\alpha,j\alpha} \eta_{i\alpha,j\alpha}\left(J_{i\alpha,j\alpha}^{AB} - K_{i\alpha,j\alpha}^{AB}\right) +$$

$$\sum_{i\beta,j\beta} \eta_{i\beta,j\beta}\left(J_{i\beta,j\beta}^{AB} - K_{i\beta,j\beta}^{AB}\right) + \sum_{i\alpha,j\beta} \eta_{i\alpha,j\beta}\left(J_{i\alpha,j\beta}^{AB}\right) \tag{19}$$

where the α and β indices span α and β spin, respectively, and the η's are as defined above. Further generalizing this result for multi-determinantal wave-functions (including GVB wave-functions):

$$\Phi^A = \sum_a C^{Aa}\Psi^{Aa} \quad \text{and} \quad \Phi^B = \sum_a C^{Ba}\Psi^{Ba} \tag{20}$$

the matrix element can be rewritten, giving a sum of single-determinant pair energy calculations:

$$H_{AB} = \sum_a \sum_b C^{Aa} C^{Bb} \left\langle \bar{\Psi}^{Aa} \middle| \hat{H} \middle| \bar{\Psi}^{Bb} \right\rangle \tag{21}$$

Using a basis set expansion:

$$\overline{\phi}_i^{Aa} = \sum_{\mu} c_{\mu i}^{Aa} \chi_\mu \tag{22}$$

and rewriting H_{AB} in terms of density matrices, we have the following expression:

$$\sum_{ab} C^{Aa} C^{Bb} \left\langle \overline{\Psi}^{Aa} \middle| \hat{H} \middle| \overline{\Psi}^{Bb} \right\rangle =$$

$$\sum_{ab} C^{Aa} C^{Bb} \sum_{\mu\nu\lambda\sigma} \underbrace{D_{\mu\nu}^{ab}\left(T_{\mu\nu} + V_{\mu\nu}\right)}_{\text{one electron contribution}} + \underbrace{\left\langle \chi_\mu \chi_\nu \middle| \chi_\lambda \chi_\sigma \right\rangle \left(2 D_{\mu\nu}^{ab} D_{\lambda\sigma}^{ab} - D_{\mu\sigma}^{ab} D_{\lambda\nu}^{ab}\right)}_{\text{two electron contribution}} \tag{23}$$

where $D_{\mu\nu}^{ab} = \sum_i c_{\mu i}^{Aa} c_{\nu i}^{Bb}$ is a $\mu\nu^{th}$ pseudo-density† matrix element (where the η's have been incorporated into the density matrices) for the ab^{th} determinant pair, $\left\langle \chi_\mu \chi_\nu \middle| \chi_\lambda \chi_\sigma \right\rangle$ is the two-electron integral over basis functions, $T_{\mu\nu}$ is the kinetic energy over basis functions, and $V_{\mu\nu}$ is the potential energy over basis functions. The most time consuming part of the above calculation is the two electron contribution. The desire is to take advantage of modern computing technology to increase the speed of the resonance calculation: the focus will be on increasing the efficiency of the two electron contribution to the energy. To accomplish this acceleration, the inherent parallel structure of the theory must be discovered; this parallel structure of the resonance theory will be discussed in Chapter 6.

Program Design for the Resonance Program

There are two conceivable ways to approach this project: one could either use and expand the existing code, or one could start from scratch and design an entirely new program. Because significant advancements have been made in both computer hardware and software technology since the original programs were written, the latter approach was

---

†These so-called pseudo-density matrices are defined in an analogous manner to density matrices, which are defined as $D_{\mu\nu} = \sum_i c_{\mu i} c_{\nu i}$.

taken. The algorithm designs will be described in the following chapters (for both parallel and distributed computing). The remainder of this chapter will be devoted to a discussion of the overall architecture and design of the program.

C++ Programming Language

One major problem with older computer languages such as FORTRAN is that they do not assist in the writing of structured computer code. While it is possible to write such code using the older languages, programming is often facilitated by more modern languages. Many benefits ensue from writing structured code: ease of debugging, maintenance, and deciphering algorithms, etc. One recent advancement that truly assists the writing of organized code was the development of *object oriented* languages and design. At its most basic level, an object oriented design breaks a program down into logical units called objects, which are a collection of data and their associated functions. A simple, illustrative example of an object is a matrix: conceptually, it is an ordered list of numbers with a collection of rules (or functions) describing how to manipulate the numbers.

One obvious benefit of using an object oriented design is that there is, as shown above, a very natural mapping between the way one thinks about operations and the way one programs them. In the case of the resonance calculation, many chemical concepts used also have a very natural mapping onto objects: for example, molecules can be thought of as data (atomic positions, atomic data, basis sets, etc.) and functions (coordinate transformations, basis set manipulations, etc.). Thus, the use of objects clarifies the logic of the program and the structure of the data.

One other benefit of using object-oriented design is, as mentioned above, the savings in debugging and maintaining code. Because an object consists of data and code, there is a natural encapsulation of the data within the object. Thus, there is a structural barrier between the data within the object and the use of the data elsewhere within the

program. Two benefits ensue: first, the data can only be modified through the explicit functions of the object, so that data cannot be inadvertently modified (the data is "safe"). In addition, each object becomes self-contained; only each object needs to be debugged and not the entire program. Of course, it is possible to write code in this manner in other languages. However, object-oriented languages certainly facilitate this design.

C++ was the language chosen for this project for two reasons: it is object oriented and it has the speed benefits of C. However, the program design was not limited to a single language. As it is possible to mix languages, different languages were used when appropriate. Because FORTRAN is efficient for matrix algebra, that language was used for those operations; the interface to these routines was written in C++, as it allows for more rational handling of the data.

The Tcl Interpreter

When designing the user-interface, it is desirable to maximize the amount of information a user can extract from the program. Additionally, the user should have a significant level of control over each important algorithm within the program. To accomplish this flexibility, the program was provided with an interface to the command language Tool Command Language (Tcl).[9]

Tcl is an *embeddable* and *extensible* command interpreter; it is embeddable because the interpreter is linked into the program and extensible because the native command set of the interpreter can be augmented by C/C++ code. Tcl provides a mechanism by which a text stream is interpreted while our code provides the implementation necessary for the commands. The Tcl language is simple, yet powerful enough to surpass the capabilities of most specialized "macro" languages used in computational chemistry codes. Tcl includes loops, conditional expressions, and variables. The main loop of the program consists of collecting input characters (either from a script file, a TCP/IP socket connection, or an interactive command line) and passing them into the Tcl interpreter.

Tcl Enabled Objects

One major problem with data handling and functionality within programs is the accessibility of data and routines to the user. Often, useful information or functions are buried deep within the program; to make them accessible requires a significant reprogramming effort. Ideally, users would be able receive raw data from a program and then transform it according to their needs. The programming effort would be reduced, as only primitive functions would be necessary, and the user would gain more flexibility from the program, especially for needs not originally envisioned.

Tcl enabled objects have been utilized to accomplish the desired flexibility. This joining of Tcl with C++ objects in computational chemistry was pioneered by Coley,[10] and essentially provides each important object within the resonance calculation with an interface to the Tcl language, making them accessible to the user.

One of the most important Tcl commands that was implemented is "new"; this command allows users to instantiate one of the chemical C++ objects. For example, to load a molecule, the user enters the command *new Molecule <molecule name>*. Once instantiated, a new chemical object provides additional Tcl commands having a nearly one-to-one correspondence with the methods provided by the underlying object. In the molecule example, there are commands for loading the molecular structure, loading wave function coefficients, extracting basis set overlap matrices, etc. We refer to these objects as *Tcl-enabled objects*, as they are C++ objects available at the user-level via Tcl.

As a result of Tcl-enabling all important C++ objects, the user can instantiate, access, and control all of the major data structures and algorithms in the program. This enabling allows an unprecedented flexibility in constructing a calculation and inspecting its results. A few examples illustrate this point. Suppose the user wishes to construct an electronic state from a superposition of two wave-functions whose coefficients are stored on disk, and use the resulting wave-function in a resonance calculation. Using the

commands available to the Tcl-enabled Molecule object, the two wave-functions can be loaded; their coefficients extracted to Tcl-enabled Matrix objects; these Matrices manipulated using standard linear algebra techniques; and the resulting Matrix returned back to a Molecule object. The modified Molecule object is then used in the resonance calculation. This is accomplished by the user without modifications or additions to the program.

As another example, consider the task of reading a wave-function from a source not currently supported by the resonance program. For most programs this would require additional code to be linked into the program to support the new file format. However, using Tcl-enabled objects and text processing capabilities built into standard Tcl, the user can write a script to import foreign file formats directly into the Tcl-enabled Molecule object without needing to recompile and relink the program.

The use of Tcl and Tcl-enabled C++ objects has proven extremely advantageous during normal running and debugging as well. Because of the high degree of access to internal data structures and algorithms, many tests could be performed at the script level during debugging. For example, at a point where wave functions should be biorthogonalized, a debugging script can easily extract the wave function coefficients to Tcl-enabled Matrix objects, compute the overlap matrix, and check for a diagonal matrix. Debugging time was greatly decreased by reducing the need to install diagnostic print statements and reducing the need for recompiling and relinking.

Program Architecture for the Resonance Program

In order to accomplish the desired flexibility, four design features were incorporated into the overall structure of the program:

1) Random access to data

2) Arbitrary indexing for all of the data

3) General input and output

4) Segregation of calculation routines from control routines.

The first two points above are quite important, as will be seen in the later chapters of this section. In many programs, the order in which the data is stored, either on disk or in memory, dictates the order in which the calculation must be performed, and thus dictates the basic structure of the program. For example, if an integral set is stored sequentially on disk and can only be read sequentially, the calculation must then be performed sequentially, starting at index 1 and running to the end. Minor improvements can be made to this program, such as speeding up certain parts (such as matrix multiplication). However, no radical improvements can be made that would not require a complete alteration of the structure.

In order for the program to run as fast as possible, as well as permit the freedom to explore non-sequential structures and algorithms, it was necessary to allow completely random access to all stored data, including the integral set stored on disk. To accomplish a random access, a utility program was written that reads in a current stored, sequential integral set and writes out a random access file.

To make full use of the randomly accessible data, it was necessary to allow for an arbitrary indexing scheme. As shown in equation 15, the total resonance matrix element is a multi-index summation, in this case with six independent indices. Generally, these summations are treated linearly as a nested series of loops (Scheme I) which are rigidly incorporated into the calculational part of the program. Note that because the order of the indices is fixed, sequentially ordered data is sufficient.

Scheme I. Traditional Nested Loop Treatment of Multi-Index Summation

```
i = 1 to 100
  j = 1 to 100
    k = 1 to 100
      l = 1 to 100
      .....
      end l
    end k
  end j
end i
```

A different approach is necessary. Instead of incorporating the organization within the calculational parts of the program, calculational routines were designed that are completely general in their input, but specific in their task. The basic "unit" of the calculation is a particular contribution to the two-electron energy (equation 23). All that is required to calculate a particular contribution is the specification of its indices. It is assumed that the necessary data will be set up beforehand.

Thus, because the calculation routine determines a single contribution from an arbitrary set of indices, the order in which the indices are traversed is completely flexible. Thus, if it is determined that a slight reorganization of the indexing is necessary to achieve optimal efficiency, this can be accomplished with ease.

Ultimately, it is desired that resonance program will be able to accept any form of input for integrals, coefficients, and "program specification" data. Currently, it uses the output from the MQM series of programs,[11] but it has been programmed in such a way to make the input of other formats straightforward. A particular, generic interface has been programmed into the code for both the integral and coefficient matrix inputs. Thus, all that is required to accept another format of input is a "module" that "knows" how to read the new format.

A final design element that is important for the resonance program is the segregation of the organization and calculation parts of the program. As was stated earlier, the routine

that calculates the particular contribution to the two-electron energy was written to calculate that specific contribution, but was also written to be called with any set of indices. Thus, the control for this routine was removed from its depths to a separate routine. All such controls for the calculations are gathered into one separate unit. The logic of such a segregation can be seen if one views the ultimate calculation as essentially a large, rather complex exercise in counting. The simple expression within the summations in equation 23 is easy to understand: it is just a handful of multiplications and sums. The real complexity comes when the summations are introduced. Thus, if this counting, or bookkeeping of indices, is segregated from the actual calculation, which is simple, an increased flexibility and clarity of the code ensues.

The real power of this idea will be demonstrated fully during the discussion of the parallel and distributed algorithms, but a simple example here will suffice: as the algorithm was being modified and analyzed, the order in which the summations were tallied was constantly changing. These modifications were straightforward to accomplish, as they didn't disrupt any of the calculational part of the program.

References

1. (a) Pauling, L. *J. Am. Chem. Soc.*, **1931**, *53*, 1367. (b) Pauling, L. *J. Am. Chem. Soc.*, **1931**, *53*, 3225. (c) Pauling, L. *J. Am. Chem. Soc.*, **1932**, *54*, 988. (d) Pauling, L. *J. Am. Chem. Soc.*, **1932**, *54*, 3570. (e) Pauling, L. *Proc. Nat. Acad. Sci*, **1932**, *18*, 293.
2. Slater, J. C. *Phys. Rev.*, **1931**, *37*, 481.
3. (a) Hückel, E. *Z. Physik*, **1931**, *70*, 204. (b) Hückel, E. *Z. Physik*, **1931**, *72*, 310. (c) Hückel, E. *Z. Physik*, **1932**, *76*, 628. (d) Hückel, E. *Z. Physik*, **1933**, *83*, 632.
4. Jackes, C. F.; Davidson, E. R. *J. Chem. Phys.*, **1976**, *64*, 2908.
5. Voter, A. F.; Goddard, W A., III *J. Chem. Phys.*, **1981**, *57*, 253.
6. Unpublished programs, A. F. Voter, J. M. Langlois.
7. (a) Bobrowicz, F. W.; Goddard, W. A., III *Methods of Electronic Structure Theory*; Schaefer, H. F., III, Ed.; Plenum Publishing Corp.: 1977. (b) Goddard, W. A., III; Ladner, R. C. *J . Am. Chem. Soc.*, **1971**, *93*, 6750. (c) Ladner, R. C.; Goddard, W. A., III *J. Chem. Phys.*, **1969**, *51*, 1073. (d) Hunt, W. J.; Hay, P. J.; Goddard, W. A., III *J. Chem. Phys.*, **1972**, *57*, 738.
8. Voter, A. F., Ph. D. Thesis, California Institute of Technology, 1983.
9. Ousterhout, J. K. *Tcl and the Tk Toolkit*, Addison-Wesley: Reading, MA, 1994.
10. Coley, T. R., Ph. D. Thesis, California Institute of Technology, 1993.
11. Goddard, W. A., III, *et al.*, California Institute of Technology, unpublished.

Chapter VI

The Parallel and Distributed Algorithms

Abstract

This chapter contains a brief review of both parallel and distributed computing, emphasizing the important aspects of each form of concurrent computing. Based on the resonance method and program design described in Chapter V, an algorithm for efficiently computing resonance matrix integrals is presented for both parallel computers and distributed computing environments.

Parallel Computing: Introduction

Parallel computation, or the operation of a single program concurrently on more than one computer processor, holds the promise for dramatic increases in speed for many computational problems. In theory, the only limitation to a program's speed is the number of processors on which it is running. However, it is still not obvious how to program to effectively take advantage of a concurrent computer's capability. While code optimization on a single processor machine is well understood, the same is not yet true for parallel computers. More fundamentally, not every algorithm lends itself to effective parallelization.

The main requirement for effective parallelization is an independence of the component parts of an algorithm. For example, if step B is dependent upon the completion of step A, then steps A and B cannot be run concurrently. A good example of an algorithm that is comprised of a series of independent operations is the multiplication of two matrices of arbitrary dimensions. The operations to calculate each element of the new matrix are strictly independent, so that in theory each element could be calculated on a different processor if enough were available. Examining this case even further, the computation of the individual elements also presents an opportunity for parallelization. As each element is a sum its computation could be broken down into, for example, three sums, running on three processors with a final sum of the three results giving the final matrix element.

The description above of a parallel computation of matrix multiplication is an example of a *symmetric parallelization* scheme, in which all processors work simultaneously on the same task but with different data. Conceptually and practically, symmetric parallelization is often simpler to deal with than *asymmetric parallelization*, where sets of processors work on different tasks. For example, one set of processors may be reading data, others may be performing calculations, while a third set may be writing results to disk. Although it can be more difficult to program, asymmetric parallelism will

frequently exploit the parallel structure of a particular algorithm more effectively than the more restrictive symmetric parallel model.

The degree of success of parallel algorithm also depends on the focus of the improvements. For example, if a program spends the majority of its running time performing a single task, it would be wise to implement a *fine grained* parallel scheme, in which all of the processors are dedicated to solving that single task. Through the use of every processor, the amount of work per processor is reduced significantly. Fine grained parallel schemes work particularly well when a large number of processors are available. Although not strictly related, fine grained parallelism is often used in conjunction with symmetric parallelization. A typical example involving fine grained (and symmetric) parallelization is shown in Scheme I, in which only the most time consuming portion (matrix inversion) of the program is split using many processors. However, many computing environments do not have vast numbers of processors at their disposal. In addition, many programs do not have a single task that overwhelms all others in the program.

A better option in these cases is *coarse grained* parallelization, in which the program is split at a higher level. The program can be split over, for example, routines. In these cases, fewer processors are used to accomplish the speed improvements. A typical example of coarse grained parallelization for the same program is shown in Scheme II. Another thing to note is that a coarse grained parallel scheme does not preclude sub-parallelization. In Scheme II, the matrix inversion could be run in parallel too, like in the Fine Grained Parallel example.

In all these schemes, the aim is to reduce the computing time as efficiently as possible. The reduction achieved for the number of processors is called the scaling. Ideal scaling is an inverse relationship between the time and the number of processors. In

theory, if n processors are used, each computes $1/n^{th}$ the total computation, leading to the ideal scaling of T/n, where T is the time. *

Scheme I: Fine Grained Parallel

specify calculation

read input from disk
matrices A, B, E, F, and I

add two matrices
A + B = C

multiply two matrices
D * F = G

start parallel section

invert a matrix
$H = I^{-1}$

end parallel section

write C
write G
write H
end program

Scheme II: Asymmetric, Coarse Grained Parallel

specify calculation

read input from disk
matrices A, B, E, F, and I

start parallel section

add matrices	*multiply matrices*	*invert matrix*
A + B = C	D * F = G	$H = I^{-1}$
write C	*write G*	*write H*

end parallel section

end program

A major concern while designing a parallel algorithm is how best to distribute the computational load amongst the processors so that all processors remain continuously busy; this process is called *load balancing*. The manner in which the load is distributed may be either static or dynamic. Static load balancing determines the computational effort distribution at the beginning of the program execution. Although simpler to implement, programs which employ a static load balancing scheme cannot adjust to competing resource demands on the computer. In addition, static load balancing schemes cannot be used effectively on a variety of different computer systems, where the balance of resource speeds (*e.g.*, between computation and I/O) vary greatly.

---

*In this case the time referred to is the time required to complete the computation on a single processor.

Algorithm[1]

Goals

As discussed in Chapter V, the most time consuming part of the total resonance calculation (1) is the computation of the two-electron energy contribution:

$$\left\langle \overline{\Psi}^{Aa} \middle| \hat{H} \middle| \overline{\Psi}^{Bb} \right\rangle = \sum_{\mu\nu\lambda\sigma} \underbrace{D_{\mu\nu}^{ab}\left(T_{\mu\nu} + V_{\mu\nu}\right)}_{\text{one electron contribution}} + \underbrace{\left\langle \chi_\mu \chi_\nu \middle| \chi_\lambda \chi_\sigma \right\rangle \left(2D_{\mu\nu}^{ab} D_{\lambda\sigma}^{ab} - D_{\mu\sigma}^{ab} D_{\lambda\nu}^{ab}\right)}_{\text{two electron contribution}} \tag{1}$$

where $D_{\mu\nu}^{ab} = \sum_i c_{\mu i}^{Aa} c_{\nu i}^{Bb}$ is the $\mu\nu^{th}$ pseudo-density matrix element for the ab^{th} determinant pair, $\left\langle \chi_\mu \chi_\nu \middle| \chi_\lambda \chi_\sigma \right\rangle$ is the two electron integral over basis functions, $T_{\mu\nu}$ is the kinetic energy over basis functions, and $V_{\mu\nu}$ is the potential energy over basis functions. The design of the algorithm will focus on increasing the speed of this computation. It is a sum, which indicates that it should parallelize well. Ideal scaling for this computation is the time divided by the number of processors. As the two-electron computation is the most time consuming, ideal parallelization is roughly T/n, where T is the time to compute the two-electron energy and n is the number of processors.

The parallel algorithm is designed to meet four goals. First, it is desired to always be computing a partial two-electron contribution to the energy. Second, the ability for dynamic load balancing is also desired. Third, the program should run as quickly and efficiently as possible. Finally, the algorithm should be as general as possible, so that it may be run on a variety of machines. To meet all of these goals, a coarse grained, asymmetric parallelization scheme is implemented.

Background Notation

Generally, the two electron integrals are stored as a set of all $\lambda\sigma$ indices for a specific $\mu\nu$ index; it is this set to which the $\mu\nu$ index refers. In the following discussion $\mu\nu$

and *ab* are "pair indices": they span all pairs of μ,ν (basis functions) and a,b (pseudo-density matrices) indices, respectively. While two separate indices comprise the pair index, the pair index array can also be thought of as a linear array; in the following discussion, it will be treated as a linear array. Thus, the notation $\mu\nu+1$ indicates the next integral pair index in the usual sequence of μ,ν pairs where μ is greater than ν: 1,1; 2,1; 2,2; 3,1;...etc. for a symmetric matrix. Similarly, $ab+1$ denotes the next density matrix pair index in the usual sequence of pseudo-density matrix pairs: 1,1; 1,2;...1,n; 2,1; 2,2;...2,n;...n,n, where n is number of matrices.

Parallel Algorithm: Description

The two electron contribution to the total energy:

$$E_{te} = \sum_{ab\mu\nu}\left\{E_{ab\mu\nu} = \sum_{\lambda\sigma}\langle\chi_\mu\chi_\nu|\chi_\lambda\chi_\sigma\rangle\left(2D^{ab}_{\mu\nu}D^{ab}_{\lambda\sigma} - D^{ab}_{\mu\sigma}D^{ab}_{\lambda\nu}\right)\right\} \tag{2}$$

is the most time consuming task, which the parallel algorithm improves. This calculation involves a sixfold summation over the indices a, b, μ, ν, λ, and σ, so the first decision is how exactly to break this up computation. The main goal is to be constantly computing some portion of the above summation. Ideally, the integrals and the density matrices could all be stored in memory. Then, parallelizing the summation would be a trivial task: just assign each of n processors 1/n of the above work. However, such storage is prohibitive: the integral file typically is at least 100 Mb for an interesting case, and if there are many density matrix pairs, this storage could be another 50 to 100 Mb. The internal memory of most machines is about 200-300 Mb, making such storage impossible.

Thus, a more clever solution is necessary. As stated above, the integrals are stored as an ordered array of $\lambda\sigma$ indices for a particular $\mu\nu$ pair. Similarly, the density matrices can be stored for each *ab* pair. Each array or matrix must be read in or calculated before

any computations can be performed. Thus, a straightforward way to arrange the calculation would be as written above: consider the basic unit of computation $E_{ab\mu\nu}$, and a complete calculation involves summing over this partial energy. The benefit of such an organization is that it provides a clear set of conceptually independent tasks that need to be accomplished: in order to calculate this particular contribution for a set of integrals (pair index $\mu\nu$) and a density matrix (pair index ab), the following operations are necessary:

1) Read in or compute the integrals (all $\lambda\sigma$ for a particular $\mu\nu$ index)

2) Read in or compute the pseudo-density matrices (index ab)

3) Calculate the energy contribution for the $ab\mu\nu$ indices ($E_{ab\mu\nu}$)

The first two operations are "setup" operations that prepare the data required for the energy calculation in a form that allows for the most efficient computation. The next step to designing the parallel algorithm is to determine the most efficient manner in which to compute each $E_{ab\mu\nu}$ while also setting up the necessary information. Because these are three different operations to be run concurrently, an asymmetric parallelization scheme must be implemented.

Pipeline Algorithm

While it was stated above that the calculation has been divided into three conceptually different tasks, the above operations are *not* independent: the two-electron energy calculation requires prior set up of the integral and density matrix information. Despite these interdependencies, the separation of the computation into the above operations represents the first opportunity for parallel computation. Each operation will have a collection of processors (processor pool) dedicated to completing the task in hand; in order to keep each pool simultaneously active, a *pipeline* will be used to control the data flow: while a partial two-electron energy contribution, $E_{ab\mu\nu}$, is being calculated by one of

the processor pools, the integral set $\mu\nu+1$ and density matrix $ab+1$ are being simultaneously read or calculated by processor pools two and three. In Figure 1, each labeled operation occurs simultaneously in a single time step on different processor pools. When all three tasks are finished for the specified pair indices (time step n), the results flow as indicated and for the next time step, the computations start on the next set of indices.

Figure 1. Pipeline for Computation of $E_{ab\mu\nu}$

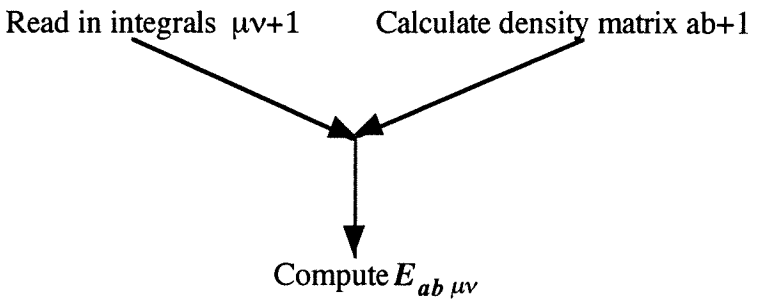

Such a simple design is straightforward to understand and program. However, it suffers from three major flaws. First, because each operation will have a dedicated processor pool, the set up data must move from the integral and density matrix pools to the computation pool. The amount of data movement will not be trivial, especially as the computation grows, and will create inefficiencies in the calculation. Second, because data is stored for only two time steps, there will be a tremendous redundancy in the set up computations. If one is not careful, it is possible to perform $d*i$ set up operations, where d is the number of density matrix pairs and i is the number of integral pairs. Third, each time step requires the setting up of 1 integral and 1 density matrix to calculate one $E_{ab\mu\nu}$. Assuming the time to perform each operation is roughly equal, the number of processors dedicated to each task should be equal: 1/3 of the total number of processors. Thus only 1/3 of the processors are dedicated to computing E_{te}; the best scaling that 1/3n processors can accomplish is 1/(n/3). As ideal scaling is 1/n, this algorithm's maximum speed is only 1/3 of ideal.

A next obvious opportunity for improvement would be to create multiple pipelines feeding into different partial two-electron energy contributions (Figure 2):

Figure 2. Parallel Pipelines for Computation of $E_{ab\mu\nu}$

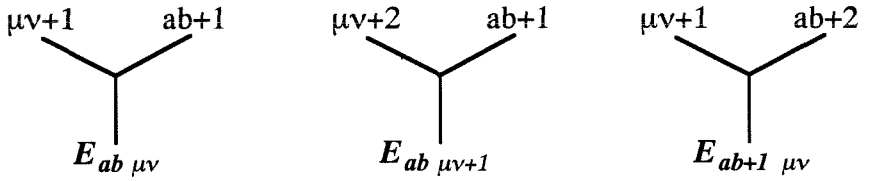

However, this simple duplication of the pipeline leads to inefficiencies: in addition to the problems described above for the simple pipeline, the different pipelines set up information (integrals, density matrices) identical to that needed by other pipelines. In the above example the integral set $\mu\nu+1$ and density matrix $ab+1$ are each being set up twice.

In order to avoid redundant computations, the algorithm is reorganized in terms of a grid of energy computations (Figure 3). Each block on the grid represents a single two-electron computation, $E_{ab\mu\nu}$, and a block's horizontal and vertical locations identify the prerequisite integrals and density matrices. A complete E_{te} calculation requires traversal of the entire grid. The key to efficiently using integral and density matrix information lies in determining how to traverse the computational grid map, and how many grid locations to compute in parallel.

Figure 3. Viewing the E_{te} Computation as a Grid.

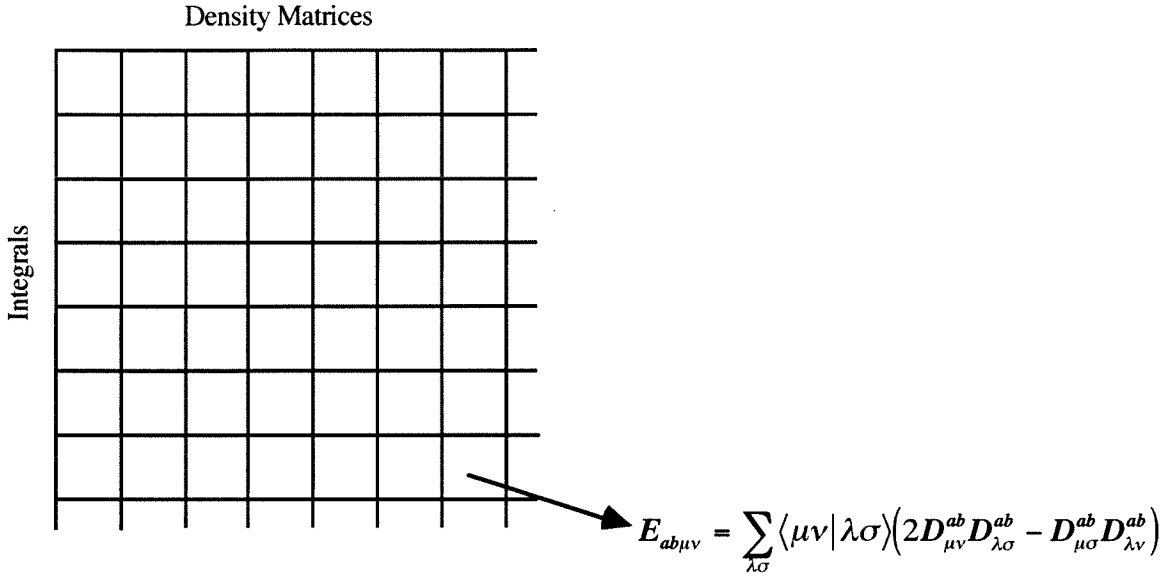

Truncated Wavefront

The solution chosen sweeps a "wavefront" of two-electron energy computations across the grid (Figure 4). At the particular step shown (darkened squares), the energy calculations performed are (*ab*, $\mu\nu$–*5*), (*ab-1*, $\mu\nu$–*4*), (*ab-2*, $\mu\nu$–*3*), ..., (*ab-5*, $\mu\nu$), where the pair indices correspond to the prerequisite density matrices and integrals, respectively. Concurrently, the *ab+1* and $\mu\nu$+*1* set up operations are performed. The energy calculations are represented graphically by a diagonal wavefront running from (*ab*, $\mu\nu$–*5*) to (*ab-5*, $\mu\nu$). One obvious benefit of this algorithm is the large reuse of previously set up information. For each time step the energy calculation will involve all 0 to *ab* or $\mu\nu$ information previously set up, requiring only one additional set up operation for each of the integrals and density matrices for the next time step. There will be no redundancy in the set up operations: only one will be required for each of the integrals and density matrix indices. And, because of the high $E_{ab\mu\nu}$ calculation to set up ratio only two processors need be dedicated to performing the set up operations, leaving n–2 to perform $E_{ab\mu\nu}$ computations.

Thus, the scaling per number of processors for this calculation should be good, about 1/(n-2).

Figure 4. Wavefront Propagation

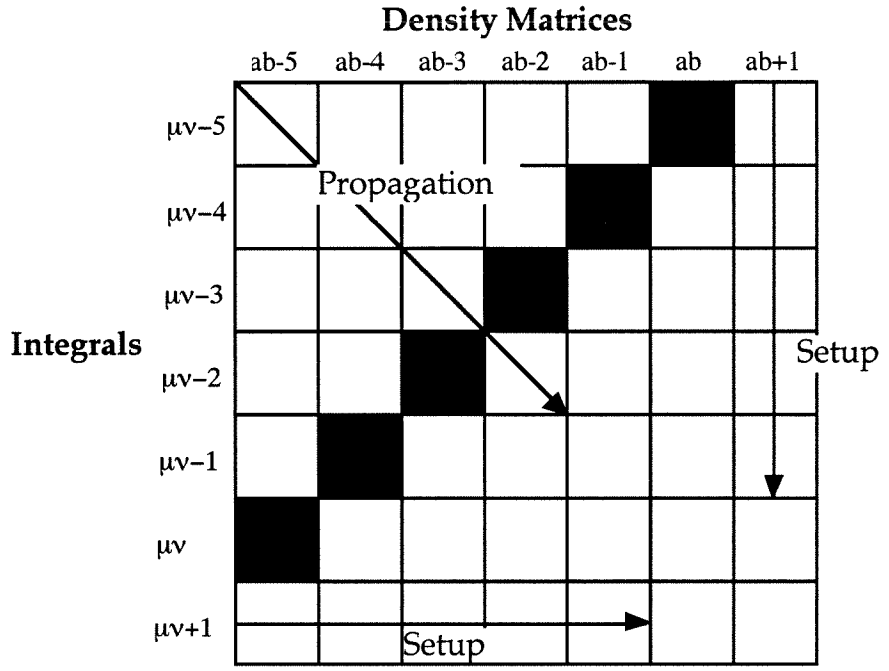

However, the wavefront technique gains efficiency at the expense of larger storage requirements. In the single pipeline (Figure 1) concurrent storage was required for only two sets of integrals ($\mu\nu$ and $\mu\nu+1$) and two sets of density matrices (ab and $ab+1$). Unfortunately, this is not the case for the wavefront scheme. As the wave progresses, all previous information (indices 0 to $ab+1$ or $\mu\nu+1$) is required; only when an axis has been completely swept is the set up information no longer necessary. This memory requirement is a serious problem since, as mentioned previously, large systems will require more memory than is available.

Truncating the wavefront so that the storage requirements do not exceed the computer's capacity is a simple solution to this problem. This truncated wavefront will still maintain the important characteristics of the "full" wavefront: namely the large reuse of previously stored information coupled with a minimal amount of set up operations for the

next time step. However, the question remains as to the most efficient manner to propagate this truncated wave while still visiting every location in the calculation grid.

One straightforward choice is propagating the wavefront along either of the two axes. For example (see Figure 5), if storage limitations require that the range of stored information be restricted to four sets for each of the integrals and density matrices, we can propagate a wave of constant length three along the density matrix axis (allowing one of the four sets for the set up). Completing the first sweep from left to right across the density matrices results in the following contribution to $\boldsymbol{H}_{AB}$:

$$\sum_{\mu\nu=1}^{3}\sum_{ab} \boldsymbol{E}_{ab\mu\nu} \tag{3}$$

Truncating the calculational wavefront has many benefits. In the example, the same integrals are used for the entire sweep along the density axis resulting in significant reuse of memory. Because all set up information cannot be stored, there must be some redundancy in these operations. However, this truncation achieves a good compromise between storage limitations and set up redundancy. In the example, redundancy is eliminated in the integral read operations, and reduced by 2/3 in the density matrix computation.

Additionally, in a one-to-one mapping of the two-electron calculations to processors, the propagation described requires no movement of the integral information from processor to processor. As shown in Figure 5, processor one has integral-set one stored in its local memory for the entire propagation of the wave along the density matrix axis. The same is true with processors and integral-sets two and three.

Truncation also allows the realization of another goal for this algorithm: program optimization. Because there is a choice along which axis to propagate (either density matrices or integrals), there is a degree of freedom for optimizing the calculation. The slowest set up step can be determined prior to program initiation; it is assumed for Figure 5 that reading the integrals is slower than calculating the density matrices. This slow step can then be performed least often by propagating along the *other* axis (the density matrices in

the example. The redundancy in the slowest step will be eliminated with the "static" propagation described.

Figure 5. Truncated Wavefront Propagation

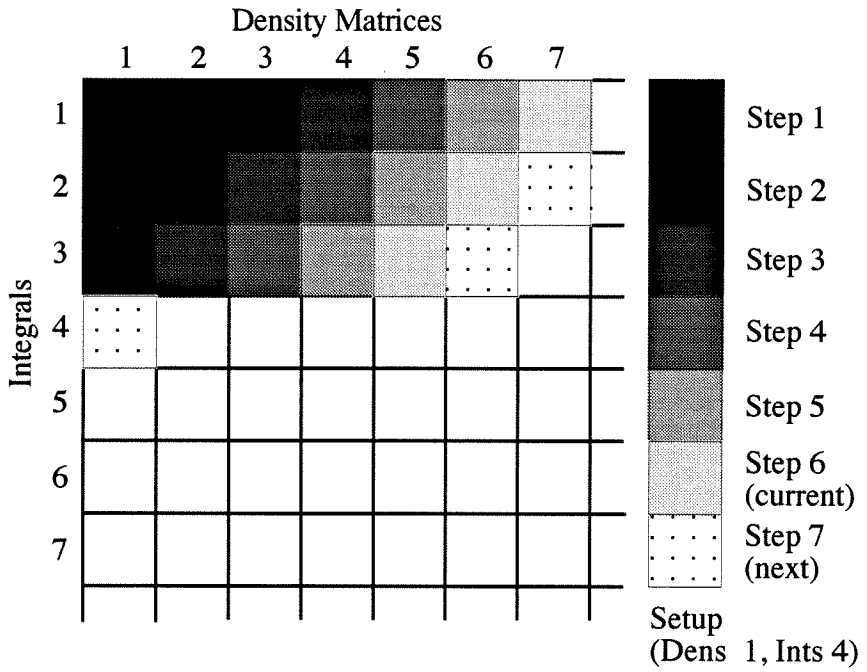

The wavefront formalism allows a smooth transition as one sweep ends and another begins. As shown in Figure 5, the seventh step, which would extend beyond the end of the density matrix indices, "wraps around," restarting at density matrix 1. The obvious alternative to the wavefront formalism, a "vertical scan" (Figure 6), does not allow for this smooth transition. While the vertical scan and the truncated wavefront both accomplish the same number of $E_{ab\mu\nu}$ calculations per time step (3 in the examples) and generally require the same set up per time step (one density matrix), they do not share the same characteristics at the end of a sweep. When the vertical scan is calculating $E_{ab\mu\nu}$ for integral indices 1 to 3, and density matrix index 7 (the final $E_{ab\mu\nu}$ calculation of the row), the next set up required would be $\mu\nu = 4$ to 6 and $ab = 1$, resulting in a less efficient use of memory (storage for six integral-sets required rather than four) and more set up operations to perform, possibly reducing the number of processors in the calculation pool.

Figure 6. Vertical Scan Propagation

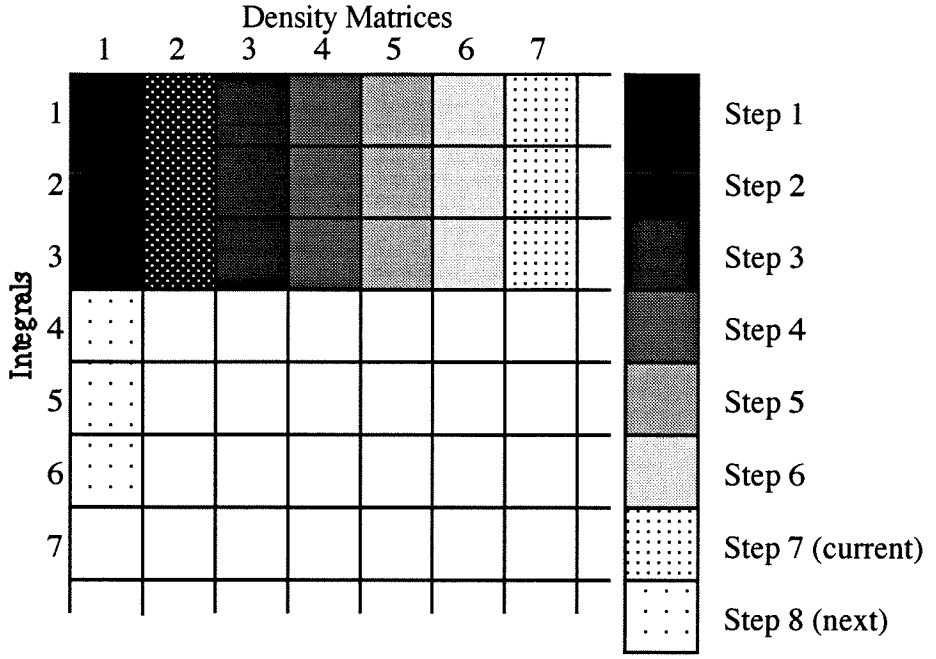

Up to this point, the algorithm consists of (1) splitting up the two-electron energy calculation into three operations (2) running the three operations concurrently in an asymmetric parallel computing scheme and (3) organizing the indexing such that a truncated wavefront is propagated across the index space. In each time step the three different operations will each be computed by one of three processor pools. At the beginning of each time step, the tasks are specified for each pool, and the pool runs the desired computations. Once a task is completed, each pool must wait until the other two have completed their tasks. Ideally, each pool should take the same time to complete their individual tasks although there is no guarantee that such is the case. Thus, in the interest of efficiency, this problem must be addressed.

Load Balancing

For the algorithm to run efficiently, it is desired to minimize inter-processor communication while making continuous, non-redundant use of all available processors (load balancing). Even though inter-processor communication is implicit (*i.e.*, data moves

upon memory access) on a shared-memory multi-processor, it is still costly. These two problems have been addressed previously as the basic design of the algorithm was being discussed. The great reuse of the data by the truncated wavefront algorithm minimizes the necessary communication, as the data that corresponds to the static axis remains with a particular processor for the duration of a sweep. The choice of propagation direction assists in load balancing.

However, it is possible to gain even more flexibility in equalizing the task times by conceptually reorganizing the calculational grid. There is no reason that the basic unit of the grid need be a single $E_{ab\mu\nu}$, although it is easier to visualize the algorithm by describing it in terms of a grid of single energy points. Thus, a new degree of flexibility will be introduced by performing a *composite* of energy component calculations simultaneously. Specifically, the single energy calculations are grouped into larger, square blocks, with a length of **B** (to be determined later); these blocks are used as the basic unit for the truncated wavefront (Figure 5). Although there will not necessarily be a one-to-one mapping of blocks to processors in most calculations, the arguments presented in favor of this organization still hold (minimal inter-processor communication and load-balancing).

This block length, **B**, is the degree of freedom desired which allows for greater load balancing between the processor pools. The number of energy calculations per time step varies quadratically with **B**, since each block represents $\mathbf{B}^2$ $E_{ab\mu\nu}$ calculations. In contrast, the number of set up operations varies linearly, since there are only **B** per block. Thus, by varying the blocklength, the algorithm can regulate the ratio of energy calculations to set up operations performed for each time step. This regulation will ultimately be based on the actual time required to complete each task.

There are three processor pools, one for each task; the desire for no idle processors requires that the time required to complete all tasks be equal for each time step. The problem is to determine how many operations within each task (set up and $E_{ab\mu\nu}$

calculations) to perform each time step. One processor is dedicated to each set up operation (density or integrals). It is necessary to determine an expression for the time required to calculate the total energy contribution for a single time step.

Figure 7. Truncated Wavefront Propagation Using Blocking

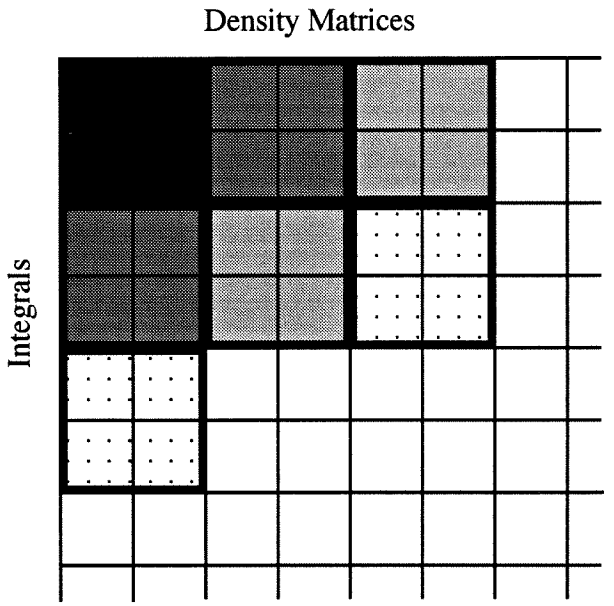

Assuming that one can evenly distribute the $E_{ab\mu\nu}$ calculations needed for a single time step, the time required to perform all $E_{ab\mu\nu}$ calculations for that time step (E_{step}) should just be the time to calculate E_{step} on a single processor divided by the number of processors in the calculation pool. This assumption is valid, as there will generally be a large number of $E_{ab\mu\nu}$ calculations to perform for each time step. The expression for the time to calculate the E_{step} contribution from a single processor must be determined.

The total number of integrals and density matrices stored (assumed to be the same), is represented by **M**; **M** is determined by the size of the available internal memory. If **B** is the block length, then **M/B** blocks of integrals and **M/B** blocks of density matrices can be stored. Recalling that one block in memory is dedicated to the set up, one finds **(M/B) – 1** active blocks (blocks of information available for $E_{ab\mu\nu}$ computations), giving a total of:

$$B^2 * \left(\frac{M}{B} - 1\right) = B(M - B) \tag{4}$$

$E_{ab\mu\nu}$ calculations per time step. Thus, the time required to calculate this energy contribution on a single processor will be:

$$B(M - B) * (E_{ab\mu\nu} \text{ calculation time}) \tag{5}$$

where the "$E_{ab\mu\nu}$ calculation time" is the time require to calculate a single $E_{ab\mu\nu}$ term.

If the number of processors on the machine is ***nproc***, the following is desired:

$$\textbf{Set up time} = \frac{B(M - B) * (E_{ab\mu\nu} \text{ calculation time})}{nproc - 1} \tag{6}$$

as in general one processor is devoted to the set up operations. Equation (6) is then solved for **B**. Ultimately, the algorithm will use live timing data for dynamic load-balancing.

It is also important to know how this algorithm will scale as we vary the number of processors. To do this, it is necessary to find an expression for the total calculation time. We know the ideal time for each step, the expression given above, and need only to determine the total number of steps a complete calculation requires. If there are **T** $E_{ab\mu\nu}$computations to perform for a complete calculation, and **B(M-B)** $E_{ab\mu\nu}$ computations per time step, there are **T / (B(M-B))** steps for a complete calculation. Thus, the total calculation time is

$$\frac{\mathbf{T}*(E_{ab\mu\nu} \text{ calculation time})}{nproc - 1} \tag{7}$$

and the total calculation time should scale inversely with the number of processors. This expression is somewhat unusual since there is no explicit dependency on the set up operations; there is only an implicit dependency in the decrease of the number of processors available for the calculation. As the number of processors increases, this factor should be negligible, allowing optimal parallelization.

The algorithm developed is useful across a wide variety of parallel computers. The current implementation runs on a shared-memory machine. However, as the algorithm is designed to require as little data movement as possible it is also well suited for distributed-memory machines.

The way the calculation is organized lends itself well to this parallel algorithm. In principle, evaluation of single energies, such as resonance, can be so easily divided, as the energy evaluation is a sum. Thus the algorithm described is valid for many electron correlation methods. For self-consistent methods, such as HF or GVB, other computational bottlenecks, such as matrix diagonalization, may preclude a simple adaption of the algorithm described.

Distributed Computing: Introduction

Parallel and distributed computing share the same theoretical basis for speed improvements, which can be thought of as "divide and conquer." Both methods break up the desired computation into smaller pieces which can be run concurrently. However, while the basic approach is the same, the implementation differs.

The most significant difference is that a parallel computation occurs on a single computing machine that has many processors, whereas a distributed computation runs on many machines, each with at least one processor. While each processor in the parallel machine has many of the properties of an independent computer, such as its own memory, only the single computer is independent. Communication between the processors is rapid, as it is internal to the machine. In contrast, communication between different computers is often very slow as it occurs over a network of slower speed than the internal network on the parallel machine. This variance in communication speed is one major difference between the two concurrent computational methods.

Another important difference between parallel and distributed computing is the available internal memory for a computation. A significant concern when designing the

parallel resonance algorithm was the most efficient use of memory: it is impossible to store, on a single machine, all of the necessary information for the calculation. Distributed computing, on the other hand, does not have such strict limitations. In theory, the total amount of available internal memory is limited only by the number of computers used and each computer's memory. This discussion is not meant to imply that one should ignore the memory requirements for each computer: indeed, such requirements will also dictate how the algorithm is structured.

Thus, optimizing a computation for distribution is different from optimizing a calculation for parallel computation. Both methods require independence of the operations to be run concurrently, but the manner in which the calculation will be organized can be quite different: on the parallel machine, sharing of data, while not inexpensive, is not exorbitantly costly; for the distributed system sharing of data is prohibitive.

Algorithm

As described above in the Parallel Algorithm section, the calculation can easily be thought of as a two-dimensional grid that needs to be entirely traversed. The algorithm described for the parallel computation swept over the grid in broad bands. Conceptually, one can also think of breaking the calculation into smaller blocks. For example, if it is desired that 4 computers be used for the computation, theoretically it should be very straightforward to divide the computation into quarters and assign each quarter to a particular computer (Figure 8). Each computer ultimately calculates two numbers, the energy contribution for that particular quadrant of the grid and its contribution to the overlap, S_{AB}. The beauty of this concept is that the communication, which is very slow for distributed computing, consists of the transfer of a handful of numbers. Such a scheme was not considered for the parallel algorithm (where processors are used instead of computers) because it does not use the internal memory particularly efficiently: processors 1 and 3 would be using the same density information, and would both have to set it up

independently. In addition, the total storage requirements for such a scheme would exceed the capacity for a single computer, but not a collection of computers.

Figure 8. Blocking of the Two Electron Energy Computation onto 4 Computers.

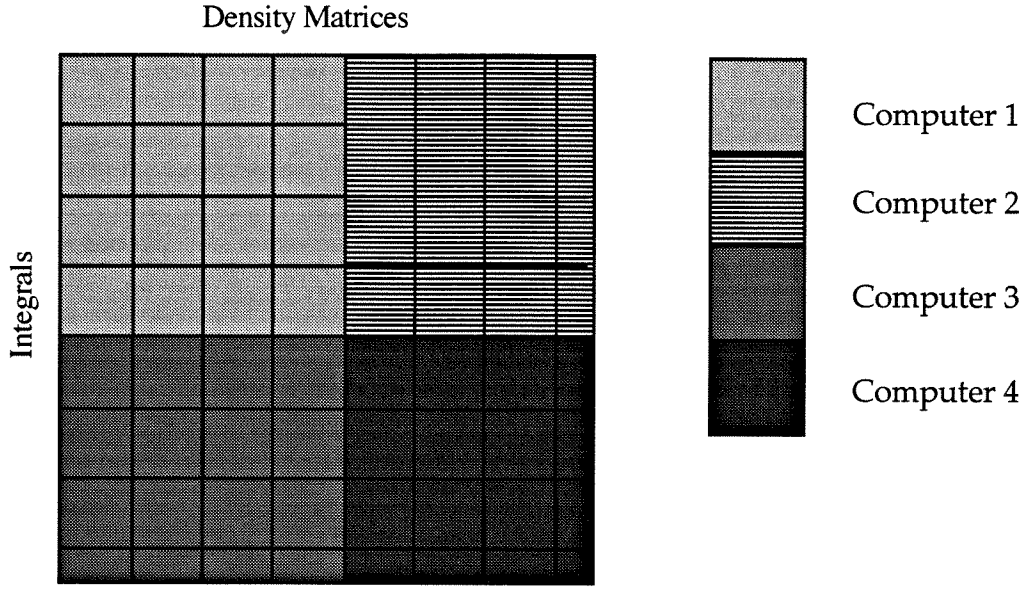

Two features that were incorporated into the overall design of the program (see Chapter V) allow this straightforward division of the computation: (1) random access to the data (both integrals and determinants) and (2) arbitrary indexing for the two-electron energy contribution. As discussed above, the two-electron energy contribution, E_{te}, is just the sum:

$$E_{te} = \sum_{ab\mu\nu} \left\{ E_{ab\mu\nu} = \sum_{\lambda\sigma} \underbrace{\langle \mu\nu | \lambda\sigma \rangle \left(2D^{ab}_{\mu\nu} D^{ab}_{\lambda\sigma} - D^{ab}_{\mu\sigma} D^{ab}_{\lambda\nu} \right)}_{\text{single grid element}} \right\} \tag{8}$$

that runs over the grid elements, $E_{ab\mu\nu}$, and thus E_{te} can be easily divided in any arbitrary way. However, to allow an arbitrary division of E_{te}, the order in which each $E_{ab\mu\nu}$ is calculated must not be fixed. To calculate any particular $E_{ab\mu\nu}$, the ability to retrieve the data in a random fashion is necessary. These two capabilities have been designed into the program.

The optimal manner in which to distribute the computation over computers is not immediately obvious. Above, it was divided into quarters, but another reasonable possibility is a division into "strips" (Figure 9). As discussed above, memory considerations for the individual computers are ultimately important. In the case of Figure 9, the storage (either internal or on disk) for each strip would consist of the entire set of integrals, and one quarter of the density matrices. Obviously, this is not the most efficient use of memory *on each machine*. Figure 8 describes a much more efficient use of memory, where only half the integrals and half the density matrices need to be stored. It is desired to get the maximum number of calculations per stored data, which can be viewed as getting the maximum volume (number of computations) for a given surface area (total amount of required storage) of the block. Thus, it is necessary to divide the calculation into as compact of pieces as possible.

Figure 9. Dividing computation into strips

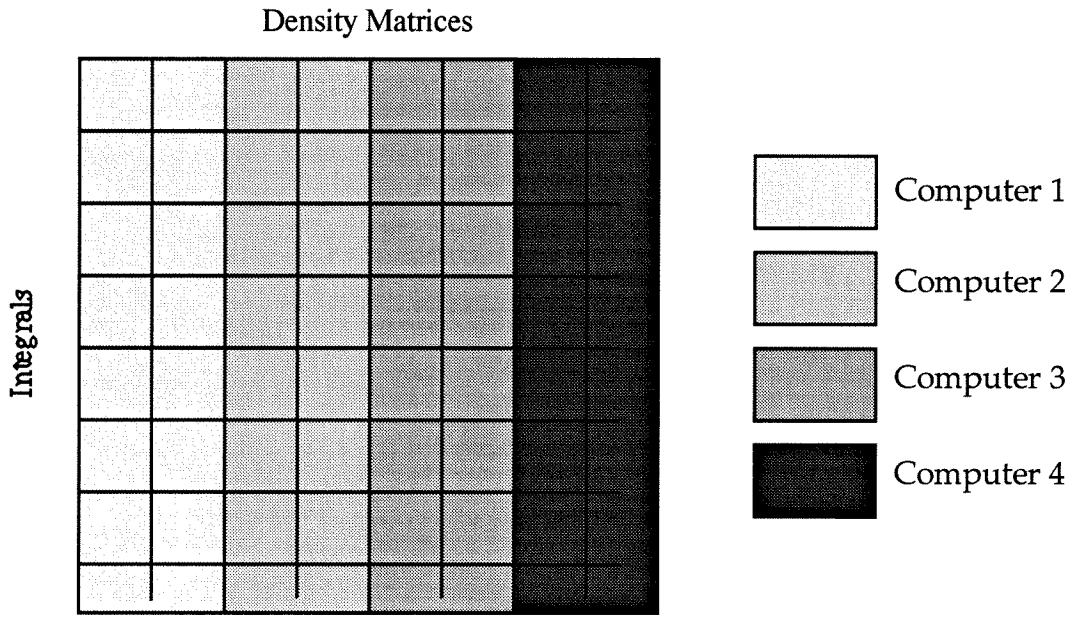

Program Design

It is important to note that the parallel resonance program (as described in Chapter V and the first part of this chapter) was not originally designed for a distributed algorithm.

Only later was it determined that ability to perform distributed computing would be a useful feature for the program. Thus, it is desired to show that the design described in Chapter V is general enough and flexible enough to allow a *different model of concurrent computing* within the same program with very minimal code modifications.

In fact, only trivial modifications to the parallel program were made to allow for distributed computing. Because the control of the program has been segregated from the calculation, it is straightforward to modify only the program control. The major modification necessary is that the program can accept as input a set of starting and ending indices for both the integrals and density matrices. Minor modifications are also necessary to avoid double counting of the one-electron contributions.

To perform a distributed calculation, it is obviously necessary for some overall control to the calculation; generally this is performed by a single computer. The master-and-slave metaphor is used for control: the master determines what computers will be used, specifies the tasks they must perform, and accepts the data when the slaves are finished. The master also performs the final summation necessary. The slaves accept their task from the master, perform their particular contribution, and send their results back to the master.

Tcl is used for this control. Because much of the program was designed around Tcl enabled objects and a flexible input, it has the ability to be "programmed" via Tcl, *i.e.*, through Tcl, the program can be manipulated much more freely than a standard program. This programmable aspect of the program allows for a situation that wasn't envisioned during the original parallel design of the program. With the code modifications described above, the rest of the distributed application was completed with Tcl scripts:

Master Script:

start listening socket

```
set s [tcp server -port $returnPort -command resgvbLogin]
$s start
```

spawn slaves

```
foreach slave $slaveHosts {
     set result($slave) none
     exec rsh $slave -n $slaveScript $masterHost $returnPort
          $slave &
}
```

check results variables

```
set stopPolling 0
while {!$stopPolling} {
     set done 1
     foreach slave $slaveHosts {
          if {$result($slave) == "none"} {
               set done 0
               break
          }
     }
     if {$done} {set stopPolling 1}
     tcp timer after 1000
}
```

collect and sum slave results

Slave Script

determine integral indices and/or determinant pairs to calculate

perform calculation

connect to master on assigned port

```
set c [tcp connect $masterHost $masterPort]
```

send results to master

```
$c send set result($slaveHost,$m$slaveHost,$ii,$jj) $elem
```

Generally, distributed computing is envisioned to involve a collection of single processor computers, maintaining its close similarity to parallel computing, and the algorithms are generally structured to run on this collection of single processor machines. However, nothing precludes the use of parallel and single processor machines together within a distributed computing environment. The adaption of the original parallel program for distributed computing gives the distribution even more flexibility: any type of computer can be used in the distribution, either single or multiprocessor machines.

References

1. Much this work is described in Bierwagen, E. P.; Coley, T. R.; Goddard, W. A., III *Parallel Computing in Computational Chemistry*, Mattson, T. G., Ed., American Chemical Society, Washington, D.C., 1995, pp 84-96.

Chapter VII

Results and Conclusions

Abstract

Timing results are presented for both parallel and distributed computations. Nearly ideal speedups are reported, with the time required to complete a computation having a nearly inverse relationship with the number of processors or computers.

Two molecules are studied with the new resonance program: didehydro [10]annulene and the cyclopentadienyl anion. The results of these studies are also discussed.

Timing Results

In both cases of concurrent computing, the goal is to use more than one processor to increase the speed of a calculation. In the ideal case of concurrent computing, when the algorithm has been perfectly optimized, the time of execution should scale as 1/n, where n is the number of processors. This 1/n scaling is the goal of parallel computing, and proves difficult to accomplish in practice.

Parallel Calculation

All timing results reported come from calculations performed on a Silicon Graphics 4D/480, with eight 40 MHz R3000 processors. The system contains 256 Mb of shared internal memory. Two large problems of chemical interest were chosen for timing tests. The first, calculating the resonance energy of the cyclopentadienyl anion ($C_5H_5^-$, Cp), involves five valence-states where each state has three GVB-correlated pairs (perfect-pairing model) and each state localizes the negative charge on a different carbon atom. The second problem is the calculation of the resonance energy for the molecule 1,6-didehydro[10]annulene ($C_{10}H_6$), a ten membered ring that formally meets the Hückel criterion of (4n+2) π–electrons for aromaticity. The π–valence structure can be written as a resonance between two states of five resonating π–bonds, each of which is correlated in a GVB pair:

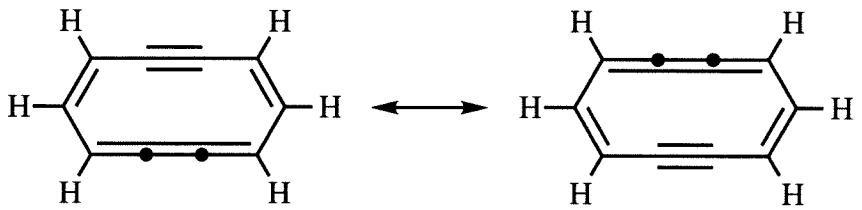

Both calculations were beyond the limits of older programs. In the case of the Cp anion, the resonance between five different valence states cannot be performed in a

straightforward manner with older programs, as they can only calculate resonances between two valence states. In the case of $C_{10}H_6$, a resonance between valence structures each containing five GVB pairs represents a calculation with 1024 determinant pairs, beyond the older program's limit of 1000 pair. Both of these calculations presented fresh opportunities for the new program.

The parallel timing data presented represent the *elapsed* time to completion for each run. Ideally, this time should be related to the number of processors by the following relationship:

$$\text{total execution time on N processors} = \frac{\text{time on a single processor}}{\text{N (processors)}} \tag{1}$$

Figure 1 presents the parallel timing results. According to the equation derived in Chapter VI for the total execution time:

$$\frac{\text{Time on one processor}}{\textbf{\textit{nproc}} - 1} \tag{2}$$

it is found that the algorithm scales with an effective number of processors that is one less than the actual number of processors. This effective number of processors is used when analyzing the data. It is impossible to run the $C_{10}H_6$ computation on seven or eight processors as these computations exceed the machine resources. The scatter in the data is a result of running the program on an otherwise heavily loaded system. It is possible to assure the program runs at a high priority by using *Nanny*,[1] nevertheless, background jobs still had an effect on the run times, most likely due to I/O contention and extra context switching. Because of the other jobs on the system, and the fact that the runs could not have perfect utilization of the desired processors, Figure 1 presents execution time speedups *scaled to 100% utilization of the desired processors* to maintain constancy amongst the data.

Figure 1. Elapsed Time Speedups Scaled to 100% Utilization vs. Effective Numbers of Processors

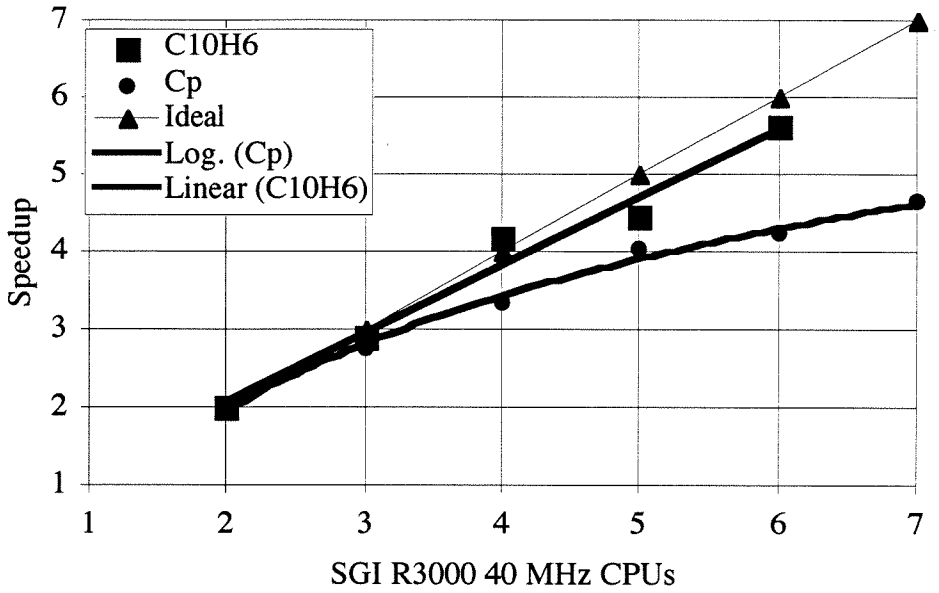

Note that the Cp case begins to exhibit leveling off as the number of processors is increased, while the $C_{10}H_6$ case is still exhibits linear speedups. The Cp case is much smaller than the $C_{10}H_6$ case, and it is believed that its smaller size causes it to begin displaying non-linear speedups more rapidly than the larger $C_{10}H_6$ case. While this phenomenon is not desired, it is acceptable, as the larger cases are the ones for which greater speedups are necessary. Based on these results, it is expected the speedups will scale well to larger numbers of processors, especially for larger systems.

For this small number of processors, the dynamic load balancing included within the algorithm does not affect the scalings or the timings. There are two possible reasons for this: (1) the load is properly distributed at program initiation, so that adjustments are not necessary and (2) it is more difficult to evenly distribute the load with such a small number of processors. It is anticipated that the dynamic load balancing will be more important as more processors are utilized.

Distributed Calculation

Given the current computational setup, it is impossible to get reliable timing results for these calculations. Thus, in Figure 2 is presented a theoretical scaling for the distributed computation. The values in this figure were obtained assuming that communication time and the time for final manipulations of the data will be small: thus the time on an individual computer to run $1/n^{th}$ of the computation represents the time for n computers complete the computation. These data represent an absolute upper bound on the efficiency of the algorithm described in Chapter VI. However, because only two, or at most three, numbers will need to be transferred per computer, the estimate represented by Figure 2 is reasonable. Note that this estimate suggests that even with 100 computers, the distributed algorithm should achieve 75% efficiency, and that ideal scaling is expected for the use of up to 50 computers.

Figure 2. Theoretical Scaling for Distributed Cp Calculation

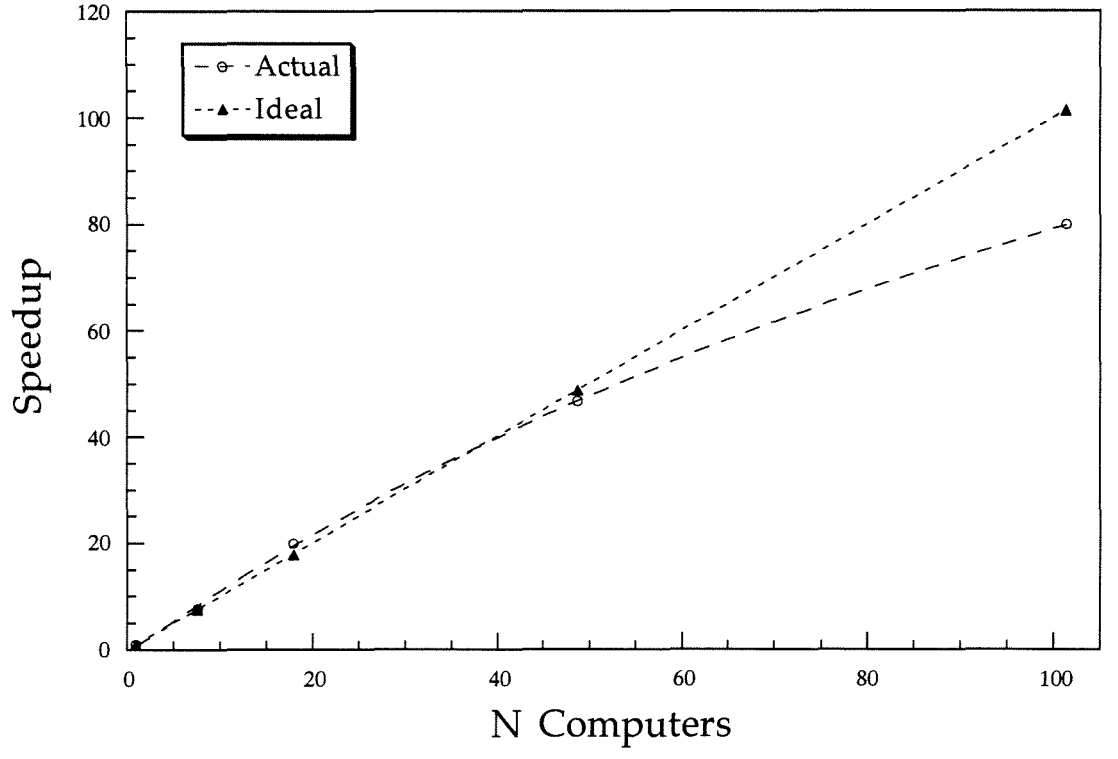

Chemical Results

Computational Details

All calculations were performed using the Dunning-Huzinaga double-ζ basis sets: for carbon the (9s5p/3s2p) set was used and for hydrogen the (4s/2s) scaled set (ζ=1.2) was used. All GVB calculations were performed using the perfect pairing (PP) approximation.

$C_{10}H_6$

This system is of interest for understanding the activity of enediyne antitumor antibiotics.[2] It is a formally aromatic molecule, although this aromaticity has not been tested. The molecule undergoes a rapid transformation to a naphthalene biradical, even at temperatures as low as –78° C. Thus, it is of interest to determine whether this molecule is in fact aromatic, *i.e.* that it has resonance stabilization.

As the molecule has not been characterized structurally, a geometry optimization of the molecule was performed at the HF level. This level of calculation, in which the orbitals are delocalized, represents the cheapest wave function least likely to introduce a calculational bias into the geometry. A calculation in which the π-electrons are correlated into GVB-PP orbitals would distort the geometry, giving alternating "single" and "double" bonds. The geometry optimized with D_{2h} symmetry is described in Figure 3.

Figure 3. Optimized Geometry of $C_{10}H_6$

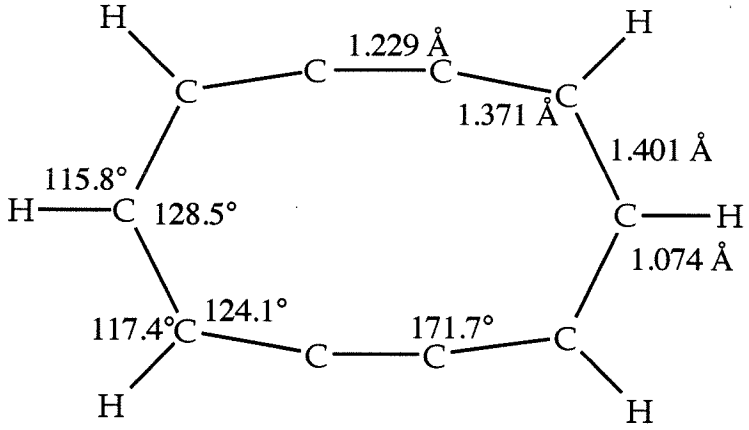

The resonance calculation is performed between two GVB(5/10) wave-functions, where the 10-π electrons have been correlated into 5 pairs within the PP approximation for each of the two valence structures. The values of H_{AB}, H_{AA}, and S_{AB} for $C_{10}H_6$ are shown in Table 1 (note that H_{AB}, H_{AA} are purely electronic energies; the nuclear repulsion energies are not included). These values lead to a calculated resonance energy for $C_{10}H_6$ of 22.3 kcal/mol.

Table 1. Resonance Matrix Elements and Overlaps for $C_{10}H_6$

Resonance Interaction	H_{AB} (hartrees)	H_{AA} (hartrees)	S_{AB}
$C_{10}H_6$	–510.092102693	–796.224965290	0.640594

It is important to understand what this value of 22.3 kcal/mol means in terms of the true resonance energy. To put this value in context, a similar calculation for benzene yields a resonance energy of 7.5 kcal/mol with an overlap of 0.8873.[3] From thermochemical analyses of the heats of hydration for benzene vs. cyclohexene, a value of 36 kcal/mol has been determined as the resonance stabilization for benzene.[4] Although the issue is more thoroughly discussed by Voter,[3] there are two reasons for the large discrepancy between the calculated and experimental values for the benzene resonance energy.

First, the orbitals optimized for the GVB(3/6) wave-function are not optimal for the full benzene resonance calculation. Allowing the orbitals to optimize for the resonance calculation increases the resonance energy to 13.5 kcal/mol (with an overlap of 0.6026),[3]

which is still significantly smaller than the experimental value. Second, the computational definition of the resonance energy is with respect to the GVB(3/6) wave-function. This definition assumes that there is no resonance in the GVB wave-function, which is not true. While the GVB wave-function exhibits the localization of VB wave-functions (*i.e.*, the dominant contributions to each bond come from the two component orbitals of the bond), GVB does allow contributions from orbitals not involved in the bond. In the case of benzene, the two π-orbitals comprising a bond each contain small contributions from neighboring π-orbital. Thus, the GVB wave-function does include some resonance.

Using the previous results for benzene, an estimate can be made of the "true" resonance energy. The benzene calculation, at the same correlation level using the same basis sets, accounts for about 21% of the experimental resonance energy, with an overlap between the two valence structures of 0.8873; with the orbitals optimized, the calculated resonance accounts for about 38% of the experimental resonance energy, with an overlap between the two valence structures of 0.6026. The overlap is a measure of the resonance included in the GVB wave-function: the greater the overlap, the greater the resonance included. In both cases, the percent experimental resonance energy scales roughly as $0.1494/S^2$ (which gives an error of ±4%) Using this relationship, a value of 61±7 kcal/mol is estimated as the true resonance stabilization. This value is a reasonable one, given that the per-π-bond resonance energy for benzene is 12 kcal/mol; the calculated per-π-bond resonance energy for $C_{10}H_6$ is 12.2 kcal/mol.

Cyclopentadienyl Anion

The cyclopentadienyl anion (Cp^-) geometry used in these calculations is taken from crystal structures of metal-Cp complexes, and is listed in Table 2.

Table 2. Geometric Parameters for Cp^-

Parameter	Value	Parameter	Value
R(C–H)	1.40 Å	θ(CCC)	108.0°
R(C–C)	1.08 Å	θ(HCC)	126.0°

For Cp the values in Table 3 are for the matrix elements between the specified charge localizations, either the 1-2 interactions (*ortho*) or the 1-3 interactions (*meta*). Solution of the secular equation for Cp leads to an E_{AB} of –192.185956986 hartree for the total wave function, compared to the single state energy of –192.17354519 hartree (both energies include nuclear repulsion terms). This leads to a calculated resonance energy of 7.789 kcal/mol. It is interesting how close in energy this value is to that previously calculated for benzene 7.5 kcal/mol at comparable levels of theory. This similarity suggests that the true resonance energy for Cp^- is about 36 kcal/mol. Using the overlap as a guide, the resonance energy of Cp^- is expected to be larger than benzene. However, the final Cp^- wave-function is described by 5 states, rather than 2 as for benzene, which means that the calculated value for Cp^- is a better estimate of the real resonance than the calculated value of benzene. Thus, the best estimate for the resonance energy of Cp^- is 36 kcal/mol.

Table 3. Resonance Matrix Elements and Overlaps for Cp.

Resonance Interaction	H_{AB} (hartrees)	H_{AA} (hartrees)	S_{AB}
Cp-*ortho* charges	–330.798477408	–342.951275455	0.965792
Cp-*meta* charges	–336.133480369	–342.951275455	0.981394

References

1. *Nanny* CPU-time balancer, Parallelograms, 7770 Regents Road, #251, San Diego, CA, 92122, info@pgrams.com.
2. Myers, A. G.; Finney, N. S. *J. Am. Chem. Soc.*, **1994**, *116*, 10986.
3. Voter, A. F., Ph. D. Thesis, California Institute of Technology, 1983.
4. Pauling, L. *The Nature of the Chemical Bond, Third Edition*, Cornell University Press: Ithaca, New York, 1960, p. 193.